DIRECTED TRANSPORT IN CHAOTIC HAMILTONIAN SYSTEMS

A THESIS

submitted for the award of Ph.D. degree of

MOHANLAL SUKHADIA UNIVERSITY

in the

Faculty of Science

by

Harinder Pal

Under the Supervision of

Dr. Madabushi Srinivasan Santhanam

Ex-Reader

Physical Research Laboratory, Ahmedabad, India

and

Co-Supervisor

Dr. Angom Dilip Kumar Singh

Associate Professor

Physical Research Laboratory, Ahmedabad, India

DEPARTMENT OF PHYSICS
MOHANLAL SUKHADIA UNIVERSITY
UDAIPUR
2011

To

My family

CERTIFICATE

I feel great pleasure in certifying that the thesis entitled, **"Directed Transport in Chaotic Hamiltonian Systems"** embodies a record of the results of investigations carried out by Harinder Pal under my guidance.

He has completed the following requirements as per Ph.D. regulations of the University.

(a) Course work as per the university rules.

(b) Residential requirements of the university.

(c) Presented his work in the departmental committee.

(d) Published/accepted minimum of two research papers in a referred research journal.

I am satisfied with the analysis of data, interpretation of results and conclusions drawn.

I recommend the submission of thesis.

Date :

Dr. Madabushi Srinivasan Santhanam
(Thesis Advisor)

Countersigned by
Head of the Department

DECLARATION

I, ***Harinder Pal****, S/O Mr. Harbans Lal, resident of A-2, PRL Residences, Navrangpura, Ahmedabad - 380 009, hereby declare that the work incorporated in the present thesis entitled,* ***"Directed Transport in Chaotic Hamiltonian Systems"*** *is my own and original. This work (in part or in full) has not been submitted to any University for the award of a Degree or a Diploma.*

Date :

(Harinder Pal)

Acknowledgments

First and foremost, I offer my sincerest gratitude to my supervisor, Dr. M. S. Santhanam, who has supported me throughout my thesis with his knowledge and patience. I am grateful to him for providing me unflinching encouragement and guidance during all these years. His openness to new ideas and intellectual support for their pursuance has made research life rewarding for me. I thank him for his efforts to educate me with the concepts and tools necessary for the work in this thesis.

I owe special gratitude to my co-supervisor, Dr. Dilip Angom. I extend my warmest thanks to him for many useful discussions, encouragement and support. I am grateful to him for his kind concern regarding my academic requirements.

I thank Dr. Bimalendu Deb for giving an encouraging start to my research life by guiding me in my coursework project. I would also like to thank Prof. J. Banerji, Dr. Jitesh Bhatt, Dr. Dilip Angom, Dr. M. S. Santhanam, Prof. Shyam Lal, Prof. R Sekar, Prof. S. A. Haider, Dr. Varun Sheel and Dr. A. K. Singal for teaching various courses and making coursework an enjoyable learning experience. I extend my thanks to Prof. P. K. Panigrahi for many informal but stimulating discussions during my early days in Physical Research Laboratory. I sincerely thank Prof. Sushanta Dattagupta and Prof. Steven Tomsovic for giving me their valuable time and sharing some ideas during their visit to PRL. Special thanks are due to Dr. R. Sankaranarayanan who visited PRL during starting phase of my doctoral research and discussed his work on generalized standard map. I would also like to thank Prof. Arul Lakshminarayan for some useful discussions during International conference on "Recent Developments in Non-linear Dynamic" held in Tiruchirapalli in 2008.

I am extremely grateful to PRL for various facilities it has provided, without which this thesis would not have been possible. I would also like to thank all the staff members of library, computer center, administration, maintenance and medical dispensary for their support in making efficient use of all the facilities possible. I would like to specially thank Mrs. Nishtha AnilKumar, Mrs. Pauline Joseph, Dr.

Sheetal Patel, Dr. Bhushit, Mrs. Parul Parikh, Miss Jayshree, Mr. Keyur Shah, Mr. Gangadharia, Mr. B. M. Joshi, Mr. Ghanshyam Patel, Mr. Ranganathan, Miss Pragya, and Mr. N. P. M. Nair for always being happy to help. I acknowledge the extensive use of High Performance Computing cluster facility for my thesis work. I am thankful to Mr. G. G. Dholakia, Mr. D. V. Subhedar, Mr. Jigar Raval, Mr. Hitendra, Mr. Tejas, Mr. Alok and Mr. Mrugesh Gajjar for their prompt actions to my computation related requests. I would like to extend my warmest regards for Mr. Manjunatha and Mr. Anish of CDAC, Pune for their help in using various packages on HPC. Their zeal to deal with HPC related issues made my life easy. I am also grateful to IISER, Pune for its hospitality during my visits for thesis related work. I also thank the staff of MLSU, Udaipur for their kind co-operation and prompt services.

I would like to thank all my friends in PRL for their affectionate company and best wishes, as well as express my apology that I could not mention names of all of them because they are just too many. Vimal and Suman have been good “school-mates”. Their company during the schools and conferences we have attended together made those learning periods more enjoyable. I would like to thank Suman also for helping me out whenever I had some software or operating system related issues. I also thank my senior Dr. Rajneesh Atre for his help and guidance.

I express my deepest thanks to my parents for their untiring efforts and encouragement throughout my studies. I also thank my sisters, Sunita and Sandeep, for their loving support. I express my sincere gratitude to my elder sister Sunita for her guidance during my schooling and also for encouraging me for higher education. I am deeply thankful to my wife Manan whose understanding, patience and unconditional support has kept my spirits up through thick and thin.

Finally, I feel great pleasure to express my gratitude to all others who have directly or indirectly contributed to this thesis.

ABSTRACT

We study the dynamics and directed transport in a class of chaotic Hamiltonian systems. The system we consider is a $\delta-$kicked particle in the presence of (i) double-barrier potential and (ii) periodic lattice of square-well potentials. In contrast to the well studied kicked rotor, the kicked system, in the presence of two variants of square-well potentials, studied in this thesis does not obey the Kolmogorov-Arnold-Moser (KAM) theorem. Due to this, invariant curves are absent and instead the phase space displays intricate chains of islands and fully connected chaotic layer even for very small kick strength. However, a special feature of the system reported in this thesis is that, inspite of being a non-KAM system, dynamics is KAM-like in some regions of phase space. We study the effect of interplay between of non-KAM and KAM-like phase space dynamics on dynamical properties of the system. We report a number of novel and interesting dynamical features like (a) the classically induced suppression of energy growth, (b) non-equilibrium steady state and (c) momentum filtering effect. We also report results for the quantum analogues of these dynamical features.

To study the directed transport properties of the system, we study evolution of a set of initial states. We study the effect of spatio-temporal symmetries on net current of a set of states. We observe that the system shows ratchet effect, *i.e.*, directed current in absence of net bias, upon breaking certain spatio-temporal symmetries. We explain how the non-KAM nature of the system imparts some useful characteristics to it as ratchet model. Throughout this work, we also analyse the quantum dynamics of the system, mainly in the semiclassical regime, and study the consequences of quantum effects. We also show that the system can act as a quantum ratchet.

Contents

List of Figures

CHAPTER 1

Introduction

Controlled transport of matter or energy is at the heart of many physics problems. Search for different ways of controlling and manipulating motion of particles like electrons, atoms, molecules, etc. encompasses many challenging problems of this class. Many of these problems are inspired by societal desire for new technologies and has always boosted the innate thirst for knowledge. The ever reducing size of electronic devices has come to mark the cutting edge in technology today. These devices rely on controlling directed but typically dissipative transport of electrons in different materials. Apart from electronic devices, directed transport occurs in natural systems as well. Transfer of water from roots of a tree to its leaves is the simplest example of such systems. However, this thesis is devoted to the physics of directed transport in a set of theoretical models relevant to some microscopic systems that can be tailor made.

In most devices, directed transport is driven by an energy source and a drain. This system of source and drain is deliberately designed to produce a net biased force for directed motion. However, humans have always longed for machines that would work perpetually without any interference. Unfortunately, a real perpetual

machine[1] is forbidden by the second law of thermodynamics, as will be clear in later sections, and indeed no such machine exists that can extract work out of a system in equilibrium situation. Nevertheless, this aspiration provoked the study of the systems which are capable of extracting work from random motion of particles in absence of any net bias though in a non-equilibrium situation. Typically, it is possible to actually implement this in systems of microscopic dimensions. They are termed ratchets and the phenomenon of extracting work in this manner is called ratchet effect.

This thesis is pivoted around the study of ratchet phenomenon in some theoretical models relevant in the study of chaotic quantum systems. The models themselves are experimentally realizable in the laboratory using a test bed of cold atoms and optical lattices. Along with the ratchet effect, we study some associated transport properties like particle pumping, momentum filtering, classical suppression of energy and dynamical localization. It is appropriate to begin with an introduction to ratchets and their brief history.

1.1 The Ratchets and Their History

In a general sense, ratchets are devices used to restrict motion to one particular direction. For instance, a turnstile can be turned only in one direction on application of force. This is one of the commonly occurring example of ratchet device encountered in daily life. However, the notion of ratchets and ratchet effect that scientists deal with is not uniquely defined. Nevertheless, there are few points common among various types of ratchets in science. For example, they are systems that work outside of equilibrium in a random environment and provide directed transport in periodic media in absence of any net bias. Symmetry breaking, spatial and/or tem-

[1]Perpetual machines of physicist's interest are of two kinds. Perpetual machines of first kind would function without any energy input and are trivially ruled out by first law of thermodynamics. Perpetual machines of second kind would extract work from a system in an equilibrium state violating the second law of thermodynamics. Perpetual machines of second kind gained much interest. None of these machines are realizable in practice.

poral, is also a central concept in the study of ratchet phenomena. The best way to reveal the flavor of the field will be through a discussion of the work already done in the field. An expedition through major contributions in the field, therefore, follows.

As already mentioned, the study of ratchets was provoked by the quest for perpetual machines which can put to work the energy absorbed from their surrounding without any deliberate human interference. A self winding wrist watch, also called as perpetual watch, is a macroscopic example of something close to a real perpetual machine. It is designed to use the random motion of wearer's wrist as a source of energy which is stored and used to turn its hands unidirectionally even when it is not worn. This self winding mechanism, however, has to be invoked periodically which, of course, needs wearer's intervention. Such novel designs were hardly thought to be possible in microscopic systems until the fabrication techniques evolved to manufacture devices that are of sub-micron dimensions. Moreover, microscopic can not escape from the effect of ambient thermal noise. Then the natural question arises - is it possible to extract useful work from a system without a net biased force in the presence of thermal noise? First comprehensive theoretical work addressing this question was done by Smoluchowski through his thought experiment in 1912, later on popularized and extended by Feynman in 1952 [Fe63]. Smoluchowski gave the first qualitative explanation of why a device would fails to extract work from random motion of particles in an equilibrium situation. Feynman in his extension to Smoluchowski's thought experiment showed that it is possible to extract work from random motion of particles but only after breaking the thermal equilibrium. Before we voyage further into history of ratchets, it worth mentioning about Peter Reimann's review [Re02] that gives a more detailed account of history and fundamental concepts of ratchets. This discussion will move along a path that will lead to the subject of the thesis.

1.2 Deterministic Ratchets

As mentioned in Ref. [Re02], another motivation for the early work on ratchets is rooted in intracellular transport research in biological systems, said to be stemming from A. Huxley's ground-breaking *sliding filament model* of muscle contraction in 1957. Since late 1980s, there have been renewed interest in transport phenomena in biological systems, probably due to advancement in microscopy and micro scale control. The study of biophysical machines relying on ratchet phenomena for their functioning, popularly known as molecular motors, offered physicists more realistic situations to analyze deeper physics of ratchet effect. Therefore, most of the early physics of ratchets dealt with the models inspired from biological system [Ma93, Ma94, As94]. In all these bio-inspired ratchets, the source of non-equilibrium fluctuations have been the thermal noise that manifests itself as Brownian motion of molecules. Therefore these ratchet systems are known as thermal ratchets, Brownian ratchets or Brownian motors. This ground breaking work that explained basic principles of ratchet phenomena inspired the study of diverse models for Brownian ratchets exploring the effect of properties of noise and potential, interaction, damping, quantum effects etc. [Do94, Ba94, Ce96, Re97, Ku98, Ka98, Bl98, Sc97].

Simultaneously, the need for a better understanding of the phenomena encouraged the study of minimalist ratchet models including new mechanisms not based on thermal noise. This initiated the study of deterministic ratchets in which chaos played the role of noise in providing random environment [Ju96, Sa99, Ma00, Tr00, Ba00]. In this direction, ratchet effect in a deterministic system free from both noise and dissipation was considered [Sc01, Gr02]. These noise and dissipation free ratchets are based on Hamiltonian systems. The desire to realize artificial nanostructured ratchets have been the motivation for for incorporation of quantum effects in these Hamiltonian ratchets [Ko03]. Kicked rotor system has served as paradigmatic model for the study of Hamiltonian chaos both in classical and quantum version [Iz90, Za07]. It can be thought of as a pendulum that receives periodic kicks

by a sinusoidal potential. With the advent of laser cooling and optical lattices, the kicked rotor model has been experimentally realized in the laboratory [Mo95]. As a result, much of the work on the chaotic Hamiltonian ratchets is based on kicked rotor system. First, we describe the kicked rotor model in some detail.

1.3 Kicked Particle System

The Hamiltonian of the kicked rotor system is given by,

$$H = \frac{p^2}{2} + \epsilon \cos(x) \sum_{n=-\infty}^{\infty} \delta(t-n), \qquad n \in \text{integer}. \tag{1.1}$$

This represents a system in which a particle is subjected to a spatially periodic potential field $\cos(x)$, modulated by a periodic sequence of delta functions in time. The term kick stands for effect of potential that acts for infinitesimally small duration due to modulation by the delta function. The potential field is generally referred to as kicking field and its amplitude ϵ as kick strength. Between any two kicks, particle act like a free particle. Notice that the mass and kicking period, ie. time duration between two δ-kicks is set to be 1, and periodicity or wave length of the kicking field is set to be 2π for simplicity. In fact, for any arbitrary values of these parameters, Hamiltonian can be reduced to the above form through appropriate coordinate transformation.

The Hamilton's equations of motion corresponding to the system in Eq. (1.1) are

$$\dot{x} = p, \tag{1.2a}$$

$$\dot{p} = \epsilon \sin(x) \sum_{n=-\infty}^{\infty} \delta(t-n). \tag{1.2b}$$

Clearly, for $\epsilon = 0$, corresponding to the free evolution of the particle, Eq. (1.2a) can also be trivially integrated and we obtain the solutions of Eq. (1.2) as

$$x = x_0 + pt, \qquad ; \qquad p = p_0. \tag{1.3}$$

Here, x_0 and p_0 represent the initial position and momentum of the particle. By applying the periodic boundary condition and restricting the position variable to $x \in [-\pi, \pi]$, we can transform to action-angle coordinates (J, θ). The kicked particle system with periodic boundaries is equivalent to the kicked rotor. In phase space (θ, J), this trajectory will be represented by straight line extending from $-\pi$ to π intersecting J-axis at $J_0 (= p_0$, in this case).

For $\epsilon \neq 0$, this system is non-integrable. However, the evolution can be treated period-wise. Let (x_n, p_n) be the position and momentum of particle just before the n^{th} kick. One notices that motion over one kicking period can be divided into two parts:

(i) Kicking part - This takes place for infinitesimal duration over which no change in position occurs, but momentum will change according to Eq. (1.2b) due to energy absorbed from the kick. The evolved momentum p_{n+1} after the kick can be obtained by integrating Eq. (1.2b) over duration δt of delta kick, in the limit of $\delta t \to 0$, as

$$p_{n+1} = \int_{n-\frac{\delta t}{2}}^{n+\frac{\delta t}{2}} \epsilon \sin(x) \sum_{n=-\infty}^{\infty} \delta(t-n)dt = p_n + \sin(x_n). \tag{1.4}$$

(ii) Free evolution part - This takes place in between the kicks during which particle moves with constant the momentum p_{n+1}, according to Eq. (1.2a). Adding distance traveled by particle during this period to x_n, one gets,

$$x_{n+1} = x_n + p_{n+1}. \tag{1.5}$$

Thus, we obtain the Chirikov map [chirikov], popularly known as standard map, defined on an infinite plane $-\infty \leq x_n, p_n \leq \infty$,

$$p_{n+1} = p_n + \epsilon \sin(x_n), \tag{1.6a}$$

$$x_{n+1} = x_n + p_{n+1}. \tag{1.6b}$$

Notice that the map can be made periodic both in x and p. By applying periodic

boundary conditions over one period (2π) from $-\pi$ to π in both x and p space, we get,

$$J_{n+1} = J_n + \epsilon \sin(\theta_n), \tag{1.7a}$$

$$\theta_{n+1} = \theta_n + J_{n+1}. \tag{1.7b}$$

Figure 1.1 shows phase space of standard map for different values of ϵ. Note that each of the trajectories (θ_n, J_n) actually represents only a stroboscopic section, at times just before the kicks, of continuous trajectory $(\theta(t), J(t), t)$. However, since the motion between the kicks is trivial free motion, all the phase space features can be studied on this section. For $\epsilon << 1$, we see there exist many continuous curves. Each curves represents a torus which is deformed due to perturbation ($\epsilon \neq 0$). These curves are called invariant curves because of associated conserved quantity w known as winding number number. This is defined as $w = \frac{(\theta_n - \theta_0)}{nd}, \quad n \rightarrow \infty$ and determines the long time average velocity. Here, d represents length of spatial period which set to be 2π. The rational values of w would correspond to periodic orbits. A periodic orbit would appear as set of finite number of points in the stroboscopic section. Irrational values of w are associated with quasiperiodic orbits. These are the orbits in which trajectory never repeats itself, however, after long enough time it comes infinitely close to its starting point. Both the periodic and the quasiperiodic orbits represent regular motion. Thus we see that for $\epsilon << 1$, the phase space is mostly populated with regular orbits.

Invariant curves generally tend to be barriers to global connectivity in phase space. This is a consequence of the fact that two trajectories in phase space can not intersect each other. As ϵ increases, the invariant curves get more and more deformed and ultimately begin to break down. This leads to a connected and mixed phase space comprising chaotic as well as regular region, the so-called islands. For $\epsilon >> 1$, all these invariant curves break down and the phase space is largely chaotic in which some islands, which represent regular orbits, are embedded. In this situ-

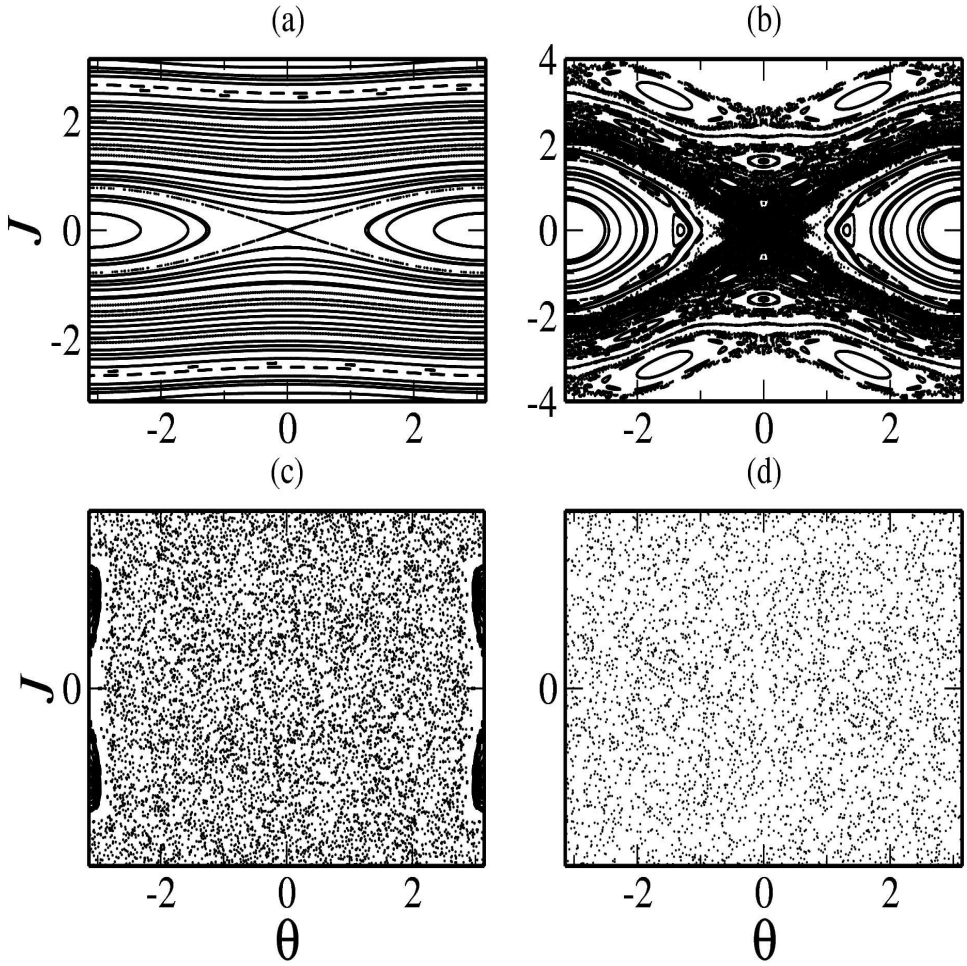

Figure 1.1: Phase space of standard map for different values of kick strength, ϵ. The kick strengths are (a) 0.15, (b) 1.0, (c) 4.5, and (d) 10. Gradual transition from regular to chaotic dynamics occur with increasing ϵ.

ation, the unbounded spread in momentum and energy space becomes possible (to observe them one has to remove periodic boundaries applied along p). However, the rate of energy growth can be hampered by the presence of sticky regions around stable islands where a chaotic trajectory might spend more time compared to other regions of phase space [Za07]. For large kick strengths, the system displays approximately normal diffusion with diffusion constant $D = \frac{\epsilon^2}{2}$ being a function only of the kick strength. Deviations from normal diffusion have been studied by Rechester and White [Re80].

Notice that the transition of the standard map from regular to chaotic dynamics is gradual with the increasing perturbation strength ϵ. Such gradual transition in systems like the standard map is guaranteed by the celebrated Kolmogorov-Arnold-Moser (KAM) theorem [Ta89, Ot93]. According to KAM theorem, under certain conditions, if a small perturbation is applied to an integrable system, then corresponding to each invariant curve of the integrable system, there exist another invariant curve (also called KAM torus) which is close to original one. In other words, in presence of small perturbation, the invariant curves are only slightly deformed. One of the conditions of the KAM theorem is that the unperturbed system should be analytic. Much of this thesis is concerned with of non-analytic potential and hence KAM theorem does not apply. In such a scenario, as we shall see in the next chapters, all the invariant curves are destroyed even for very small perturbation.

In case of quantum kicked particle [Iz90], the evolution can be studied through one time-period evolution operator, known as Floquet operator, that evolves an initial state over one kicking period. This is expressed as,

$$\widehat{U} = \exp\left(-\frac{i\epsilon}{\hbar_s}\cos\widehat{x}\right)\exp\left(-\frac{i}{\hbar_s}\frac{\widehat{p}^2}{2}\right). \tag{1.8}$$

Here, the first term represent the effect of kicking and the second the effect of free evolution between the kicks. The eigen states of the Floquet operator $\widehat{U}$, known as Floquet state, will represent the asymptotic dynamics of the system. These states are the equivalent of the stationary states for the time independent quantum system.

One major feature observed in quantum version of the system is the dynamical localization [Re04, St93]. For $\epsilon >> 1$, as discussed earlier, the classical dynamics is nearly diffusive. However, in the corresponding quantum system, the diffusive growth of energy is arrested by dynamical localization [Ca79, Ca84] arising due to destructive quantum interferences. We will see that dynamical localization plays an important role in Hamiltonian ratchets based on kicked particle system.

1.4 Quantum Ratchets

The work of Schanz et. al. [Sc01, Hu04] appears to be the first proposal to study chaotic Hamiltonian ratchets. In this work, it was argued that in a regime of mixed phase space with islands of regularity embedded in a chaotic layer, directed transport is possible if appropriate spatio-temporal symmetries are broken. The directed transport in this proposal arises from the imbalance between the transport due to the island structures and the chaotic layer in phase space. This imbalance is induced by breaking the spatio-temporal symmetries in the system. The quantum ratchet appears in the corresponding semiclassical regime in which the classical mechanism largely carries over to the quantum regime.

Is it possible to obtain directed transport in chaotic regime of the system ? Monteiro et. al. [Mo02] show, using kicked rotor model, that it is indeed possible. Classical kicked rotor, for large kick strengths, is predominantly chaotic. It leads to unbounded growth in energy as a function of time, $E_n \approx Dn$, where D is the diffusion coefficient. Upon breaking spatio-temporal symmetries appropriately, the particles with positive and negative momenta have diffusion coefficients D_+ and D_- respectively. Thus, the rate of energy growth continues to be linear but is different for particles travelling in different directions. Thus, it leads to net mean momenta $\langle p \rangle \neq 0$, *i.e.,* directed motion becomes possible. However, there is a catch. The unbounded growth in energy dilutes the mean momenta continually and hence it will not work as a meaningful ratchet. However, thanks to dynamical

localization in the corresponding quantum system, the energy growth is arrested and we obtain a quantum ratchet in which the net mean momenta $\langle p \rangle$ has converged to a non-zero value. Thus, the system works as a quantum ratchet. This effect was claimed to be a true quantum ratchet mechanism. Typically, in systems based on kicked rotor, spatial symmetry is broken by manipulating the phase and temporal symmetry is broken by additional kicks in every cycle. However, in one possible experimental realization of the quantum ratchet [Jo07a], spatial symmetry is broken by a rocking potential and temporal symmetry by placing additional kicks. This represents one of the first experimental results on quantum ratchets. Another experimental effort based on kicked rotor was performed by Dana *et. al.*, [Da08] in which Bose-Einstein condensate in standing waves were used to realize quantum-resonance ratchets leading ratchet acceleration. Directed transport in a driven (as opposed to a kicked) classical system was experimentally realized using atomic rubidium Bose-Einstein condensates in time modulated optical lattices [Sa09]. In this case, the ratchet effect arises due to desymmetrization of the Floquet states in the quantum regime. With these developments, there were reports on control of ratchet effect in cold atoms [Ke08], ratchets in driven quantum systems [De07], ratchet accelerators [Wa08, Da11], quantum ratchets at resonance [Po07, Cu09] and proposals for ratchets in other models of quantum chaos [Wa08a, Er09]. The bulk of ratchet work in the context of chaos and quantum chaos is based on some variant of the kicked rotor, which as we pointed out earlier, is an example for how KAM theory works out in practice. However, there is the other class of system that does not obey the KAM theory. The central idea in the thesis is to study the directed transport in non-KAM systems and exploit their dynamical features for directed motion.

1.5 Motivation

The kicked rotor is a popular model of chaos and for the same reason turns out to be popular in the context of chaotic ratchet as well. Much less is known about the

systems that do not obey KAM theorem. In the last two decades, at least a couple of non-KAM systems have been studied in some detail; the kicked harmonic oscillator [Ch87, Ch88] and kicked particle in infinite well [Sa01]. In the first case, the classical system is degenerate which leads to non-KAM behavior. The the second case, the classical system is non-analytic, the reason for being non-KAM. We now know from earlier studies that in either of these cases, the system displays abrupt transition to chaos (as opposed to smooth transition in a KAM system such as kicked rotor) and the phase space can be mixed but without any invariant tori. Kicked harmonic oscillator was shown to be experimentally realizable using an ion trap [Ga97]. However, infinite wells are only an idealization and cannot be exactly replicated in experiments. A suitable modification would be to consider finite potential wells. This might look like a simple modification possibly retaining the non-KAM nature of the system but it leads to significant changes in the dynamics. Firstly, this allows for transport in the spatial and momentum coordinates. In the infinite well, there can be no true transport along coordinate axis. For instance, in a recent experiment, Henderson et al [He06] constructed a quasi-one-dimensional finite box using a combination of optical and magnetic trap, with the Bose-Einstein condensates BECs in the box receiving periodic kicks. This setup was used to study the effect of atomic interactions on the transport of BECs. In place of the dynamical localization they observed a classical saturation in the energy of BECs due to a balance between the energy gained from kicks and the energy lost by leakage of BECs over the finite barrier. Then, one of the questions would be the role of non-KAM dynamics in such results. Going beyond finite well, we can construct potentials with double barrier or a lattice of finite wells. Such stationary potentials have relevance in applications. Much of electronic devices are based on quantum wells such as double barrier structures constructed from semiconducting materials. Hence the transport and ratchet effect in a prototype such as the finite well can lead to better understanding of the non-KAM dynamics with and without the ratchet currents. Due to its potential applications in electronic devices, this could ultimately

lead to better control over ratchet type currents in such systems. For instance, the effect of non-KAM chaos on transport properties of semiconductor superlattices has already been addressed by Fromhold et. al. [Fr01, Ba08] though not in the context of ratchets. However, it must be pointed out that electronic devices do not rely on ratchet effect for the conduction of electrons but on the external bias provided by the power source. All this points to a potential experimental realization of kicked system placed in finite well potential. Motivated by these considerations, we choose to study dynamics and directed transport properties of a non-KAM Hamiltonian system described briefly below.

We study dynamics and directed transport properties of systems that can be defined by a general Hamiltonian of the form

$$H = \frac{p^2}{2m} + V_s(x) + \epsilon f\left(x\right) g\left(t\right). \tag{1.9}$$

In this, V_s is the stationary potential that could represent a square well or a 1D lattice of wells. Both these stationary potential are non-analytic. Due to presence of these non-analytic potentials, the system is non-KAM, *i.e.* it does not KAM theorem. The system is driven by a periodic series of kicks obtained using smooth potential field varying spatially as $f\left(x\right)$ and temporally modulated by series of delta functions given by $g(t)$. ϵ is the strength of kicking field. In order to study the system in different situations, we use different specific forms for V_s, $f\left(x\right)$ and $g\left(t\right)$. In the next chapters, the work in this thesis covers the following problems. We basically study the effect of non-KAM potential on the dynamics of the system. We study the effect of spatial and time symmetry on the dynamical features of these systems along with the consequences of breaking these symmetries. We also study the effect of these symmetries on net directed transport of the system. We also study the quantum version of the system through wave packet evolution and Floquet analyses. We address the effect of quantum dynamics on various dynamical properties of the system.

CHAPTER 2

Kicked Particle in a Double-barrier Structure: The Phase Space Dynamics

The dynamics of a particle in a one dimensional lattice of finite wells (Fig. 2.1) is a fundamental model of significant interest in condensed matter physics [Bu92,As76]. For instance, Konig-Penney model [Li80] forms the basis for our understanding of crystalline structure in solids. A kicked particle in such a potential is the candidate for the study of ratchet effect in this thesis. Before we consider a lattice of finite wells, firstly we begin with a study of a kicked particle in double-barrier structure (DBS). This would be a segment extending from the mid-point of the left barrier to mid-point of the right barrier. This system turns out be an ideal building block for analyzing the dynamical aspects of kicked particle in a lattice of finite wells. The transport of electron through a double-barrier structure is perhaps one of the most important idea that finds application in resonant tunnelling diodes and in many other electronic devices [Le03] though without the applied kicks.

From the point of view of classically chaotic Hamiltonian systems, kicked particle in a DBS is one possible generalization of the widely studied kicked rotor system [Ch79, Re04]. Then, it is not entirely surprising that the dynamics of a particle

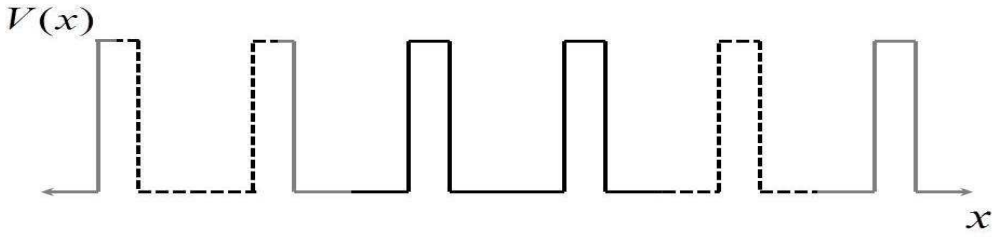

Figure 2.1: Grey line shows the periodic lattice of identical equally spaced finite wells. Dotted lines superimposed on it show two kinds of periodic units. Solid black line shows the double barrier structure.

in DBS, in the region between the two barriers, can be analyses in terms of kicked rotor dynamics. In this chapter, we derive a classical map for studying the evolution of a kicked particle in the presence of a double-barrier structure. This map can be thought of as a standard map [Re04] in which the effect of finite barriers has been incorporated. The role of kick strength, symmetries and length scales involved in determining phase space features are discussed. The semiclassical regime in which quantum dynamics mimics the classical one is also highlighted in this chapter.

2.1 The System

We consider the system described by the Hamiltonian

$$H = \frac{p^2}{2m} + V_{sq}(x) + \epsilon \cos\left(\frac{2\pi x}{\lambda} + \phi\right) \sum_{n=-\infty}^{\infty} \delta(t - nT), \tag{2.1}$$

where the stationary potential is given by,

$$V_{sq}(x) = V_0 \left[\Theta(x + b + a) - \Theta(x + a) + \Theta(x - a) - \Theta(x - a - b)\right]. \tag{2.2}$$

In this, $\Theta(.)$ represents a unit step function. The double-barrier structure $V_{sq}(x)$ is shown as part of a series of wells in Fig. 2.1, and again separately in Fig. 2.2. This

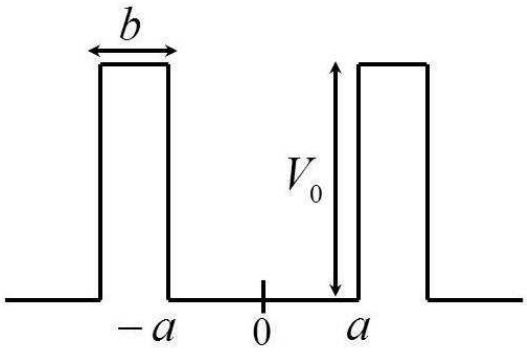

Figure 2.2: Schematic of the stationary part of the potential: The double-barrier structure

potential can be written in piece-wise form as,

$$V_{sq}(x) = 0, \quad -\infty \leq x \leq -a-b, \tag{2.3a}$$

$$= V_0, \quad -a-b \leq x \leq -a, \tag{2.3b}$$

$$= 0, \quad -a \leq x \leq a, \tag{2.3c}$$

$$= V_0, \quad a \leq x \leq b, \tag{2.3d}$$

$$= 0, \quad b \leq x \leq \infty. \tag{2.3e}$$

The two barriers are taken to be identical in this work and each of them has width b and height V_0. The barriers, separated by a distance $2a$, are positioned symmetrically the origin, at $\pm a$, for convenience. Along with this stationary potential, the particle is subjected to extremely short impulses acting at equal intervals of time. These impulses are collectively represented as a series of delta functions shown in the last term and, therefore, called as delta kicks. The strength of the impulsive force applied by these kicks varies as a sinusoidal function of wavelength λ and amplitude ϵ. Application of these kicks is equivalent to a periodic flashing of the cosinusoidal potential field of given wavelength and amplitude modulated temporally through a series of delta functions. The amplitude ϵ is generally referred to as kick strength. The symbol ϕ represents the phase of the kicking field with respect to the origin.

The set of canonical transformations given by

$$t = \widetilde{t}T, \quad x = \lambda\frac{(\widetilde{x}-\widetilde{\phi})}{2\pi}, \quad p = \frac{\widetilde{p}TE_c}{\lambda\pi},$$
$$H = \frac{\widetilde{H}E_c}{2\pi^2}, \quad \epsilon = \frac{\widetilde{\epsilon}E_cT}{2\pi^2}, \quad V_0 = \frac{\widetilde{V}_0E_c}{2\pi^2}, \quad b = \frac{\lambda}{2\pi}\widetilde{b}, \tag{2.4}$$

with $E_c = m\lambda^2/2T^2$ leads to a new dimensionless Hamiltonian

$$\widetilde{H} = \frac{\widetilde{p}^2}{2} + \widetilde{V}_{sq}(\widetilde{x}) + \widetilde{\epsilon}\cos(\widetilde{x})\sum_{n=-\infty}^{\infty}\delta(\widetilde{t}-n). \tag{2.5}$$

All the discussions in this chapter will henceforth refer to the scaled parameters and variables though for convenience we suppress the tilde symbols and the Hamiltonian can be written as,

$$H = \frac{p^2}{2} + V_{sq}(x) + \epsilon\cos(x)\sum_{n=-\infty}^{\infty}\delta(t-n). \tag{2.6}$$

Here,
$V_{sq}(x) = V_0\left[\Theta(x-\phi+b+R\pi) - \Theta(x-\phi+R\pi) + \Theta(x-\phi-R\pi) - \Theta(x-\phi-R\pi-b)\right]$ with $R = 2a/\lambda$ being the ratio of the width of the well to the wave length of the kicking field. Following the canonical transformation, note that R is a ratio of two length scales in the system and is a dimensionless quantity. Further, the kicking period and the mass in the transformed coordinates becomes unity. Consequently, the set of parameters determining the classical dynamics of the system are, namely, ϵ, R, b, V_0 and ϕ. Of these, R, b and ϕ determine the positions of discontinuities in the potential (position of the wall boundaries) at $\mathbf{B} = \{-x_l - b, -x_l, x_r, x_r + b\}$ where $x_l = -R\pi + \phi$ and $x_r = R\pi + \phi$. Note that if ϕ= 0, then $x_l = x_r$. In that situation, we take $x_r = x_w$ and $x_l = -x_w$. Thus, the qualitative nature of the classical dynamics depends on the kick strength ϵ and the potential height V_0 and positions of the wall boundaries collectively denoted by **B**.

2.2 The Classical Map

The Hamiltonian in Eq. (2.6) is integrable for $\epsilon = 0$. The situation corresponds to a particle moving freely in presence of barriers with momentum that has a constant magnitude and its sign changing on every reflection from the barriers. For $\epsilon = 0$, it is possible to transform to a new set of action-angle variables. In the well region, which supports periodic motion, for a particle with energy $E \leq V_0$, the action-angle transformation results in $H = \frac{\pi^2 J^2}{8a^2}$, where J is the action variable. In the case when $\epsilon > 0$ and $V_{sq}(x) = V_0$ (a constant), the dynamics is non-trivial leading to the well studied standard map [Re04] as shown in chapter 1. However, for $\epsilon > 0$ in the presence of DBS potential shown in Eq. (2.2), *i.e.*, in the presence of both the kicking field and the non-analytic potential, the system becomes non-integrable. In this case, the dynamics is even more rich and complex than a kicked rotor system. To best of our knowledge, such a system has not been studied until now in the context of Hamiltonian chaotic systems.

To simplify the task of dealing with non-analytic potential, we separate out the effects of the kicking and the stationary potential by rewriting the Hamiltonian in Eq. (2.6) as,

$$H = H_0 + V_{sq}(x). \tag{2.7}$$

where, $H_0 = \frac{p^2}{2} + \epsilon \cos(x) \sum_{n=-\infty}^{\infty} \delta(t-n)$ is the time-dependent part and $V_{sq}(x)$ separately accounts for the effect of stationary part. Now, we evolve the system as being entirely governed by H_0 that leads to the difference equations in Eq. (2.8a) and then incorporate the effect of discontinuities in $V_{sq}(x)$ through appropriate boundary conditions and this leads to Eq. (2.8b). This leads to the following map:

$$\begin{aligned} p_n &= p_{n-1} + \epsilon \sin(x_{n-1}), \\ x_n &= x_{n-1} + p_n, \end{aligned} \tag{2.8a}$$

$$\begin{pmatrix} p_n \\ x_n \end{pmatrix} \rightarrow \widehat{\mathcal{R}} \begin{pmatrix} p_n \\ x_n \end{pmatrix}. \tag{2.8b}$$

Equation (2.8a), that represents the effect of H_0, is identical to the standard map except that the periodic boundary conditions have not been applied here because the potential $V_{sq}(x)$ is explicitly non-periodic. We can write $\widehat{\mathcal{R}} = \widehat{\mathcal{R}}_k \ldots \widehat{\mathcal{R}}_2 \widehat{\mathcal{R}}_1$, *i.e.*, as time ordered product of operators $\widehat{\mathcal{R}}_1, \widehat{\mathcal{R}}_2, \ldots, \widehat{\mathcal{R}}_k$ that separately represent effects due to encounters of the particle, in between two kicks, with the discontinuities of V_{sq} at positions represented by $B_1, B_2, \ldots B_k$, respectively. Here, k represent total number of boundaries encountered by particle in between any two consecutive kicks. Depending on the energy, each of these k encounters could either be a reflection (sign of momentum changes) or refraction (magnitude of momentum changes) at $B_i \in \mathbf{B}$, $i = 1, 2, ...k$.

To keep track of the potential discontinuities encountered by the particle between successive kicks, the following procedure is implemented. Between two kicks acting at integer times, say n and $n+1$, we denote the state of the particle after incorporating effect of ith encounter with the discontinuity that happens at B_i by $\binom{x_n^i}{p_n^i}$. We define $]x_s^i, x_n^i[$ with $i = 0, 1 \ldots k$ as the path, starting from x_s^i, a particle would traverse between the two kicks after encountering i^{th} discontinuity if there were no discontinuities to be faced till the next kick. For $i = 0$, x_s^i would simply be x_{n-1} and B_i for $i > 0$. x_n^0 and p_n^0 would be x_n and p_n obtained directly from Eq. (2.8a). Now, B_{i+1} would be the position of the discontinuity that lies with in the interval $]x_s^i, x_n^i[$ and is closest to x_s^i. For the discontinuity in the potential $V_{sq}(x)$ at B_{i+1}, we have,

$$\binom{x_n^{i+1}}{p_n^{i+1}} = R_{i+1} \binom{x_n^i}{p_n^i} \tag{2.9}$$

Now, B_{i+2} can be determined from $x_s^{i+1} = B_{i+1}$, x_n^{i+1} and the corresponding R_{i+2} is applied to $\binom{x_n^{i+1}}{p_n^{i+1}}$. In this manner, boundary conditions are applied k times until $\big]x_s^k, x_n^k\big[\cap \mathbf{B} = \emptyset$.

The map in Eq. 2.8 would be complete if the transformation that the operator $\widehat{\mathcal{R}}_i$ effects on the state $\binom{x_n^{i-1}}{p_n^{i-1}}$ to incorporate the effect of i^{th} discontinuity is explicitly written down. Let E_n denote the energy of the particle just after the nth kick (at time n). If $E_n < V_0$, particle will suffer reflection at the discontinuity at B_i. This implies that the momentum of particle after incorporation of effect of this encounter should be $p_n^i = -p_n^{i-1}$. In the case for $E_n > V_0$, particle will suffer a change in the magnitude of its momentum (due to change in its kinetic and potential energy with its total energy conserved) while it crosses the potential discontinuity. We call this process refraction. The momentum after a refraction can be obtained using conservation of energy and we get,

$$p_n^i = \text{sign}(p_n^{i-1})\sqrt{(p_n^{i-1})^2 - (\text{sign}(V_{diff}))\,2V_0}, \qquad E_n > V_0, \tag{2.10}$$

where, sign$(.)$ denotes the sign and $V_{diff} = V(B_i) - V(x_s^{i-1})$. The position x_n^i of the particle after it encounters discontinuity at B_i can be obtained by evolving it with the new momentum p_n^i starting from B_i for remaining time of evolution (until the next kick). This time will be equal to $(x_n^{i-1} - B_i)/p_n^{i-1}$. This gives,

$$x_n^i = 2B_i - x_n^{i-1} \quad \text{for reflection}, \tag{2.11}$$

$$x_n^i = B_i + \frac{(x_n^{i-1} - B_i)\,p_n^i}{p_n^{i-1}} \quad \text{for refraction}. \tag{2.12}$$

Using these transformation that relate $\binom{x_n^{i-1}}{p_n^{i-1}}$ to $\binom{x_n^i}{p_n^i}$, we can define $\widehat{\mathcal{R}}_i$ through Eq (2.13). For $E_n \leq V_0$ (reflective boundary condition), we have

$$\begin{pmatrix} x_n^i \\ p_n^i \end{pmatrix} = \widehat{\mathcal{R}}_i \begin{pmatrix} x_n^{i-1} \\ p_n^{i-1} \end{pmatrix} = \begin{pmatrix} 2B_i - x_n^{i-1} \\ -p_n^{i-1} \end{pmatrix}. \tag{2.13a}$$

For $E_n > V_0$ (refractive boundary condition), we have

$$\begin{pmatrix} x_n^i \\ p_n^i \end{pmatrix} = \widehat{\mathcal{R}}_i \begin{pmatrix} x_n^{i-1} \\ p_n^{i-1} \end{pmatrix} = \begin{pmatrix} B_i + \dfrac{(x_n^{i-1} - B_i)\, p_n^i}{p_n^{i-1}} \\ \text{sign}(p_n^{i-1}) \sqrt{(p_n^{i-1})^2 - (\text{sign}(V_{diff}))2V_0} \end{pmatrix}. \tag{2.13b}$$

Thus, the dynamics of system in Eq. (2.6) can be described by the standard map defined on an infinite plane, i.e., $-\infty \leq x_n, p_n \leq \infty$ (Eq. (2.8a)) and subjected to potential barriers (Eq. (2.8b)). Notice that by putting $V_0 = 0$ in Eq. (2.13b), we obtain $\widehat{\mathcal{R}}_i = \mathbf{I}$ for all i, where $\mathbf{I}$ is the identity matrix of order 2. Then $\widehat{\mathcal{R}} = \mathbf{I}$ and, as expected, Eq. (2.8) reduces to standard map for $V_0 = 0$. Thus, the transformation in Eq. (2.13) can be viewed as deviation from standard map dynamics induced after each encounter of the particle with a discontinuity of the potential $V_{sq}(x)$. Note that the map we have obtained can be thought of as a generalization of the generalized standard map [Sa01].

Note that the map derived above relates the positions and momenta just before two consecutive kicks. In other words, it gives only stroboscopic view of the three dimensional phase space (x, p, t), and the stroboscopic section is taken at the "phase" of kicking period that corresponds to times just before the kicks. Unlike in case of standard map, in which the motion between the kicks is free motion with constant momentum, momentum may change between the kicks due to reflection or refraction at a potential discontinuity in system in Eq. 2.1. However, this change in momentum between the kicks does not affect the major phase space features, like regions of chaos, regularity etc, which are main objects of interest in this chapter. Thus, it will be sufficient to analyze a stroboscopic section of phase space in this chapter.

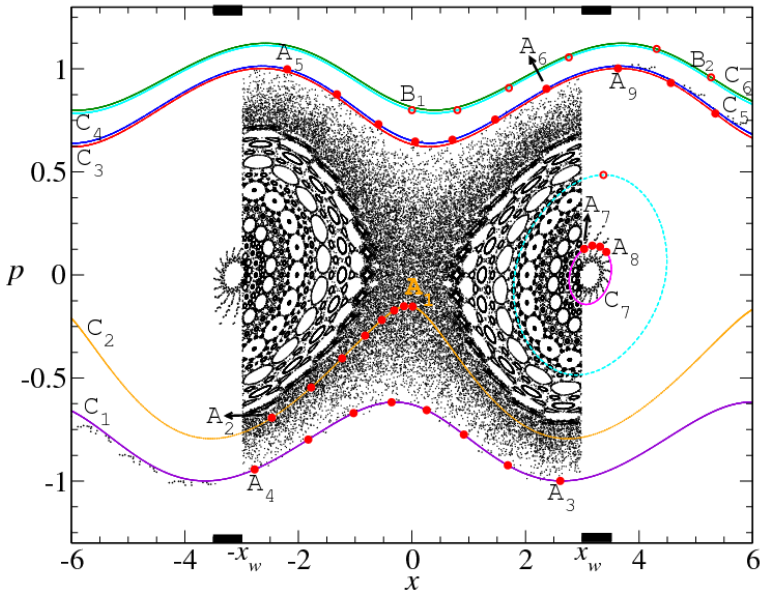

Figure 2.3: Stroboscopic Poincare section (black) for $R = 0.95, \epsilon = 0.15, V_0 = 0.5, \phi = 0$ and $b = 0.5$. All the continuous curves (in color) marked C_1 to C_6 are for the corresponding standard map with kick strength 0.15. The black box at position $x = \pm x_w$ indicates the width b of the barrier. The solid circles (in red) show a trajectory starting from A_1 until it exits the potential well at A_9. The time ordered sequence of the trajectory is A_1 to A_2, reflection at $-x_w$, A_3 to A_4, reflection at x_w, A_5 to A_6, cross the boundary at x_w, A_7 to A_8, cross the boundary at $x_w + b$, exit the potential at A_9. See text for details. Open red circles show trajectory of a particle with initial state at B_1 evolving to B_2

2.3 Phase Space Dynamics

Figure 2.3 shows a stroboscopic section obtained by evolving the map in Eq. (2.8) for uniformly distributed initial conditions in $x \in (-x_w, x_w), p \in (-p_c, p_c)$, where $p_c = \sqrt{2mV_0}$ is the minimum momentum required for barrier crossing. In this paper, we have chosen kick strength $\epsilon << 1$ such that the corresponding standard map displays only KAM curves. Throughout this thesis, we use the phrase "corresponding standard map" to mean Eq. (2.8) with $V_{sq}(x) = 0$. As pointed out earlier, the limit $V_{sq}(x) = 0$ reduces Eq. (2.6) to kicked rotor system. Firstly, a striking feature is the absence of invariant curves and the appearance of a mixed phase space. This is in stark contrast with the standard map which displays mostly quasi-periodic orbits for kick strengths of this order as shown in Fig. 1.1. Figure 2.3 also shows snap shots (solid circles in red) of a trajectory in between successive encounters with the

discontinuities at B. Clearly, the evolution between two successive encounters with the boundaries is confined to a trajectory that is identical with one of the quasiperiodic orbits of the corresponding standard map shown as continuous lines in the figure. In this chapter, we analyze the dynamics of our system in Eq. (2.5) in terms of the quasi-periodic orbits of the corresponding standard map. Due to $V_{sq}(x)$, particle breaks away from one quasiperiodic orbit and joins another at each encounter with the boundaries. This leads to the absence of quasiperiodic orbits and the development of mixed phase space comprising intricate chains of islands embedded in chaotic sea. Another model of non-KAM chaos, namely, the kicked harmonic oscillator also displays such intricate chain of islands [Ch87, Ch88, Be91, Za05].

We illustrate the effects of discontinuities in Fig. 2.3 by following a typical initial condition marked A_1 in the chaotic layer. This evolves to A_2 on the invariant curve C_2 of the corresponding standard map. After a long time, this point appears on the curve C_1 and goes from A_3 to A_4. After a reflection at $-x_w$, it goes from A_5 to A_6 on C_3. Then it shifts to the barrier region $(x_w, x_w + b)$ and moves on C_7 from A_7 to A_8. Depending on the winding number of the orbit in $(x_w, x_w + b)$, the particle could have gone back in to region between the barriers or escape from the finite well. In the present example, it makes its escape out of two barrier structures and its state meets the curve C_5 at A_9. Once the particle has escaped it does not encounter the potential discontinuity, responsible for its breaking from one orbit and jumping to another. As a result, its state evolves on same curve as $n \to \infty$ thereafter.

From a theoretical perspective, the absence of quasiperiodic orbits can be attributed to the non-analyticity of $V_{sq}(x)$ which violates the assumptions of KAM theorem. KAM theorem requires that the unperturbed system H_0 be analytic [Ar68] though later proofs have required just about few derivatives to exist. Thus, the non-KAM nature of the system leads to onset of chaos even for $\epsilon < 1$. However, once the particle escapes from DBS, this non-KAM potential does not affect it anymore and, thus, the system displays KAM behavior for $|x| > x_w + b$. Figure 2.3 also

shows the trajectory of a particle that escapes from DBS without suffering a single reflection. As seen in Fig. 2.3, the discontinuities at x_w and $x_w + b$ relocate the incoming particle from $C_5\,(\mu_5)$ to another orbit $C_6\,(\mu_6)$, where μ_5 and μ_6 are their winding numbers, respectively. Figure 2.4 schematically shows how the difference between the trajectories followed by particle before and after a refraction depends upon b. When a state reaches a barrier region, the loss of kinetic energy to potential energy makes it travel lesser distance than what it would travel in the absence of boundaries. As a result it breaks away from the invariant curve $C(\mu_5)$ and joins with a new invariant curve $C(\mu_6)$. The departure from the phase point at which state should reach in absence of barriers is proportional to b since the fraction of evolution time between the kicks spent with decreased kinetic energy is proportional to b. Appendix A shows that the difference between the two orbits, $C(\mu_5)$ and $C(\mu_6)$ for example, on which a state evolves before reaching and after crossing the barrier, measured as $(\mu_6 - \mu_5) \to 0$ when $b \to 0$. In other words, refraction becomes identity operation as $b \to 0$. This leads to appearance of invariant curves identical to the standard map implying KAM-like behavior, even for $|x| < x_w + b$ as shown in Fig. 2.5.

The initial conditions starting from a region defined by $|p| < p_c$ will spread in momentum space as the system evolves. Here, we will discuss some constraints applicable to phase space region these states can explore, which will actually represent the limits on the extent of mixed phase space. Let us consider first the simpler case of $b \to 0$. In the Fig. 2.5, we identify quasiperiodic orbits or invariant curves $C_{\pm}(\mu_a)$ and $C_{\pm}(\mu_b)$ of corresponding standard map, μ_a and μ_b being their winding numbers. The invariant curves $C_{\pm}(\mu_b)$ are defined in such a way that that minimum value of $|p|$ on each of them is equal to p_c. Any state evolving on a standard map orbit $C(\mu)$ with $\mu > \mu_b$, will surely approach barrier with $|p| > p_c$ for which refractive boundary conditions apply. Since for $b \to 0$ refractive boundary condition becomes identity operation, any of these state must cross the barrier evolving uninterruptedly on its original standard map orbit. Thus, the phase space beyond $C_{\pm}(\mu_b)$

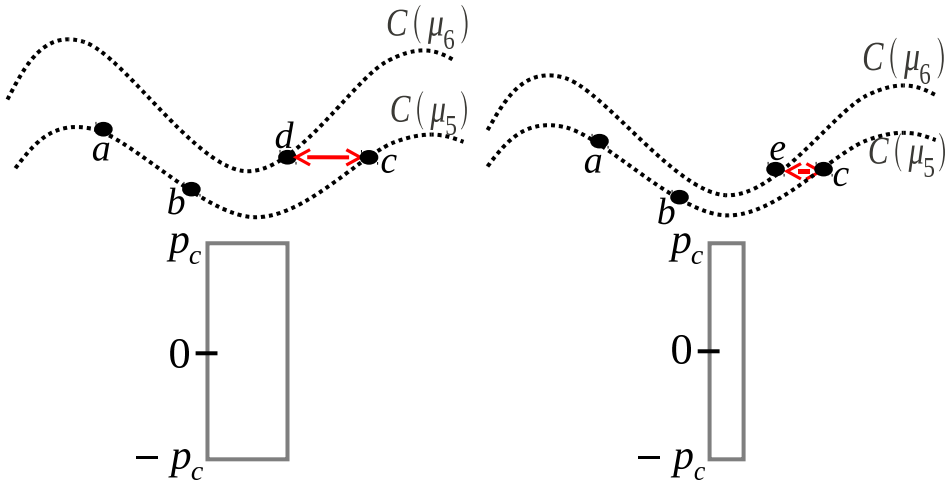

Figure 2.4: Figure shows schematically the effect of refraction at the barrier. Grey boxes represent the barrier region in phase space. The three phase points a, b and c represent the states of particle evolving on $C(\mu_5)$ starting from a in absence of barriers. Red arrows connects the phase point c, the evolving state would reach in absence of barrier, with the point d or e it actually reaches in presence of barrier after evolving between the kicks.

should be regular. At the same time, any state initially on $C(\mu)$ with $\mu \leq \mu_b$, can not cross $C_{\pm}(\mu_b)$. This is because for $b \to 0$, only transformation that can make a state jump from one quasiperiodic orbit to other, changing the winding number associated with it, is reflection. Now, a state encountering reflective boundary must have $|p| < p_c$ and therefore must appear on an orbit with $|p| < p_c$ after reflection takes place. Since none of the orbits with $\mu > \mu_b$ overlap with region defined by $|p| < p_c$, the state must appear on an orbit with $\mu < \mu_b$. This means that initial conditions lying between $C_+(\mu_b)$ and $C_-(\mu_b)$ can not diffuse beyond phase space region enclosed between these orbits.

The invariant curves $C_{\pm}(\mu_a)$ are defined in such a way that maximum value of $|p|$ on each of them is p_c. Now, any state evolving on an invariant curve with $\mu < \mu_a$ approaching barrier must have $|p| < p_c$ and will surely get reflected. However, if

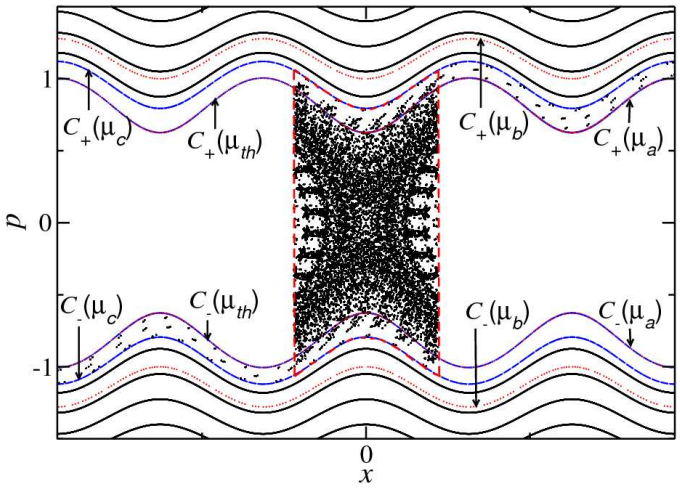

Figure 2.5: Stroboscopic plot for $b = 10^{-5}, R = 0.7, \phi = 0, \epsilon = 0.15, V_0 = 0.5$. Dashed line (in red) represents the boundary of region $\mathcal{M}$. The scatter of points between $C_+(\mu_c)$ and $C_+(\mu_{th})$ on right and between $C_-(\mu_c)$ and $C_-(\mu_{th})$ on left side of the DBS represent the particles escaping out of the well (whose initial states were in $\mathcal{M}$).

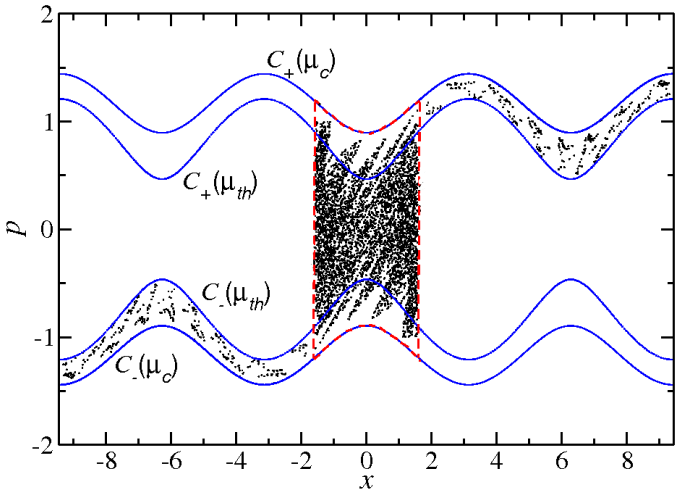

Figure 2.6: Stroboscopic plot for $R = 0.5$. All the other parameters are same as in Fig. 2.5. Dashed line (in red) represents the boundary of region $\mathcal{M}$. The scatter of points between $C_+(\mu_c)$ and $C_+(\mu_{th})$ on right and between $C_-(\mu_c)$ and $C_-(\mu_{th})$ on left side of the DBS represent the particles escaping out of the well (whose initial states were in $\mathcal{M}$).

a particle's state lies on an invariant curve with $\mu_a < \mu < \mu_b$, it might escape or not. This implies that a chaotic state must first reach the any of the invariant curves $C(\mu)$ with $\mu_a < \mu < \mu_b$ before it can escape the barriers. Thus, the quasiperiodic orbits followed by escaped particles must correspond to $\mu_a < \mu < \mu_b$.

Based on the above constraints, $C_{\pm}(\mu_b)$ should represent the border between the regular and mixed phase space. However, the real limits on the mixed phase space are represented by some $\mu < \mu_b$. This happens because as μ increases in the range $\mu_a < \mu < \mu_b$, the overlap of an invariant curve with region $p > p_c$ increases. This increases the probability that a state evolving on $C(\mu)$ approaches barrier with $|p| > p_c$ and hence its escape probability increases. Usually there exists some value of $\mu = \mu_c < \mu_b$, for which any state evolving on it will definitely escape. Then $C_{\pm}(\mu_c)$ will act like an actual border between mixed and regular phase space. Also, μ_c will act like upper limit on winding numbers of invariant curves on which escaped particles evolve. Moreover, the lower limit on μ for invariant curves followed by escaped particles can take a value larger than μ_a, say μ_{th} depending on the details of dynamics around $|p| = p_c$. Figure 2.5 shows that the escaped particles evolve on a band of invariant curves $C(\mu)$ with $\mu_{th} < \mu < \mu_c$. In this case, $\mu_{th} = \mu_a$, however, in Fig. 2.6 we see that the highest point of $C(\mu_{th})$ is clearly above p_c which is actually top point of $C(\mu_a)$ (not shown here) too. Figure 2.5 also highlights the mixed phase space region enclosed in red dashed line.

The existence of above discussed limits on the mixed phase space region and on winding numbers of escaped particles are easier to explain in case of $b \to 0$. However, they do exist in case of $b >> 0$ also. For the case with $b >> 0$, any state approaching barrier with $|p| > p_c$ may or may not escape from the DBS. As soon as it crosses the potential discontinuity at the inner edge of the barrier ($|x| = x_w$), it jumps to a quasiperiodic orbit of much smaller winding number due loss of kinetic energy to potential energy. If this new orbit happens to be close to be located across the $p = 0$ line, it may turn the evolving state back towards the well. This is apparent from small elliptic orbits in barrier region observed on section

shown in Fig. 2.3. Thus, invariant curves may get broken even beyond the region enclosed between $C_{\pm}(b)$ for $b >> 0$. However, there must exist some invariant curve $C(\mu)$ in corresponding standard map with sufficiently large μ such that if any state evolving over it approaches barrier, it will jump to another invariant curve for which direction of momentum never changes. In that case the evolving state will not get turned back into well during its evolution through barrier region and will escape from the DBS. Beyond such invariant curves, on both sides of $p = 0$, no state should get reflected or turn back into well region. Thus the region beyond these curves will be regular due to absence of repeated encounter with the barriers, although trajectory of the particle is discontinuous at barrier edges. The finite spread of chaotic layer shown in Fig. 2.3 along the momentum axis is due to existence of these regular regions on both sides of mixed phase space region. This is in contrast to general behavior of non-KAM systems in which such break down of invariant curves leads to a mixed phase space. Hence, we call this also as KAM-like behavior. Again, the real border between the regions of mixed and regular dynamics as well as limits on the μ for quasiperiodic orbits followed by escaped particles is determined by detailed dynamics of the system for a given set of parameters.

The above discussion can be be summarized as follows ; we can define a phase space region $\mathcal{M}\left(|x| < x_w + b; |p\left(x\right)| < p\left(x;\mu_c\right)\right)$, such that system has mixed phase space inside $\mathcal{M}$ in general and regular dynamics outside it. Here, $p\left(x;\mu_c\right)$ is momentum of any state on the curve $C_+\left(\mu_c\right)$ at position x. In Figs. 2.5 and 2.6, a close numerical approximation of the region $\mathcal{M}$ is highlighted by the red dashed line.

We remark that for $b \to 0$, the phase space structures inside $\mathcal{M}$ are identical to those of well map that describes the dynamics of δ-kicked particle in an infinite well [Sa01]. This is to be expected since the well map has only reflective boundaries for $|p| \leq \infty$. Further, the well map is hyperbolic for $R < 0.5$ for any $\epsilon > 0$. The Hamiltonian in Eq. (2.1) also displays complete chaos for $R < 0.5$ inside $\mathcal{M}$. This is seen in Fig. 2.6 as no regular structures are visible in this region to the

accuracy of our calculations. In fact, it can be shown that the phase space between the barriers will always be fully chaotic if force between the barriers is monotonic and increasing, *i.e.*, $-\frac{d^2V(x)}{d^2x} > 0$ throughout the region between the barriers for any arbitrary kicking potential $V(x)$. The region defined by $\mathcal{M}$ is determined by the positions of potential discontinuities $\mathbf{B}$ and $C_{\pm}(\mu_c)$. It can be shown that $C_{\pm}(\mu_c)$ will remain close to $\pm p_c (= \pm\sqrt{2mV_0})$ when $b \to 0$ for any ϵ for which standard map has mostly regular phase space. Thus, the extent of chaotic region will depend grossly on the positions **B** and height V_0 of the barriers only. This implies that it is possible to engineer chaos in a desired region by varying these parameters.

2.4 KAM-like Behavior: Role of Symmetries

In this section, we explore the conditions under which KAM or non-KAM type of dynamics can be realized in the system. In Eq. (2.1), the non-analyticity of V_{sq} violates the assumptions of the KAM theorem. Hence, generically we expect this system to display the signatures of non-KAM system such as the stochastic webs instead of quasi-periodic orbits and an abrupt transition to chaos. These features are shown in Fig. 2.7(a,c,d,f). However, we show that even in the presence of non-analyticity in $V_{sq}(x)$, quasi-periodic orbits similar to that in a KAM system can be realized, as shown in Fig. 2.7(b,e) if certain symmetry conditions are satisfied.

As argued before, until interrupted by the barriers, the dynamics is confined to a particular invariant curve of the corresponding standard map. We recall that corresponding to every trajectory C_+ of standard map with $p_n > 0$, there exists one and only one trajectory C_- with $p_n < 0$, such that a particle will evolve on these trajectories in exactly the same way but in opposite direction. Consider the (R, ϕ) pairs for which the condition

$$\pm R\pi + \phi = l\ 2\pi, \qquad l \in \mathbb{Z} \tag{2.14}$$

is satisfied. When Eq. (2.14) is satisfied, as shown in Appendix B, application of $\widehat{\mathcal{R}}_i$

takes a particle from C_+ to C_- and application of $\widehat{\mathcal{R}}_{i+1}$ brings it back to C_+. This leads to quasiperiodic behavior in which the particle is confined to a pair of tori. This quasiperiodic orbit undergoes smooth deformation, just like in a KAM system, until it breaks for large kick strengths. Hence we call this KAM-like behavior for its striking resemblance to the qualitative behavior of a KAM system. In general, there exist infinite (R,ϕ) pairs for which KAM-like dynamical behavior can be recovered in this system. In Fig. 2.7(b,e), we show the sections for $R = 1, \phi = 0$ and $R = 0.5, \phi = \pi/2$ for which KAM-like behavior is obtained. In Fig. 2.7(a,c,d,f), we also show cases where Eq. (2.14) is not satisfied and hence for $|p| < p_c$ stochastic webs and chaotic regions are seen.

Symmetry related invariant curves like C_+ and C_- are due to the symmetry of the kicking field about any $x = m\pi + \phi$ where m is an integer. It turns out that when Eq. (2.14) is satisfied, kicking field is symmetric about x_w and x_{-w}. The existence of KAM-like behavior in presence of non-analytic potential can be attributed to existence of centers of symmetry of kicking field at $-x_w$ and x_w.

2.5 Quantum Dynamics

In this section we discuss the simulations of the wave packet evolution in the system to study its quantum dynamics. We start by writing down the time-dependent Schroedinger equation corresponding to the scaled Hamiltonian in Eq. (2.6),

$$i\hbar_s \frac{\partial \psi}{\partial t} = \left[\frac{-\hbar_s^2}{2} \frac{\partial^2}{\partial x^2} + V_{sq} + \epsilon \cos x \sum_n \delta(t-n) \right] \psi. \tag{2.15}$$

The scaled Planck's constant is $\hbar_s = \frac{2\pi^2\hbar}{E_c T}$. This being a kicked system, we can obtain the one-period Floquet operator that evolve an initial wave packet over one time period T and is defined as,

$$\widehat{U} = \exp\left(-\frac{i}{\hbar} \int_t^{t+T} \widehat{H} \right). \tag{2.16}$$

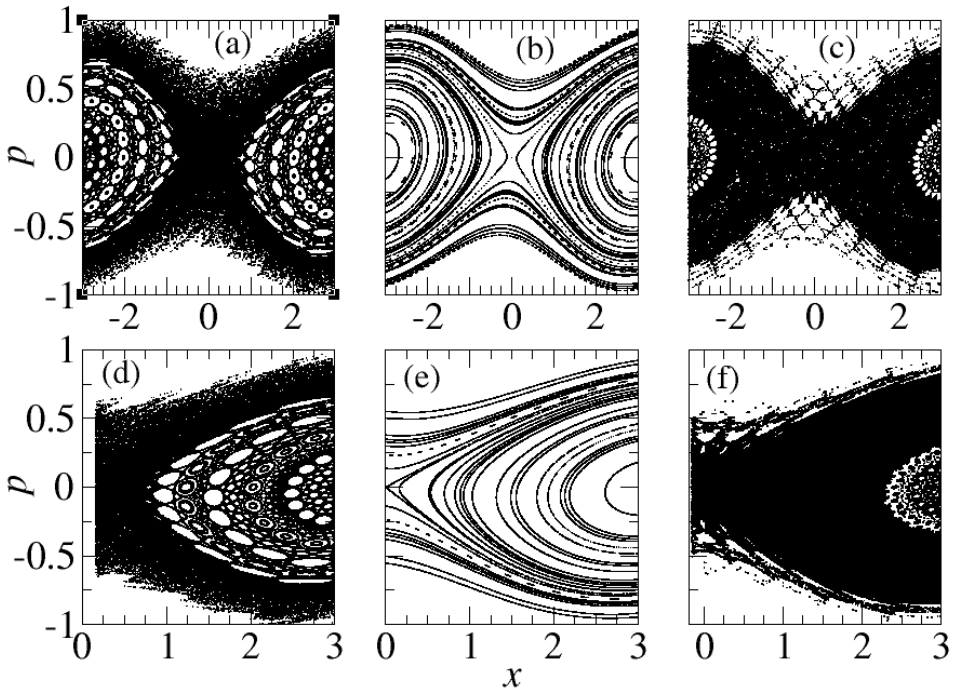

Figure 2.7: Stroboscopic Poincare section for the Hamiltonian in Eq. (2.1) showing the region $x \in (-x_l, x_r), p \in (-p_c, p_c)$ for $b = 0, \epsilon = 0.15, V_0 = 0.5$. The other parameters are (a) $R = 0.95, \phi = 0$ (b) $R = 1.0, \phi = 0$, (c) $R = 1.05, \phi = 0$, (d) $R = 0.45, \phi = \pi/2$, (e) $R = 0.5, \phi = \pi/2$ and (f) $R = 0.55, \phi = \pi/2$.

Putting $T = 1$ and replacing $\hbar$ with $\hbar_s$ and making initial time t coincide with origin of time axis, Floquet operator for scaled system defined in Eq. (2.15) becomes,

$$\widehat{U} = \exp\left(-\frac{i}{\hbar_s}\int_0^1 \left(\frac{\widehat{p}^2}{2} + \widehat{V}_{sq} + \epsilon\cos\widehat{x}\sum_n \delta(t-n)\right)dt\right). \tag{2.17}$$

Just like in case of standard map, one can divide the evolution into free evolution, but subjected to stationary potential in this case, and the kicking part. The evolution operator evolving a wave packet from a time just before a kick to just before the next kick comes out to be

$$\widehat{U} = \exp\left(-\frac{i\epsilon}{\hbar_s}\cos\widehat{x}\right)\exp\left(-\frac{i}{\hbar_s}\left[\frac{\widehat{p}^2}{2} + \widehat{V}_{sq}\right]\right), \tag{2.18}$$

such that $\psi(x,n) = \hat{U}^n\psi(x,0)$.

Since $\widehat{p}$ and $\widehat{V}_{sq}$ in Eq. (2.18) do not commute, we first divide the duration between successive kicks into $N_{\triangle t}$ small time steps and the second term of Eq. (2.18) becomes $\prod_{i=1}^{N_{\triangle t}} \exp\left(-\frac{i}{\hbar_s N_{\triangle t}}\left[\frac{\widehat{p}^2}{2} + \widehat{V}_{sq}\right]\right)$. Then, we apply the split-operator method [Ta07] to evolve the system according to which

$$\begin{aligned}&\exp\left(-\frac{i}{\hbar_s N_{\triangle t}}\left[\frac{\widehat{p}^2}{2} + \widehat{V}_{sq}\right]\right)\\ &= \exp\left(-\frac{i}{\hbar_s N_{\triangle t}}\left[\frac{\widehat{p}^2}{2}\right]\right)\exp\left(-\frac{i}{\hbar_s N_{\triangle t}}\left[\widehat{V}_{sq}\right]\right) + O(\triangle t)^2.\end{aligned} \tag{2.19}$$

We use Fast Fourier transform [Fr05] to obtain $\widetilde{\psi}(p)$ from $\psi(x)$ and vice-verse. In our calculations, we have taken $N_{\triangle t} \sim 2500$, the typical temporal step size is $O(10^{-3})$ and spatial step size is $O(10^{-4})$ to ensure that the evolved wavepackets converged to at least 6 decimal places.

From evolved wave packet, we calculate the Husimi distribution [Hu40, Ta89a]

$Q(x_0, p_0, n)$ defined by

$$Q(x_0, p_0, n) = |\langle\psi(x, n)|x_0, p_0\rangle|^2 \tag{2.20}$$

corresponding to evolved state $|x_0, p_0\rangle$ at time n to study the phase space dynamics. In this, $\langle x|x_0, p_0\rangle$ the minimum uncertainty wavepacket centered at (x_0, p_0). In terms of wavefunction, Husimi distribution can be expressed as,

$$Q(x_0, p_0, n) = \left| \int_{-\infty}^{\infty} \frac{1}{(2\pi\triangle x)^2} \exp\left(\frac{-i}{\hbar_s} x_0 x\right) \exp\left(\frac{-(x - x_0)^2}{4(\triangle x)^2}\right) \psi(x, n) dx \right|^2 . \tag{2.21}$$

Here, $\triangle x$ is the width in position space of the minimum uncertainty wavepacket centered at (x_0, p_0).

In the semiclassical regime, the dynamics in the Husimi representation mimics the classical dynamics of the system in phase space [Ta89a]. In Fig. 2.8, we show the Husimi function distribution at $n = 250$ from which one can clearly see that the density of Husimi distribution shows pattern similar to classical structures shown in Fig. 2.3.The initial wavepacket at $n = 0$ is located in between the two barriers. We choose parameters b and $\hbar_s$ for which the Husimi distribution closely resembles the classical phase space and shows that the probability density associated with the initial wavepacket will ultimately leave the barrier region by predominantly following the classical path rather than by tunnelling. Thus, the system stays in the semiclassical regime and tunnelling is largely suppressed. Quite clearly, for such a choice of parameters in the semiclassical regime, the classical dynamical features would be reflected in the quantum dynamics as well.

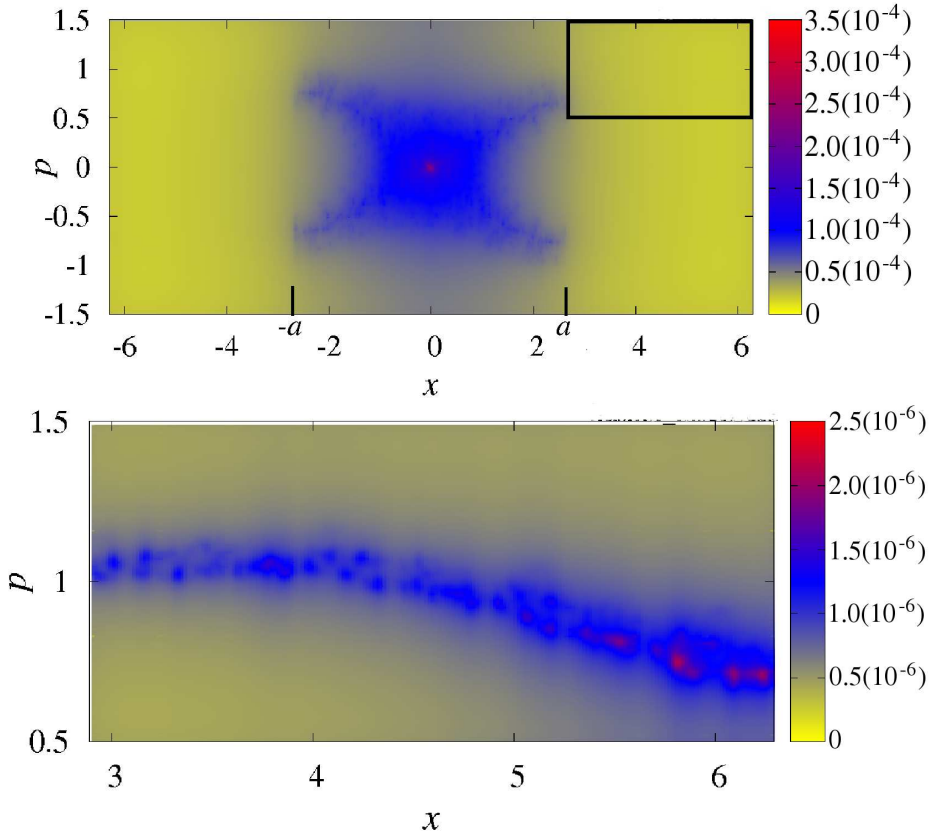

Figure 2.8: (Top) Husimi distribution for evolved wave packet. Initial wave function corresponds to $Q(x_0, p_0, n)$ sharply localized inside chaotic region around $(0, 0)$. In Grey scale version, grossly the darker areas represent the region with larger value of Husimi distribution function (for figure at the bottom as well). It shows that the Husimi function decays very steeply outside $[x_{-w}, x_w]$ and acquires negligible values compared to those for region inside $[x_{-w}, x_w]$. We have taken $\hbar_s = 0.0025$, $R = 0.85$, $b = 0.2$, $\epsilon = 0.15$, $V_0 = 0.5$, $\phi = 0$. (Bottom) Enlarged and better resolved view of inset from figure on the top shows path followed by probability density outside the barrier region.

CHAPTER 3

Kicked Particle in a Double-barrier Structure: Dynamical Features

In this chapter, we present the dynamical features in a system of kicked particle in the double barrier structure arising due to intricate interplay between non-KAM and KAM-like dynamics. These classical features also leave their imprint in the semi-classical regime of the corresponding quantum system. In particular, we study the temporal evolution of an initial distribution located inside the well region at time $n = 0$ as the periodic kicks act on the system. We take the ensemble size, *i.e.*, the number of initial states, large enough that we can study some statistical properties of the evolving phase space distributions. We report results on the following interesting dynamical features; (i) classically induced suppression of energy growth, (ii) non-equilibrium steady states, (iii) momentum squeezing and (iv) momentum pumps. All these features are important in the context of transport properties of this system.

3.1 Classically Induced Suppression of Energy Growth

In the kicked rotor model, one of the significant results is the quantum suppression of classical diffusion. For large kick strengths, the kicked rotor displays classical diffusion in energy [Re04]. In this regime, the particles tend to absorb unbounded energy. However, in the corresponding quantum system, the unbounded energy growth is arrested by quantum localization [Ch89, Iz90], an effect arising due to destructive quantum interferences and this is shown to be analogous to Anderson localization [An58, Fi82, Gr84]. This is purely a quantum phenomena. In contrast to this, in this chapter we discuss the suppression of energy growth, in the system represented by Eq. (2.1), arising due to the influence of KAM-like classical structures in phase space.

3.1.1 Mechanism of Escape from DBS

Based on the discussions in section (2.3), we have shown that there exists a region $\mathcal{M}\left(|x| < x_w + b; |p\left(x\right)| < p\left(x;\mu_c\right)\right)$ such that the system exhibits mixed phase space inside $\mathcal{M}$ and exhibits regular dynamics outside $\mathcal{M}$. Any state initially located inside $\mathcal{M}$, during the course of further evolution, is bounded by the invariant curves $C_+(\mu_c)$ and $C_-(\mu_c)$. When it escapes from region $\mathcal{M}$, it will evolve over an invariant curve $C(\mu)$ with $\mu_{th} < \mu < \mu_c$. For typical values of kick strengths $\epsilon << 1$ used in this work, we obtain a subdiffusive (mixed phase space) or diffusive (in case of full chaos between the barriers; see Fig. 3.1) region immersed in a regular region. Then, evolving particles can leak from the (sub)diffusive region into the regular one through the small window between $C_\pm(\mu_c)$ and $C_\pm(\mu_{th})$.

If we start at time $n = 0$ with a localized distribution of points in phase space all located in the (sub)diffusive region, they will begin to diffuse as kicks begin to act on them. This leads to fast growth of total energy of all the particles initially. However, this initial diffusion will get arrested because the invariant curves $C_+(\mu_c)$

and $C_-(\mu_c)$ act as dynamical barriers to diffusion in momentum space. Some of them will absorb sufficient energy and escape from the DBS. The escape of energetic particles from the DBS region will continue, however, leading to more and more absorption of energy by the particles from kicking field until all of them leave the DBS. Figure 3.1 shows stroboscopic section for a situation in which the phase space corresponding to the well region is fully chaotic and is bounded by the invariant KAM-like curves. The values p_{min} and p_{max} shows the momentum range of the particles escaping out of the well region. Momentum distribution corresponding to same set of parameters as Fig. 3.1 at times $n = 0, 50$ and 100 is shown in Fig. 3.2(a,b,c). Clearly, the momentum distribution falls within the limits imposed by $C_\pm(\mu_c)$ as shown in Fig. 3.1. All the particles escaping out of well region, lie in momentum bands corresponding to the band invariant curves lying between

$$C_+(\mu_{th}) \text{ and } C_+(\mu_c), \text{ if } p > 0, C_-(\mu_{th}) \text{ and } C_-(\mu_c), \text{ if } p < 0. \tag{3.1}$$

As the system evolves, more and more particles enter these bands.

3.1.2 Saturation of Energy Growth

Once a particle has escaped, it gets locked on to an invariant curve $C(\mu)$ with $\mu_b < \mu < \mu_c$. Hence its momentum and energy will fluctuate about the average momentum and energy of all the states lying on $C(\mu)$ and, thus, no net increase in the energy of escaped particles. Hence, any net absorption of energy should take place only through particles which are not yet escaped. Let N and N_n be the total number of particles and number of particles left in the well region at time n, respectively. Let $\langle E \rangle$ denote the mean energy of all the particles in the system. As the system evolves with time, more and more particles escape out of the well region and consequently N_n/N decreases. This leads to decrease in energy absorption rate with time. As time $n \to \infty$, $N_n/N \to 0$ which results in $\frac{d\langle E \rangle}{dt} \to 0$. This implies the existence of an asymptotic *steady state* in which momentum and, hence, en-

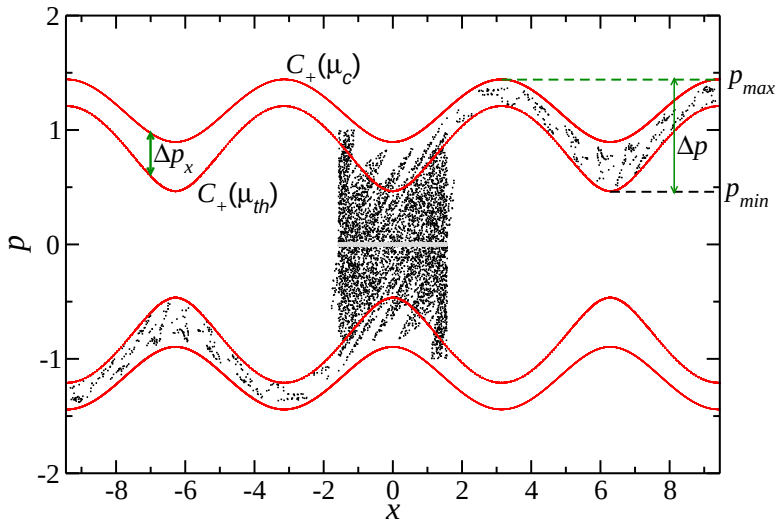

Figure 3.1: Stroboscopic section for $R = 0.5, \epsilon = 0.3, b = 0.2, V_0 = 0.5$ and $\phi = 0$. Lower and upper limits on momenta of escaped particles are represented by p_{min} and p_{max}, respectively. The width of momentum band in which escaped particles lie is given denoted with Δp. The momentum span of trajectories followed by escaped particles at a fixed value of x is represented by Δp_x. Grey strip around $p = 0$ is the region in which all the initial states were distributed uniformly.

ergy distribution converge to a stationary distribution corresponding to the situation in which all the particles have escaped out of the well. In the quantum domain, a similar steady state is obtained if the parameters, including the effective Planck's constant $\hbar_s$, are chosen to be in the semiclassical regime.

In Fig. 3.3, the classical and quantum momentum distributions are plotted for times $n = 250, 275$ and 300. The steady state behavior is seen in the nearly invariant momentum distributions for $n > 250$. As a result of this, $\langle E \rangle$ saturates to $\langle E \rangle_s$, where the $\langle . \rangle_s$ represents the mean taken over an ensemble of particles when $N_n/N \to 0$. Formally, this could be written as,

$$\langle E \rangle_s = \int_{p_{min}}^{p_{max}} g(p)\, \frac{p^2}{2}\, dp, \tag{3.2}$$

where $g(p)$ is the momentum distribution over the invariant curves with $\mu_{th} < \mu < \mu_c$. In general, $g(p)$ does not seem to have any universal form. It depends on the detailed phase space structure in the vicinity of the barrier region. Let $\sigma(p, n)$ be

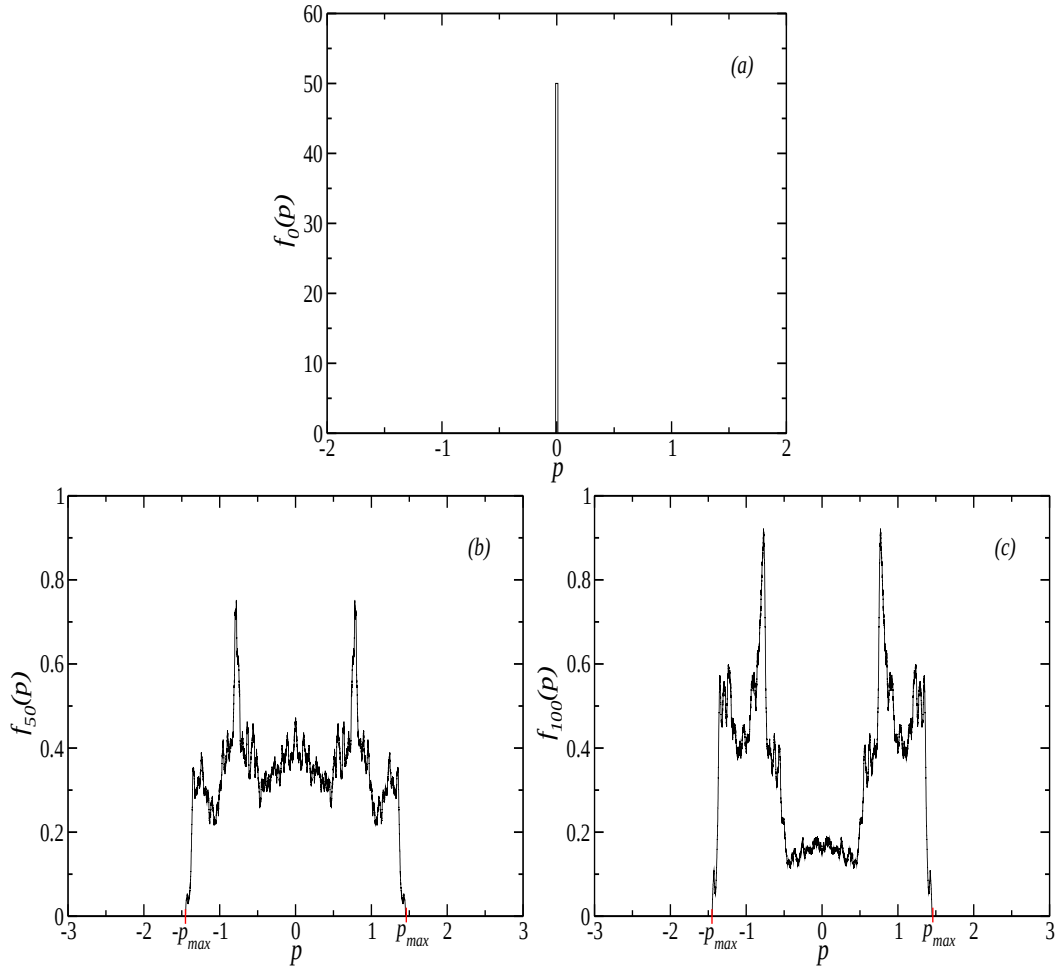

Figure 3.2: Distribution of states in momentum space at (a) $n = 0$, (b) $n = 50$, (c) $n = 100$ corresponding to parameters and initial set of states used in Fig. 3.1.

the momentum distribution of escaped particles at time n, so that mean energy of escaped particles can be defined as

$$\langle E \rangle_{out} = \int_{p_{min}}^{p_{max}} \sigma(p,n)\, \frac{p^2}{2}\, dp. \tag{3.3}$$

Obviously, as $n \to \infty$, $N_n/N \to 0$ and $\sigma(p,n) \to g(p)$. For small n, much before the steady state is reached, momentum distribution $\sigma(p,n)$ should also follow $g(p)$ determined by details of phase space dynamics for given set of parameters. However, it will exhibit large fluctuations due to small number of escaped particles. This means that before steady state is reached, $\langle E \rangle_{out}$ (not shown here) will fluctuate about $\langle E \rangle_s$. These fluctuations can be canceled by taking time average of $\langle E \rangle_{out}$ after some time of evolution when steady state is still very far. The broken horizontal line in Fig. 3.4 shows $\langle E \rangle_s$ estimated in this manner. The dashed line in the Fig. 3.4 is the mean energy $\langle E \rangle$ for the corresponding quantum system. The quantum mean energy can be calculated as,

$$\langle E \rangle_n = \frac{1}{2} \int_{-\infty}^{\infty} \widetilde{\psi}^*(p,n)\, p^2\, \widetilde{\psi}(p,n)\, dp. \tag{3.4}$$

For our choice of effective Planck's constant, the system is in the semiclassical regime and the quantum dynamics mimics the classical behavior though pronounced deviations are noticeable. Note that as $n \to \infty$, the quantum mean energy is saturated. Note that the quantum mean energy departs from the classically estimated values for $\langle E \rangle_s$. This departure from classical distributions is also seen in Fig. 3.3(a,b,c). This discrepancy between the classical and quantum mean as well as classical and quantum steady state distributions can be attributed to finiteness of effective Planck's constant. In contrast to the quantum suppression of energy growth in the kicked rotor, which arises from quantum interference effects, in our system given by Eq. (2.1), the energy growth is arrested due to classical effects.

The difference between mean energy $\langle E \rangle$ at a given time and saturated mean energy $\langle E \rangle_s$ being purely due to the fraction of particle remaining inside the well

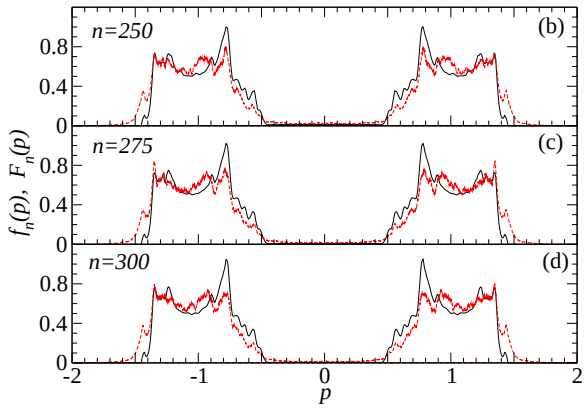

Figure 3.3: Classical (black) and quantum (red) momentum distribution at different times corresponding to parameters and initial states used in Fig. 3.1. For quantum simulation $\hbar_s = 0.0025$. These nearly identical distributions indicate that the evolved distribution has very well converged to a steady state.

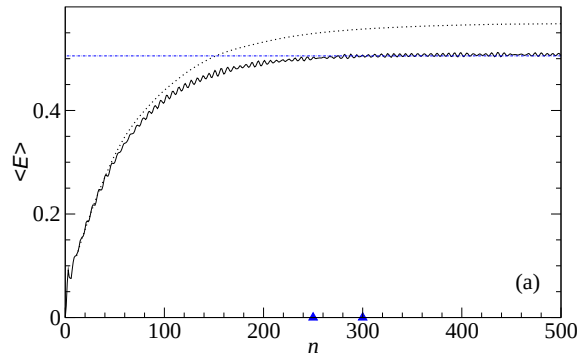

Figure 3.4: Classical (solid line) and quantum (dashed line) $\langle E \rangle$ as function of time n. Numerically estimated value of $\langle E \rangle_s$ for classical system is shown through horizontal line. Parameters are same as those for Fig. 3.3. The triangles in the x-axis are the times for which momentum distribution is drawn if Fig. 3.3

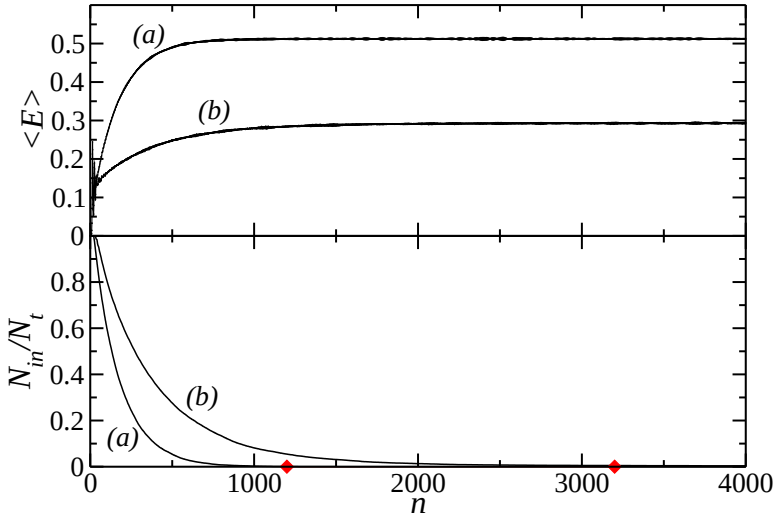

Figure 3.5: (Top) $\langle E \rangle$ vs time n for (a) full chaos between the barriers ($R = 0.5$) and (b) mixed phase space ($R = 0.8$). (Bottom) Number of particles remained inside the well region N_n vs time n for (a) full chaos and (b) mixed phase space between the barriers. Other parameters are: $\epsilon = 0.2, b = 0.2, V_0 = 0.5$ and $\phi = 0$.

region, we can write a gross relation $\langle E \rangle_s - \langle E \rangle \propto \frac{N_n}{N}$. So, faster the rate at which $\frac{N_n}{N} \rightarrow 0$, faster will be the rate at which $\langle E \rangle_s - \langle E \rangle \rightarrow 0$. For a given value of ϵ, as we move from full chaos regime to mixed phase space by changing R, rate at which particle leave well region decreases. This leads to decrease in the rate at which steady state is reached as shown in Fig. 3.5. The lower graph in Fig. 3.5 shows the fraction of particles that are left inside the well as a function of time. Clearly, faster escape rate leads to faster convergence to steady state. Since the rate of loss of particles from the DBS should increase with increase in ϵ keeping all other parameters constant, the rate at which steady state is reached also increases with increase in ϵ. This is shown in Fig. 3.6.

We emphasize that the classical phase space features underlying this classically induced suppression of energy growth, and other features discussed in this chapter, appear only for small kick strength $\epsilon << 1$ for which corresponding standard map shows regular dynamics. In the context of experiments, small kick strengths is a useful feature since it would not substantially heat up the cold atoms which constitute the test bed for kicked rotor type systems. Note that the quantum local-

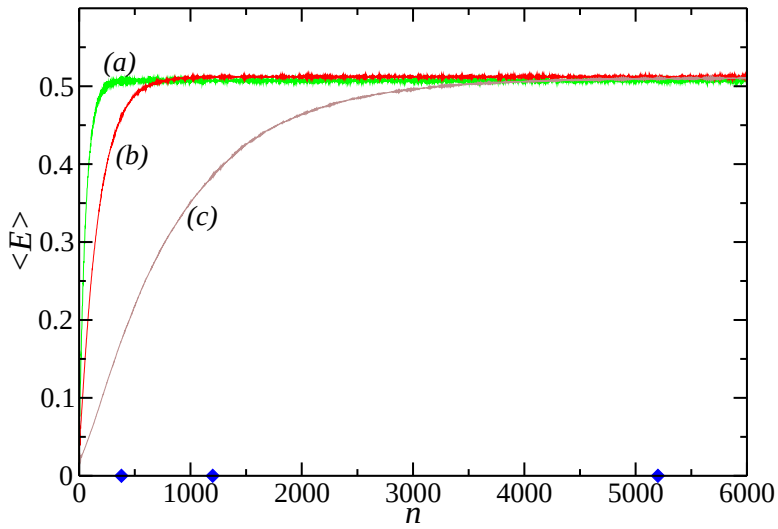

Figure 3.6: $\langle E \rangle$ vs n for (brown) $\epsilon = 0.1$, (red) $\epsilon = 0.2$ and (green) $\epsilon = 0.3$. Other parameters are: $R = 0.5, b = 0.2, V_0 = 0.5$ and $\phi = 0$.

ization in kicked rotor was achieved in the laboratory through cold atoms in optical lattices more than a decade back [Mo94, Mo95]. However, in the last few years, there were a series of experiments with BECs evolving in finite box and optical speckle type potentials which displayed suppression of energy growth due to classical mechanism [He06, Cl05, Fo05, Sc05a, Sa08]. In these experiments, in contrast to the expected localization due to quantum effects, the observed suppression of energy growth could be explained by purely classical mechanism in which energy exchange between the particles played vital role. The system studied in this thesis essentially provides a non-trivial classical localization feature in a non-interacting system. We believe this could be a useful model to understand the interplay between interactions, localization and disorder.

3.1.3 Behavior for Large Kick Strengths

In section 5, we showed evidence for suppression of energy growth leading to steady states for low kick strengths, $\epsilon < 1$. In this section, we show that the classical dynamics of our system in Eq. (2.6) displays nearly normal diffusion corresponding to an unbounded growth of energy *for large kick strengths, i.e.,* $\epsilon >> 1$. This

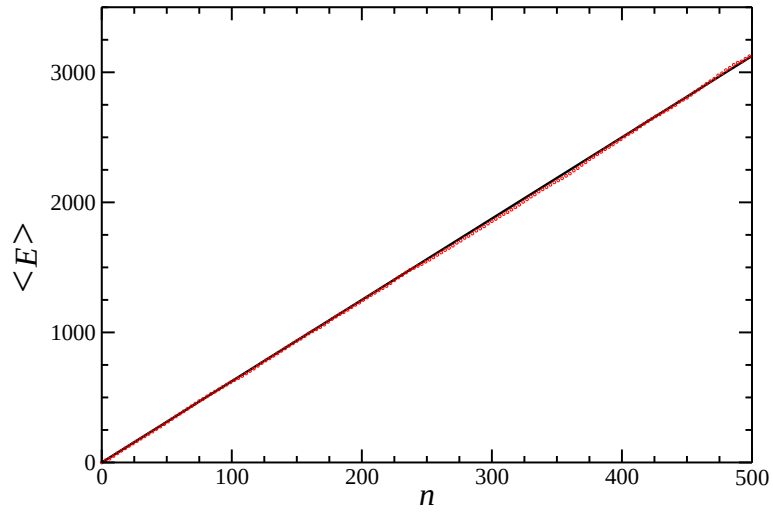

Figure 3.7: (Black line) Theoretical $\langle E \rangle$ vs n for standard map for $\epsilon = 5$. (Red circles) Numerically calculated $\langle E \rangle$ vs n for system defined in Eq.(2.6) for same value R. Other parameters for second case (red circle): $R = 0.9, b = 0.2, V_0 = 0.5$ and $\phi = 0$.

behavior is similar to the classical dynamics of the standard kicked rotor. This normal diffusion for $\epsilon >> 1$ can be explained as follows. Note that if $\epsilon < 1$ we had emphasized the role played by non-KAM and KAM-like classical structures in bringing about energy saturation effect. However, if the kick strength $\epsilon >> 1$, then most of the invariant curves in the region of KAM-like behavior are also destroyed and the chaos dominates throughout the phase space. In such a scenario, the energy growth is not arrested and, instead, we obtain the diffusive energy growth regime similar to the one that would be seen in the case of kicked rotor at same value kick strengths. This is shown in Fig. 3.7 with $\epsilon = 5.0$. At this value of kick strength, classical kicked rotor is largely chaotic. For the classical kicked rotor, energy growth is $\langle E \rangle = \frac{\epsilon^2}{4} t$ [Re04]. This estimate is also consistent with the energy growth in the case of the system in Eq. (2.6) for $\epsilon >> 1$. Hence, for large kick strengths, our model in Eq. (2.6) behaves like a kicked rotor with identical value of kick strengths. Then, the role of finite barriers becomes insignificant and classical suppression of diffusion is not observed.

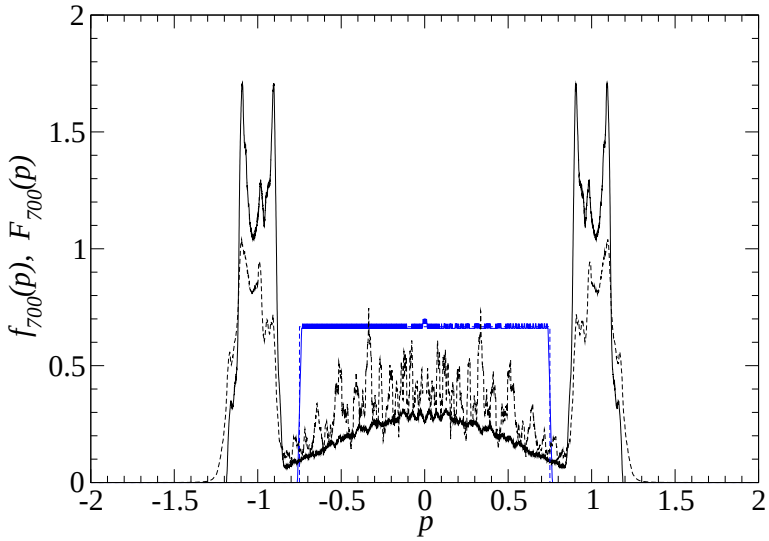

Figure 3.8: Classical (solid black line) and quantum (dashed line) momentum distributions at $n = 700$ for $R = 0.5, b = 0.2, \epsilon = 0.1, V_0 = 0.5$ and $\phi = 0$. For quantum simulation $\hbar_s = 0.0025$. Initial momentum distribution is uniform as shown by rectangular blue curve.

3.2 Momentum Squeezing

In this section we report results for what we call momentum squeezing. At the outset, we state that this phenomena is unrelated to quantum squeezing which is due to saturation of uncertainty inequality [Lo00]. As demonstrated in Fig. 3.3, the classical momenta of particles escaping from the DBS lie in finite (and narrow) width momentum bands approximately centered at $p = p_c$ and $p = -p_c$. One possible manifestation of this confinement in momentum space is momentum squeezing that can be achieved by tuning system parameters. It is possible to choose parameters such that momentum distribution of escaped particles become narrow. Figure 3.8, shows an initial broad momentum distribution in region between the barriers. This also shows evolved momentum distribution after 700 kicks, *i.e.*, for $n = 700$. By this time, a large fraction of particles have escaped from the well and the distribution has become nearly bimodal with peaks near p_c and $-p_c$. We call this phenomena momentum squeezing.

If the phase space in region $\mathcal{M}$ is fully chaotic, all the particles having initial states inside it at $n = 0$ will escape from the DBS, making region between the

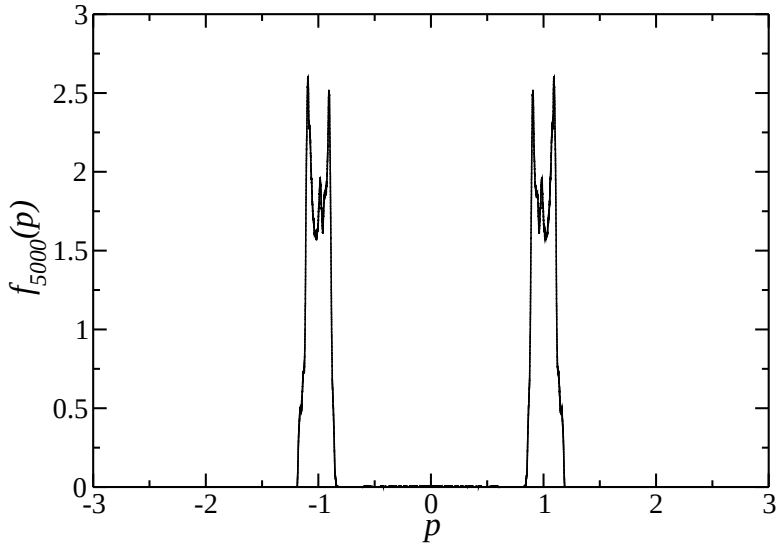

Figure 3.9: Evolved momentum distribution at $n = 5000$ for parameters and initial state same as used in Fig. 3.8. Zero density between two peaks indicate that all the particles have escaped from DBS.

barriers empty after sufficient number of kicks, and their momentum distribution will evolve into a pair of distinctly narrow bands as shown in Fig. (3.9). The chaotic layer between the barriers also ensures that the final result will be independent of the details of initial distribution. In case of mixed phase dynamics inside $\mathcal{M}$, particles having their initial states on some stable island will remain on them even as $n \to \infty$. However, all the particles with initial states lying in the chaotic sea will escape the DBS and reach the thin momentum band. In this case, only the fraction of particles remaining inside the DBS, in asymptotic regime of evolution, will depend upon the details of initial distribution of the states. The momentum band width for escaped particles will remain unaffected, however. Figure 3.10, shows two regions of phase space in which initial states were distributed. It also shows the stable islands for which states never escape even after long time of evolution if these were initially lying on them. It also shows the evolved momentum distribution for two sets of initial states. In the case for which all the initial states lie in the chaotic sea, the fraction of particles that have escaped after a given time of evolution is much larger than in the case in which many initial states lie on stable islands.

The properties of the system as a momentum squeezer can be tuned using sys-

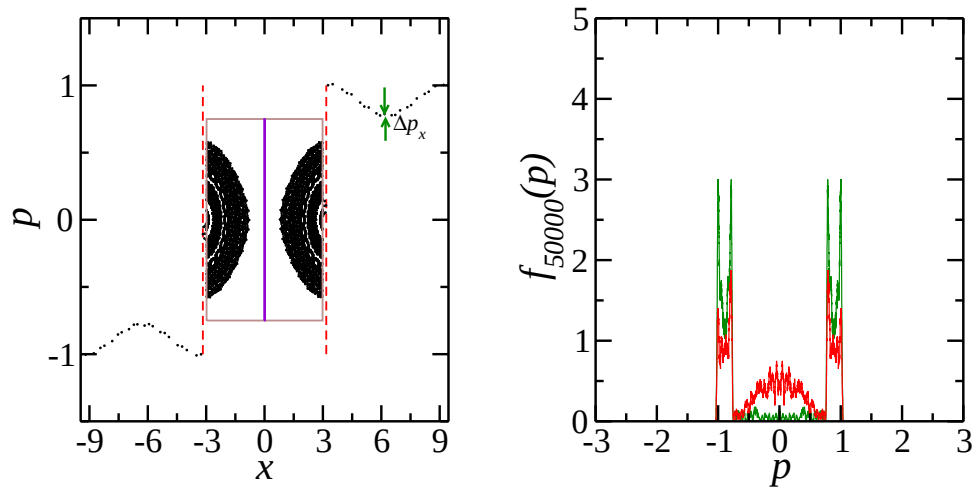

Figure 3.10: (Left) Stroboscopic section for $R = 0.95, b = 0.2, \epsilon = 0.1, V_0 = 0.5$ and $\phi = 0$. The phase space between the barriers is mixed phase space. However, the chaotic region is empty because after long evolution all the chaotic particles have escaped. Two sets of initial states (i) uniformly distributed in brown box (ii) uniformly distributed on purple line, are used to get evolved momentum distribution at $n = 50000$. The section corresponds to second set. (Right) Evolved momentum distribution at $n = 50000$ for first set of initial states is shown in green and for second set it is shown in red.

tem parameters. We have already seen that as we go from mixed phase space to fully chaotic regime between the barriers the evolved distribution becomes independent of the details of the initial distribution. Now, the width of the the momentum band Δp is, in general, very large compared to Δp_x, the width of momentum space spanned by the bundle of invariant curves on which states of escaped particles evolve, for a given x as shown in Figs. 3.1 and 3.9. In case of Fig. 3.9, it is negligible compared to the overall width of the momentum band. Hence, the width of the momentum band Δp of escaped particles Δp, in most cases, is grossly determined by the two extremal values of momenta on any individual invariant curves followed by escaped particles (see Fig. 3.10). As $\epsilon \to 0$, these invariant curves flatten and tend to become horizontal, representing constant momenta. Hence, the difference between two extreme momenta on a given trajectory decreases as ϵ decreases. As a result, band width Δp decreases as $\epsilon \to 0$, keeping all other parameters constant, as shown in Fig. 3.11.

The effect of changing V_0 will manifest through corresponding change in p_c

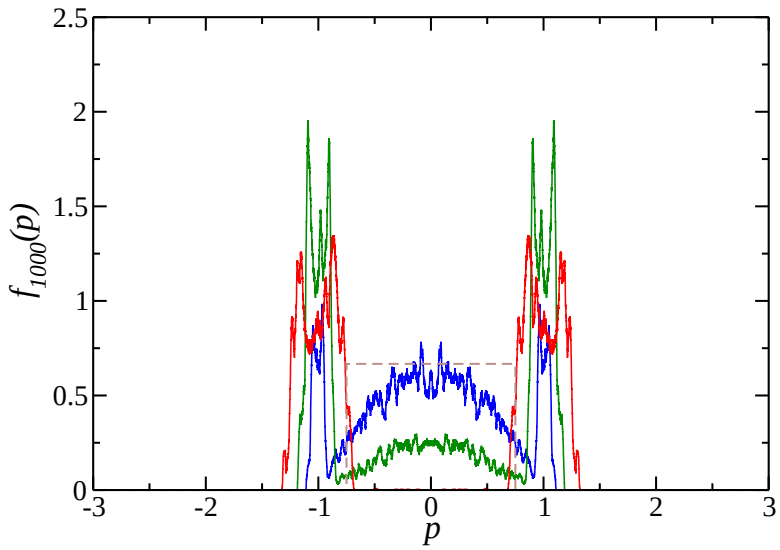

Figure 3.11: Evolved momentum distribution for $\epsilon = 0.05$ (blue), $\epsilon = 0.1$ (green) and $\epsilon = 0.2$ (red). Other parameters are: $R = 0.5, b = 0.2, V_0 = 0.5$ and $\phi = 0$.

which increases with increase in V_0. Since the momentum of escaped particles is narrowly distributed around threshold momentum p_c for $b \rightarrow 0$ or around some momentum above p_c for $b >> 0$, the peaks in momentum distribution will shift towards higher momentum on increasing p_c. This is shown in Fig. 3.12. However, fluctuations in this behavior for very small changes in p_c can not be ruled out because the exact momentum distribution depend upon details of the dynamics. Another interesting property that has very clear dependence on p_c and, hence, on V_0 is squeezing power of the system. Consider two cases in which the value of p_c differ by one period of corresponding standard map, say, $p_c = 1$ and $p_c = 1 + 2\pi$. The momentum span of the invariant curves corresponding to escaped particles turns out to be nearly same for both these cases due to periodicity of corresponding standard map. However, the chaotic layers in between the barriers has broader range in momentum space. This implies that a set of initial states with much broader initial momentum distribution can lead to bimodal distribution with same width of peaks. If the momentum values are scaled by dividing with p_c, the width of peaks in bimodal distribution is smaller as shown in Fig. 3.13. Thus, the factor by which initial broad momentum distribution can be squeezed is larger for second case. Hence,

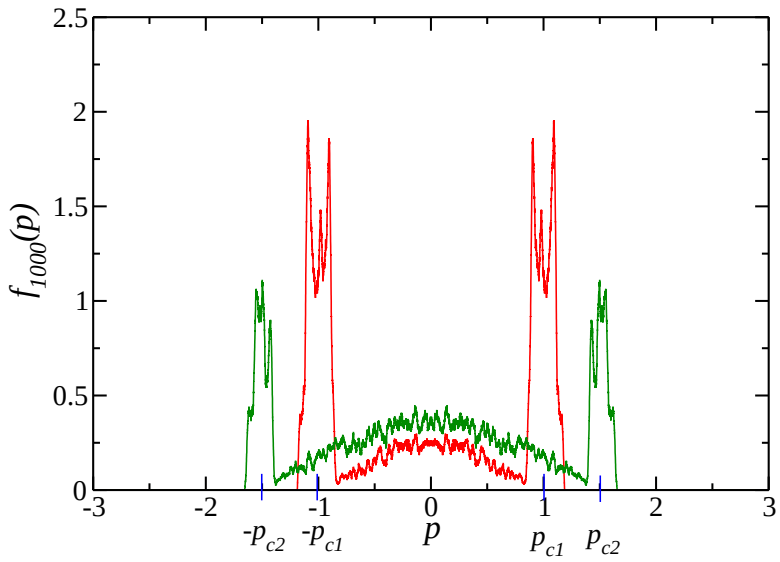

Figure 3.12: Evolved momentum distribution at $n = 1000$ for $V_0 = 0.5$ (red), $V_0 = 1.25$ (green). Other parameters are: $R = 0.5, b = 0.2, \epsilon = 0.1$ and $\phi = 0$. The threshold momenta corresponding to $V_0 = 0.5$ and $V_0 = 1.25$ are marked as p_{c1} and p_{c2}, respectively.

larger squeezing power.

Recalling the canonical transformation in section 2.1, changing scaled p_c need not necessarily imply changing the barrier height. According to the transformation $p = \widetilde{p}TE_c/\lambda\pi$ in equation array (2.4), the threshold momentum in scaled coordinate system can be expressed in terms of unscaled parameters as $p_c^{scaled}\sqrt{\frac{2V_0}{m}} = p_c\frac{2\pi T}{\lambda}$. So scaled p_c can be increased by decreasing particle mass or wavelength of kicking field or by increasing the periodicity of the kicks without changing original barrier height. However, one needs to tune other original parameters as well to keep the scaled parameters other than p_c constant. Thus, squeezing power of the system can be well controlled.

As already noted that the width of the bundles of invariant curves Δp_x, *i.e.* difference between maximum and minimum value of p at a given x across the complete set of curves, on which states of escaped particles evolve remains quite small throughout the position space.

The width of a momentum band Δp arises due to undulating nature of the invariant curves. If the system is evolved for sufficiently long enough time, the particles

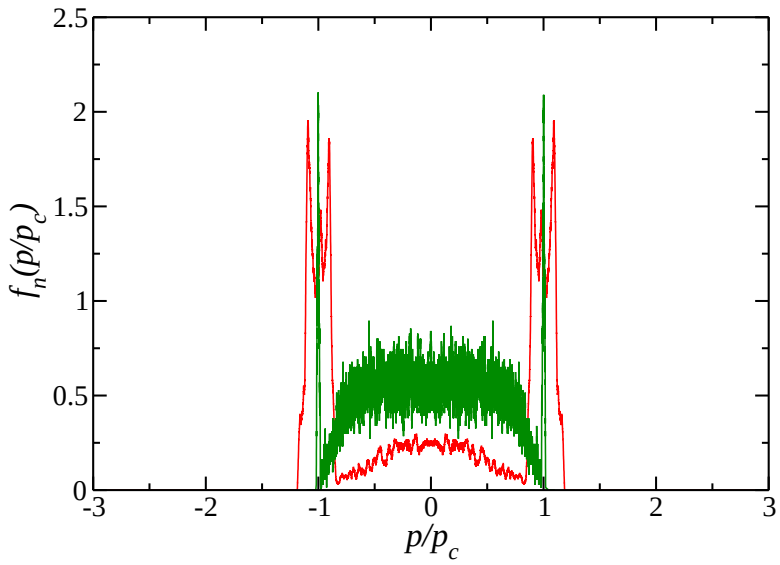

Figure 3.13: Evolved momentum distribution at time n scaled with p_c for two values of V_0 corresponding to $p_c = 1$ (red) and $p_c = 1 + 4\pi$ (green). Since the time taken for sufficient number of particles to escape from the DBS, so that their distribution can analyzed, is longer for larger p_c, we take $n = 5000$ for $p_c = 1+4\pi$ and $n = 1000$ for $p_c = 1$. Other parameters are: $R = 0.5, b = 0.2, \epsilon = 0.1$ and $\phi = 0$.

evolving over the invariant curves would have ergodically explored all the phase points on this curve. Then, long time average momentum of an escaped particle is denoted by,

$$\langle p \rangle_{\Delta n} = \frac{1}{\Delta n} \sum_{i=1}^{\Delta n} p_i. \tag{3.5}$$

The distribution of $\langle p \rangle_{\Delta n}$ for an ensemble of particles will have a width much smaller than the width of momentum distribution. Figures 3.14(a and b) show distribution of $\langle p \rangle_{\Delta n}$ for the same sets of parameters used in Figs. 3.3 and 3.10, respectively. Momentum distribution is also shown for comparison. Initial momentum distribution is identical to the one shown in Fig. 3.8. Clearly, distribution of $\langle p \rangle_{\Delta n}$ is much narrower than the momentum distribution. This one could anticipate from Poincare sections. We see in Figs. 3.1 and 3.10 that Δp_x is much smaller than Δp. The difference is quite large in Fig. 3.10. The effect of undulating nature of invariant curves, which is mainly responsible for width the momentum band, gets evened out on taking average over Δn. Then, the width of $\langle p \rangle$ is mainly determined

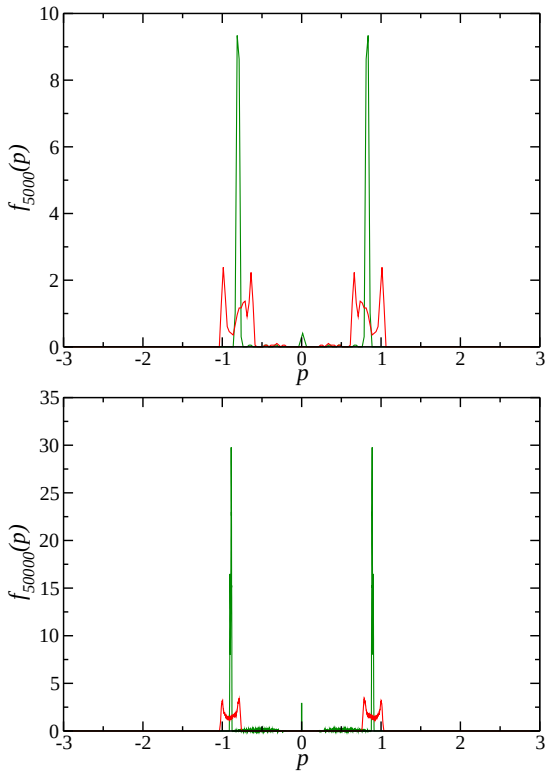

Figure 3.14: Green curves shows evolved distribution of $\langle p \rangle_{\Delta_n}$ (refer to text for its definition) at $n = 5000$ for parameters corresponding to Fig. 3.3 (left) and at $n = 50000$ for parameters corresponding to Fig. 3.10 (right). Red curves show corresponding evolved momentum distributions.

by Δp_x which is usually small. The narrowly distribution of $\langle p \rangle$ indicates that escaped particles, in long term, move much more coherently than anticipated from their momentum distribution.

3.3 Pumping Action

In this chapter, until this point, we have considered only $\phi = 0$. For $\phi = 0$, the system is spatially symmetric and the effect of this symmetry is seen in symmetric momentum distributions shown in Fig. 3.15. However, when spatial symmetry of the system is broken by taking $\phi \neq 0$, the phase space structures between the barriers become asymmetric. Figure 3.16 shows stroboscopic section for an asymmetric case ($\phi \neq 0$). The invariant curves $C(\mu)$ with $\mu_{th} \leq \mu \leq \mu_c$, on which the states

of escaping particles evolve are no longer bound to be symmetric about $p = 0$. If $\phi = 0$, μ_{th} and μ_c was identical for $p > 0$ and $p, 0$. As a result of $\phi \neq 0$, the momentum distribution becomes asymmetric. As the kicks begin to act, the classical particles evolve in to asymmetric momentum distributions even if the initial distribution at $n = 0$ was symmetric about $p = 0$. This scenario, in general, leads to $\langle p \rangle \neq 0$ for all the particles, *i.e.*, net directed motion, in the absence net bias. Please note that $R = 1.0$ in Fig. 3.15. This means that the region between the barriers contains one full wave length of cosinusoidal potential. This implies the net bias in the well region is zero, *i.e.*, $\int_{x_l}^{x_r} -\frac{dV(x)}{dx} dx = 0$, where $V(x)$ is the kicking potential at x. In this case, the net transport occurs in absence of net bias and thus, the system acts like a ratchet of finite dimension, generally known as a *pump*. The chaotic layer in the well region ensures that the pumping action is independent of the initial conditions. This is one of the few examples of pumping mechanism based on Hamiltonian chaotic dynamics. In general, the field of quantum pumps is an active area of research in condensed matter physics [Br98], almost no attention had been paid to pumping action using chaotic dynamics with the exception of the work in Ref. [Di03]. In this work, they consider square well type potentials whose walls or the depth are driven by an external field. After breaking relevant symmetries, directed currents emerge in this finite system. However, no system is known that can act simultaneously like a pump as well as momentum squeezer.

3.4 Non-equilibrium Steady State

In this section, we show that the system can support non-equilibrium steady state for fully chaotic dynamics between the barriers at x_l and x_r. We start with initial conditions uniformly distributed on a thin rectangular band around $p = 0$, as displayed in Fig. 3.17(a). As the kicking field begins to impart energy to the system, the initial distribution begins to diffuse in phase space and some of them leave the DBS region upon absorbing sufficient energy. Figures 3.17(c-d), shows phase space

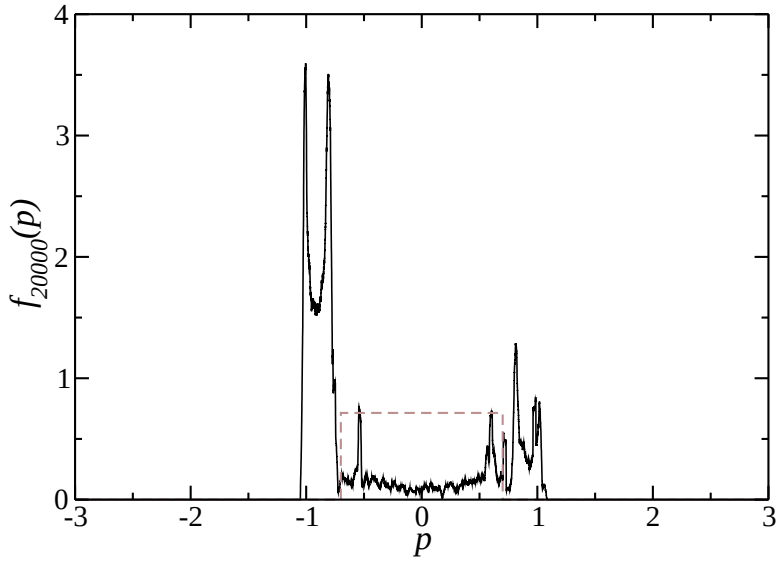

Figure 3.15: Initial (brown) and evolved (black) momentum distribution for $R = 1.0, b = 0.2, \epsilon = 0.1, V_0 = 0.5$ and $\phi = 0.5$. Asymmetric momentum distribution indicates net transport.

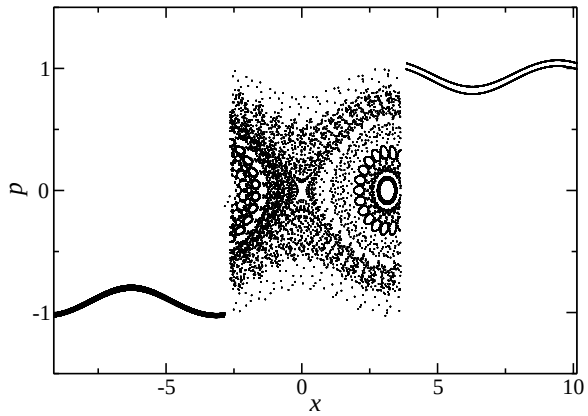

Figure 3.16: Stroboscopic section for $R = 1.0, b = 0.2, \epsilon = 0.1, V_0 = 0.5$ and $\phi = 0.5$. For non-zero ϕ the phase space is also asymmetric.

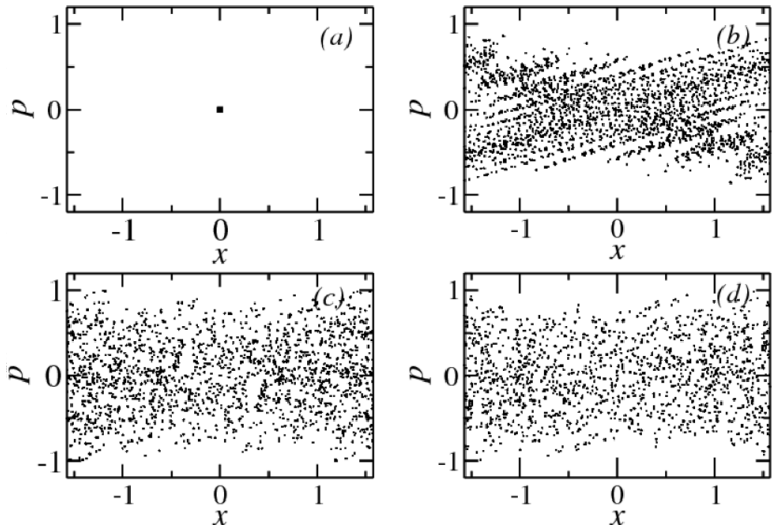

Figure 3.17: Phase space distribution of unescaped particles at (a) $n = 0$, (b) $n = 20$, (c) $n = 80$, (d) $n = 150$ for $R = 0.5, b = 10^{-5}, \epsilon = 0.15, V_0 = 0.5$ and $\phi = 0.0$. Nearly identical distributions in (c) and (d) indicate the non-equilibrium steady state.

distribution at different times of evolution. At any discrete time n, the mean energy $< E_n >$ of the particles lying inside the well is $< p^2/2 >$, where $< . >$ represents average at time n over the classical states (evolved from initial states over n kicking cycles) for which $< x_l < x < x_r$. In the corresponding quantum regime, we have

$$\langle E \rangle_{in} = \int_{-x_l}^{x_r} \psi^*(x,n)\, \frac{\widehat{p}^2}{2} \psi(x,n)\, dx \tag{3.6}$$

The effect of the operator $\widehat{p}^2$ on $\psi(x,n)$ can be calculated using fast Fourier transform and is equal to inverse Fourier transform of $p^2\widetilde{\psi}(p,n)$. Figure 3.18 shows that initially $\langle E \rangle_{in}$ increases and after a time scale t_r, $\langle E \rangle_{in}$ saturates to a constant. During this time scale, the behavior is similar to the classical diffusive regime of the standard map.

The existence of steady state can be understood as follows. For the parameters used in Fig. 3.17 the phase space in region $\mathcal{M}$ is fully chaotic. As kicks begin to act, any localized classical distribution $\rho_0(x,p)$ is quickly dispersed throughout this region. The total energy E_n of the particles in the well region increases. Simultaneously, the particles with $|p| > p_c$ leave the finite well leading to loss of energy.

As the momentum distribution broadens, the loss process becomes more and more significant leading to decrease in $\frac{d<E>_{in}}{dn}$, *i.e.* the rate at which $< E >_{in}$ is increasing. Eventually the loss of energy due to loss of particles and absorption of energy from kicks leads to $\frac{d<E>_{in}}{dn} = 0$. This must happen at a time t_r, when there is a net loss of energy but the corresponding decrease in number of particles keeps $< E >_{in}$ constant. Now, constant $< E >_{in}$ ensures that the normalized momentum as well as phase space distribution does not change as system evolves during the time interval $[t_r, t_r + \nabla]$, where $\nabla << t_r$. Invariant normalized phase space distribution leads to same statistical behavior (fraction of particles lost, fraction of energy lost etc.) at $t_r + \nabla$ as at that t_r and, thus, in turn ensures that $\frac{d<E>_{in}}{dn} = 0$ at $t_r + \nabla$ as well. This means that once $\frac{d<E>_{in}}{dn} = 0$, it freezes at this value. Hence, $< E >_{in}$ and the normalized momentum distribution will remain invariant for $n > t_r$. Figures 3.17(c and d) show nearly identical phase space distribution except that the density of particles between the barriers is smaller in later case. Figure 3.19 shows nearly identical normalized momentum distribution at two very different times after the NESS is reached.

From a physical perspective, the invariant normalized distribution in the DBS region even after continual loss of particles from energetic region can be attributed to chaotic mixing inside the well region. If the region between the barriers displays mixed phase space, the reorganization of states within the complex structures inside $\mathcal{M}$ modifies the phase space distribution. When this happens, $\frac{d<E>_{in}}{dn}$ is no longer bound to remain zero. Hence, full chaos in $\mathcal{M}$ region is essential to support NESS.

One of the factors that determine t_r is the rate at which any initial distribution of states diffuses in the chaotic region and steady state distribution shown in Fig. 3.19 is achieved. This rate increases with ϵ in general. For the present case with complete chaos, one expects this rate to be proportional to $1/\epsilon^2$, just like in the diffusive regime of standard map and hence one expects $t_r \propto 1/\epsilon^2$. Numerical results shown in Fig. 3.18 show a good agreement with this gross estimate for t_r.

Figure 3.18 shows that the quantum mean energy $\langle E \rangle_{in}$ follows the classical

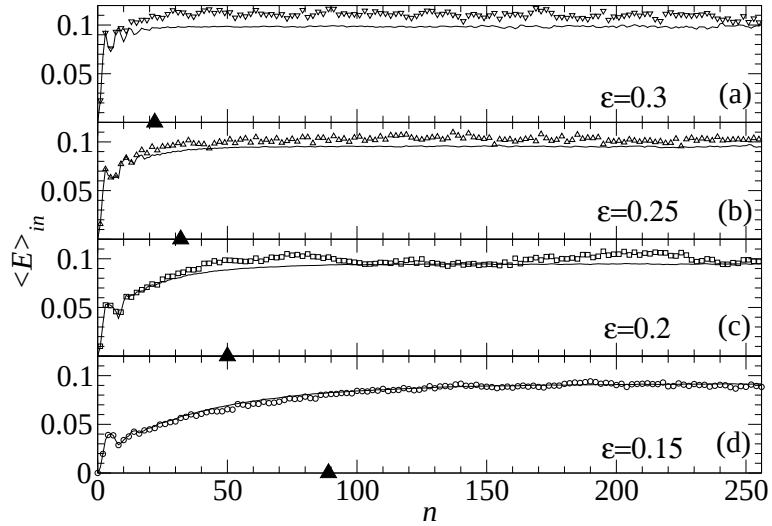

Figure 3.18: Nonequilibrium steady state in the system in Hamiltonian 2.6. The solid lines are the classical results and the symbols correspond to quantum results. The mean energy for the particles held in between the double-barrier structure $\langle E \rangle_{in}$ saturates to different constants for different values of ϵ. The other parameters are $R = 0.5, b = 10^{-5}, V_0 = 0.5$ and $\phi = 0.0$ and for quantum simulations $\hbar_s = 0.0025$. The solid symbol (triangle up) marks the time scale tr at which the system relaxes to the steady state.

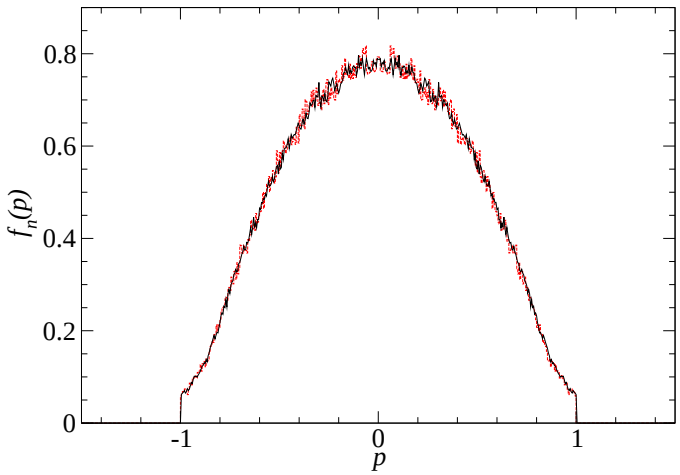

Figure 3.19: Classical steady-state momentum distribution for $\epsilon = 0.25$ at $n = 100$ solid and $n = 200$ (dashed red). The other parameters are $R = 0.5, b = 10^{-5}, V_0 = 0.5$ and $\phi = 0.0$.

curve quite closely. These results correspond to $\hbar_s = 0.0025$ and reflect the behavior in the semiclassical regime. Larger values of ϵ correspond to moving away from semiclassical regime towards purely quantum regime. Thus, we should expect quantum averages to deviate from classical averages in a pronounced manner. This is borne out by the numerical results in Figs. 3.18(a,b,c). There is current interest in quantum non-equilibrium steady states about which not much has been explored until now [Zn10]. For $\epsilon >> 1.0$, the quasiperiodic orbits of the standard map are sufficiently destroyed to allow global transport in phase space. Then, particles do not have to rely on discontinuities in V_{sq} to diffuse in phase space. This leads to unlimited energy absorption by the particles between the barriers and NESS is not supported. Then, the system essentially works like the kicked rotor in the strongly chaotic regime.

Note that all the features involving energy and momentum distributions are studied on a stroboscopic section of three dimensional phase space (x, p, t), despite the fact that the momentum and, hence, energy distribution between the kicks is not invariant in this system. This can be justified as follows. In the case of momentum squeezing and pumping it is the momentum or energy distribution of particles escaped from the DBS that is significant. Since the momenta of escaped particles do not change between the kicks, as they move in constant stationary potential, it is sufficient to consider their distribution on stroboscopic section. In the case of classically induced suppression of energy and non-equilibrium steady state, the change of sign of momentum due to reflection or change in kinetic energy of a particle due to refraction do not change the total mechanical energy of a particle. So the energy distributions will essentially remain invariant between the kicks.

CHAPTER 4

Kicked Particle in a Lattice of Finite Wells: The Classical Ratchet

From a theoretical point of view, generally ratchets are systems with infinite spatial extension and it is often achieved through use of periodic boundary conditions. Towards this goal, in this chapter, we analyze the dynamics of kicked particle in a one dimensional lattice of finite square potential wells (1DLFW). A single double barrier structure introduced in chapter 2 was useful to understand the phenomenology of non-KAM chaos and in this chapter we extend the system to the case of a periodic lattice. The primary motivation is to study the ratchet effect in non-KAM systems and also to make the connection with condensed matter systems in which transport in a periodic lattice is a problem of significant research interest (for instance, see [Fe08, Du05, Sc07]). The recipe to analyze the classical phase space of a lattice of finite square wells and study its consequent dynamical features are adopted from chapters 2 and 3. This is not entirely surprising since the potential to be studied in this chapter is built up using double barrier structure (DBS) as the basic unit. In fact, the map derived in section 1.2 can be used here along with additional periodic boundary conditions imposed due to the periodic nature of the potential. We study

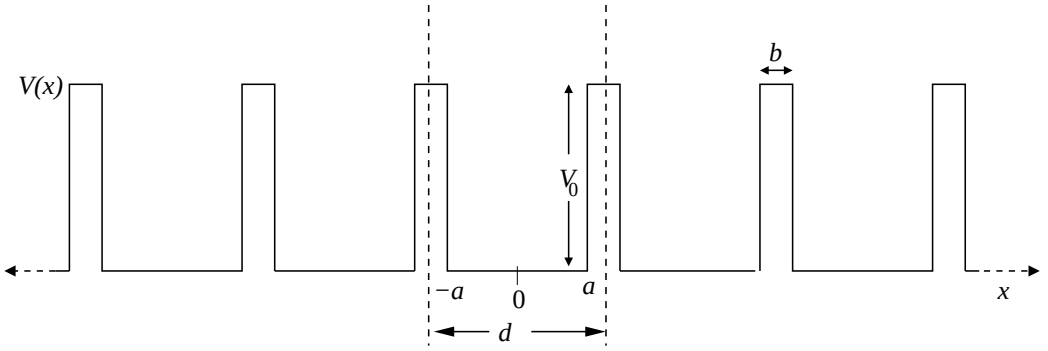

Figure 4.1: Schematic of one dimensional lattice of finite square wells.

the phase space feature of the system and its directed transport properties. Based on these results, we report on the conditions for the system to work as an effective ratchet system.

4.1 The System

The system can be described by the Hamiltonian given by

$$H = \frac{p^2}{2m} + V_{sq} + \epsilon \cos\left(\frac{2\pi x}{\lambda} + \phi\right) \sum_{n=-\infty}^{\infty} \delta(t - nT). \tag{4.1}$$

This is similar to the Hamiltonian in Eq. (2.1) except that in this case the stationary potential becomes

$$\begin{aligned} V_{sq} &= V_0 \sum_{s=-\infty}^{s=\infty} [\Theta(x + sd + b + a) - \Theta(x + sd + a) \\ &+ \Theta(x + sd - a) - \Theta(x + sd - a - b)] \,. \end{aligned} \tag{4.2}$$

Figure 4.1 shows the schematics of the stationary potential comprising a series of identical blocks of the basic DBS potential. In this form, it is similar to the Konig-Penney potential [Li80]. We consider a situation in which this series is long enough that it can practically be treated like an infinite lattice of wells as represented by summation from $-\infty$ to ∞ in Eq. (4.2).

Performing the canonical transformations as in Eq. (2.4) and separating the stationary potential from kicking and kinetic energy part, the Hamiltonian in scaled coordinate system, just as in section (2.2), can be written as,

$$H = H_0 + V_{sq} \tag{4.3}$$

In this case, the potential becomes

$$\begin{aligned} V_{sq} &= V_0 \sum_{s=-\infty}^{s=\infty} [\Theta(x + s2\pi - \phi + b + R\pi) - \Theta(x + s2\pi - \phi + R\pi) \\ &+ \Theta(x + s2\pi - \phi - R\phi) - \Theta(x + s2\pi - \phi - b - R\pi)] \end{aligned} \tag{4.4}$$

and $H_0 = \frac{p^2}{2} + \epsilon \cos(x) \sum_{n=-\infty}^{\infty} \delta(t-n)$. In this case too, the mass and the kicking period in scaled coordinate system is unity. The spatial periodicity of the stationary potential in scaled coordinates is equal to 2π. The absolute values of these parameters does not affect the qualitative dynamics of the system. Unlike the case of DBS, it must be noted that $R = 2a/\lambda$ and b are not independent parameters, but are restricted by the constraint $2R\pi + b = 2\pi$ in scaled coordinate system. This expresses the relation that periodicity of the potential is equal to the sum of the widths of the barrier and well region. For the purpose of simplicity and comparison with DBS, we use both R and b in V_{sq}. After canonical transformations, the dynamics of the system will be determined by the set of parameters V_0, ϵ, ϕ and one of the R or b.

4.2 The Phase Space Unit Cell

In the case of kicked particle in DBS, the phase space dynamics was studied on a stroboscopic section of three dimensional phase space, as it is done for the kicked rotor. The aim is to study the dynamical features in phase space, both qualitatively and quantitatively. As discussed in chapters 2 and 3, ignoring the dynamics between the kicks would not affect these features. In the context of transport properties, the change in the momentum of a particle which has not yet escaped during its evolution

between the kicks would be insignificant as the transport properties of the system are finally determined by momenta of escaped particles which does not change between the kick. However, in the periodic lattice of DBS potential, even the particles having initial states in chaotic region will never be able to escape the repeated encounter with the potential boundaries. Thus, all the contribution to $\langle p \rangle$ comes from these "unescaped" particles and, hence, can not be neglected. Since, the momenta of the particles that frequently encounter boundaries can change between the kicks if an encounter occurs between the kicks, $\langle p \rangle$ should in general be different at different times between the kicks. Therefore, in case of 1DLFW the phase space dynamics of the system on a stroboscopic section corresponding to times just before the kicks is not sufficient and one has to consider the three dimensional space (x, p, t).

Utilizing the spatial and temporal periodicity, we reduce the $(x, p, t)-$space to a *unit cell* (q, p, τ) with

$$q = \text{mod}(x \pm \pi, 2\pi) \pm (-\pi) \qquad \text{and} \qquad \tau = \text{mod}(t \pm 0.5, 1) \pm (-0.5). \tag{4.5}$$

In these expressions, " $\pm$ " represents " $+$ " for positive values of q and t and " $-$ " for negative values of q and t. Notice that the kicking sequence defined in Hamiltonian (4.4) is such that perioidic kicks act at integer times and the origin of t-axis coincides with mean position of a δ-kick. In case of DBS, it choice have been convenient. However, for now onwards we shift the origin of t-axis such that it lies in the middle of two δ-kick. With this choice, time at the mid-point between two kicks will always correspond to $\tau = 0$, time just before any kick will correspond to $\tau = 0.5_-$ and time just after any kick will correspond to $\tau = -0.5_+$. The major phase space features can be studied on some stroboscopic section of $(q, p, \tau)-$space. We need to consider three dimensional picture in (q, p, τ) space only while studying the ratchet current. The current will depend on the instant of time τ within the kicking period as discussed above.

4.3 The Classical Map

All the dynamical features can be studied on some stroboscopic section of $(q, p, \tau)-$space as in the case of DBS and standard map. To study the ratchet effect, the three-dimensional phase space can be divided in to a number of such stroboscopic sections. As we show later in section (4.7), computing $\langle p \rangle$ at a finite number of stroboscopic sections corresponding to different values of τ will be sufficient. We identify each of the stroboscopic section by the value of τ it corresponds to and denote it $S(\tau)$. Further, we denote particle's state in n-th kicking cycle on the section $S(\tau)$, that is the point on $S(\tau)$ at which trajectory of the particle intersects it in n-th period of time, by (q_n, p_n, τ). Now, to study the dynamics on a particular stroboscopic section $S(\tau)$, we derive a map that will relate a state (q_{n-1}, p_{n-1}, τ) with (q_n, p_n, τ).

To begin with, we consider $\tau = 0.5_+$, corresponding to the time just before a kick. We recall that in case of DBS we derived the map in Eq. (2.8) for studying stroboscopic section (just before a kick) by separating out the effect of H_0 and V_{sq}. In that case, τ did not play a significant role because we were concerned only with one of the many possible sections. In the same spirit, the dynamics of the system governed by Hamiltonian (4.3) can be studied using following map:

$$\begin{aligned} p_n &= p_{n-1} + \epsilon \sin(x_{n-1}), \\ x_n &= x_{n-1} + p_n, \end{aligned} \tag{4.6a}$$

$$\begin{pmatrix} p_n \\ x_n \end{pmatrix} \rightarrow \widehat{\mathcal{R}} \begin{pmatrix} p_n \\ x_n \end{pmatrix} \tag{4.6b}$$

$$\begin{pmatrix} p_n \\ x_n \end{pmatrix} \rightarrow \begin{pmatrix} p_n \\ \text{mod}(x_n, 2\pi) \end{pmatrix}. \tag{4.6c}$$

The system is evolved under the action of H_0 using Eq. (4.6a) and the effect of potential discontinuities is incorporated through Eq. (4.6b). However, there

is an additional transformation given in Eq. (4.6c) that implements the periodic boundary conditions. The operator $\widehat{R}$ is identical to that defined in section (2.2). We recall that the first of two difference equations in 4.6a describes the evolution of a state from the time just before the kick to time just after it. The delta kicks have infinitesimal width along time axis and so there is no change in the position of the particle during a kick. The momentum of particle changes due to energy absorbed from kicking field. During the rest of the evolution until the next kick happens, the momentum of a state evolving under H_0 remains constant and its position changes. The second difference equation, which largely governs the evolutions between the kicks, is the one in which the effect of boundary conditions through Eq. (4.6b) is to be incorporated.

Now, we consider the case of $\tau = 0.0$. This corresponds to time instants at the mid-point between two consecutive kicks. In this case, the kicking cycle does not begin with a change in momentum followed by the free evolution subjected to boundaries. Instead, there are two parts for free evolutions, one before and one after the kick. Consequently, the corresponding map that will evolve (x_n, p_n) over one time period on the stroboscopic section $S(0)$ should contain two difference equations similar to the second one in the pair of Eqs. (4.6a), each followed by boundary conditions. Thus, we obtain the map as,

$$x_n = x_{n-1} + \nabla^b p_{n-1}, \tag{4.7a}$$

$$\begin{pmatrix} p_n \\ x_n \end{pmatrix} \rightarrow \widehat{\mathcal{R}} \begin{pmatrix} p_n \\ x_n \end{pmatrix}, \tag{4.7b}$$

$$\begin{pmatrix} p_n \\ x_n \end{pmatrix} \rightarrow \begin{pmatrix} p_n \\ \text{mod}(x_n, 2\pi) \end{pmatrix}, \tag{4.7c}$$

$$p_n = p_{n-1} + \epsilon \sin(x_n), \tag{4.7d}$$

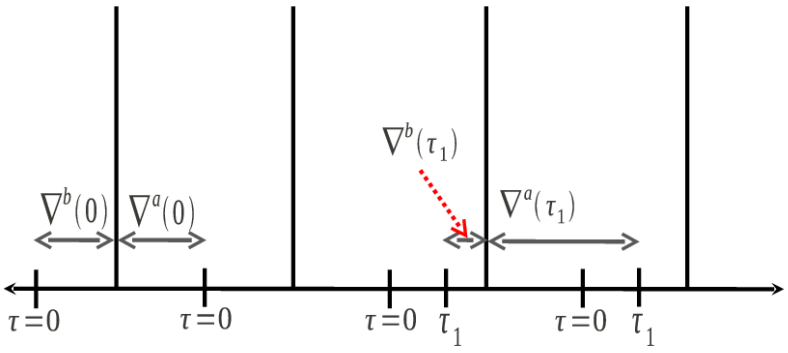

Figure 4.2: Periodic series of δ-kicks. Positions of vertical line represent the times at which kicks act. $\nabla^b(0)$ and $\nabla^a(0)$ represent the durations of free evolutions before and after the kick for $\tau = 0$. $\nabla^b(\tau_1)$ and $\nabla^a(\tau_1)$ represent the durations of free evolutions before and after the kick for $\tau = \tau_1$.

$$x_n = x_n + \nabla^a p_n, \tag{4.7e}$$

$$\begin{pmatrix} p_n \\ x_n \end{pmatrix} \rightarrow \widehat{\mathcal{R}} \begin{pmatrix} p_n \\ x_n \end{pmatrix}, \tag{4.7f}$$

$$\begin{pmatrix} p_n \\ x_n \end{pmatrix} \rightarrow \begin{pmatrix} p_n \\ \text{mod}(x_n, 2\pi) \end{pmatrix}. \tag{4.7g}$$

In this map, Eqs. (4.7a) and (4.7e) correspond to free evolution parts, one before the kick and one after the kick. The effect of kick is incorporated through Eq. (4.7d). In this ∇^b and ∇^a represent the durations of free evolution before and after the kick for evolution. For $\tau = 0.0$, $\nabla^b = \nabla^a = 0.5$. In general, we have

$$\tau = |\nabla^b| - |\nabla^a|. \tag{4.8}$$

The map in Eqs. (4.7) can be used for any value of τ by making appropriate choices for $\nabla^b(\tau)$ and $\nabla^a(\tau)$, where (τ) is used to generalize the notations for arbitrary values of τ. Figure 4.2 shows free evolution parts about a kick for two values of τ.

In fact, the above recipe can be generalized to evolve any state over one period of kicking cycle for any periodic series of delta kicks. Consider a kicking cycle shown in Fig. 4.3. The figure shows a kicking cycle that contains two unequally spaced kicks in each period. Different heights of vertical line indicate that the strengths of two kicks lying in same cycle are unequal. We use this kind of kicking cycle in section (4.5) to break the temporal symmetry of the system, as this series of kicking cycle does not have any center of symmetry. However, we keep the spatial variation of kicking field same as in Hamiltonian in Eq. (4.1). Mathematically, this new kicking field can be written as

$$V(x,t) = \cos\left(\frac{2\pi x}{\lambda} + \phi\right)\left(\epsilon_1 \sum_{n=-\infty}^{\infty} \delta(t - nT - t1) + \epsilon_2 \sum_{n=-\infty}^{\infty} \delta(t - nT)\right), \tag{4.9}$$

and in scaled coordinate system the kicking field becomes

$$V(x,t) = \cos(x)\left(\epsilon_1 \sum_{n=-\infty}^{\infty} \delta(t - n - t1) + \epsilon_2 \cos(x) \sum_{n=-\infty}^{\infty} \delta(t - n)\right), \tag{4.10}$$

where t_1(scaled)=$\frac{t_1\text{(original)}}{T}$ and all other scaled coordinates are related with the original according to canonical transformations in Eq. (2.4).

Now, for above two kick cycle, different values of τ would mean different sequence of kicks and free evolutions as shown in Fig. 4.3. We define a kicking sequence in terms of $\epsilon_j(\tau)$, $\bigtriangledown_j^b(\tau)$ and $\bigtriangledown_j^a(\tau)$. Here $\epsilon_j(\tau)$ denotes the strength of j-th kick in sequence corresponding to a given τ, $\bigtriangledown_j^b(\tau)$ and $\bigtriangledown_j^a(\tau)$ denote the free evolution times before and after the j-th kick. A state (x_n, p_n, τ) can be evolved for such a sequence of kicks and free evolutions in a manner analogous to one in which a state is evolved through a sequence of free evolution before a kick, kick and free evolution after the kick in Eq. (4.7) for single kick cycle.

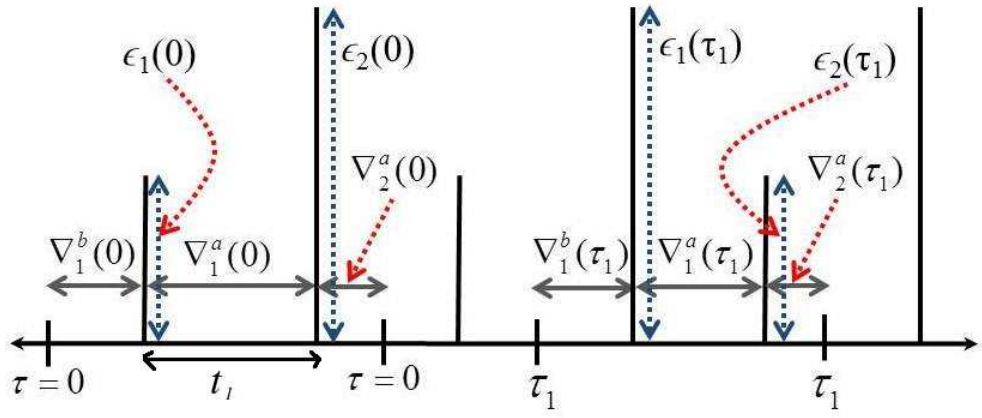

Figure 4.3: Periodic cycle of δ-kicks. Each cycle contains two kicks of unequal strength. Positions of vertical line represent the times at which kicks act and their heights represent their strengths. The sequences of the kicking and free evolution parts are shown for $\tau = 0$ and $\tau = \tau_1$.

4.4 Phase Space Features

For the Hamiltonian in Eq. (4.1), the choice $\epsilon = 0$ is the integrable limit. The momentum $|p|$ and hence the energy $p^2/2$ are the constants of motion. It is possible to transform the system to action-angle variables for $\epsilon = 0$. For $\epsilon > 0$, the phase space typically displays mixed dynamics, a direct consequence due to multiple reflections and refractions of the particle with the non-analytic potential boundaries. It must be emphasized that the mixed phase space region in between the barriers does not display invariant curves as would be expected for a non-KAM system. This is borne out by the section shown in Fig. 4.4.

As shown for the case of DBS in Fig. 2.3, in the periodic lattice too, a kicked particle evolves over the invariant curve $C(\mu)$ representing a quasiperiodic orbit of the corresponding standard map (with $V_{sq} = 0$) until it encounters potential discontinuity. In this, μ is the winding number of the invariant curve. Moreover, the periodic boundary conditions applied at the potential boundary does not break away a state from $C(\mu)$ as the underlying standard map itself is periodic. However, the repeated reflections and refractions at the potential discontinuity leads to a particle

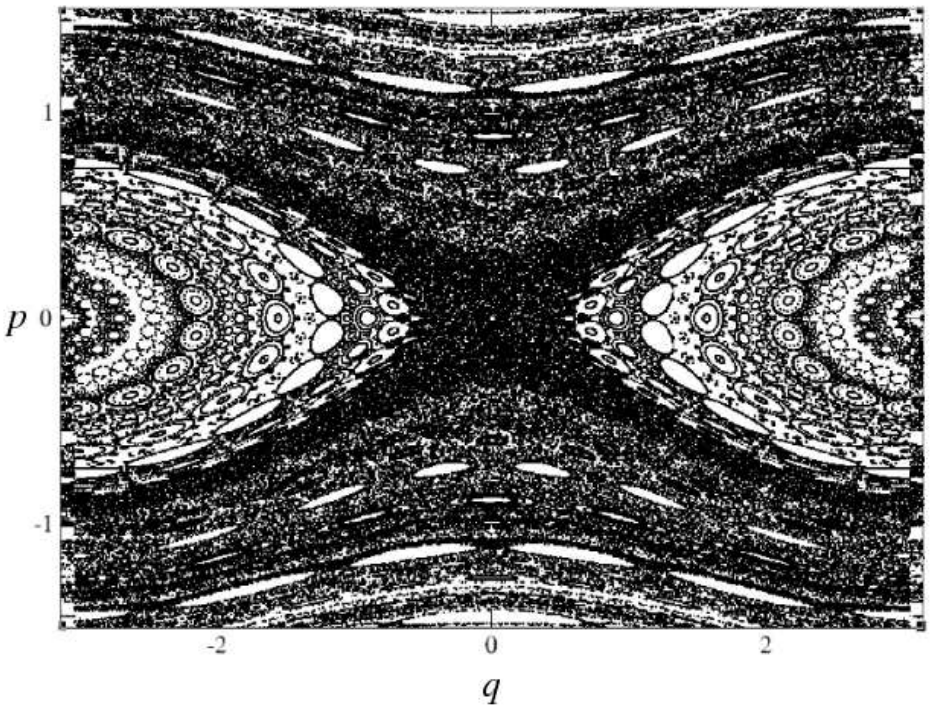

Figure 4.4: Stroboscopic section corresponding to $\tau = 0$, i.e. $S(0.0)$, for $b = 0.2, \epsilon = 0.15, \phi = 0$ and $V_0 = 0.5$. System exhibits mixed dynamics in all parts of phase space.

being kicked from one invariant curve to another. This results in mixed phase space region as shown in Fig. 4.4. Due to an array of potential barriers, the particle can never escape from the whirl of reflection and refractions, unless $b \to 0$ for which refraction becomes an identity operation as discussed in chapter 2. This is in strong contrast with the case of DBS. In DBS, a particle that has once crossed a barrier executes regular motion on an invariant curve leading to KAM-like region in phase space. This region encloses a mixed phase space or chaotic layer in phase space.

In contrast to this, in the case of lattice of square wells, there is no region in which the system can exhibit KAM-like behavior. Thus, the mixed dynamics inside the well region comprising both chaos and quasiperiodic orbits prevails throughout the phase space as the bounding KAM-like curves do not exist along coordinate or momentum axis. As a result of this, a distribution of points at time $n = 0$ starting from the chaotic sea will diffuse in phase space in the absence of dynamical bounds. However, the rate of diffusion may vary with the region of phase space and the choice of parameters and, in some case, can get significantly suppressed. Figure 4.5 shows stroboscopic section $S(0.0)$ at four different times. Clearly, the spread of phase points continues even in regions well beyond $|p| = p_c$. As a result of this spreading, the energy of the system grows continuously with time as shown in Fig. 4.6.

In the limit $b \to 0$, the refraction does not practically affect the invariant curve on which state of a particle is evolves. Thus the trajectory of a particle whose state evolves on any of the invariant curve for which reflection is not possible should remain unaffected in the presence of potential barriers. In case of DBS, innermost of such curves were identified as $C_{\pm}(\mu_c)$ for spatially symmetric case. We denote them by $C_{-}(\mu_c)$ and $C_{+}(\mu_c)$ for current system too. Obviously, the phase space region beyond $C_{\pm}(\mu_c)$ will be similar to that of the corresponding standard map. This region is mostly populated by quasiperiodic orbits which break only for very high kick strengths. Thus the current system also displays KAM-like dynamics in regions beyond $C_{\pm}(\mu_c)$. In contrast to DBS case, R and b are not independent in

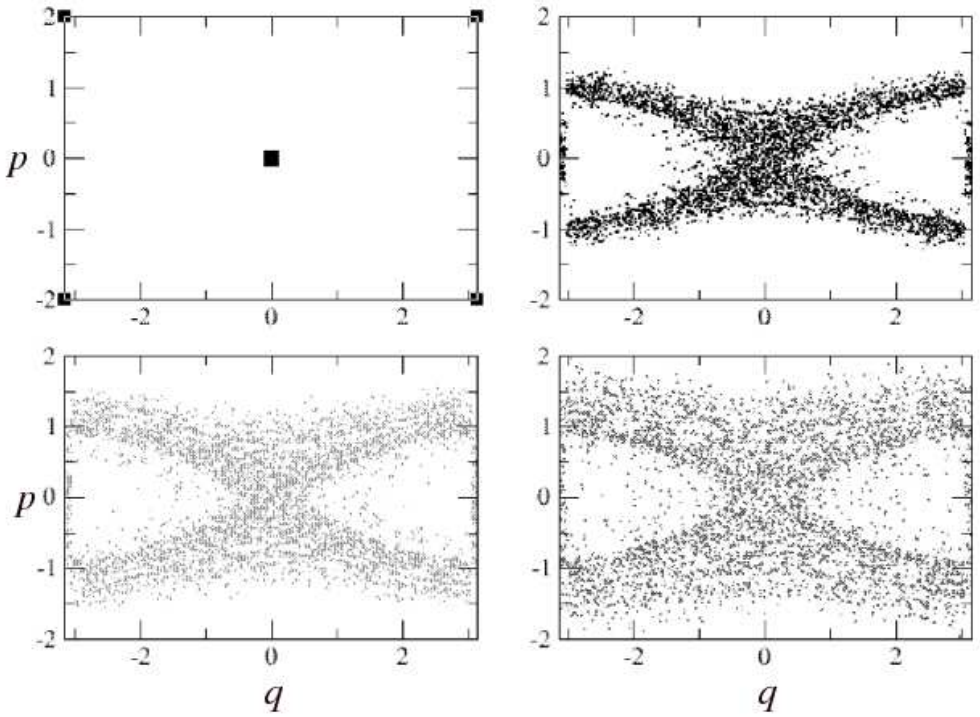

Figure 4.5: Evolving set of initial states shown on Stroboscopic sections $S(0.0)$ for parameters same as for Fig. 4.4 at (a) $n = 0$, (b) $n = 50000$, (c) $n = 100000$, (d) $n = 200000$. For this all the initial states were taken on a small region around (0,0) as shown in (a).

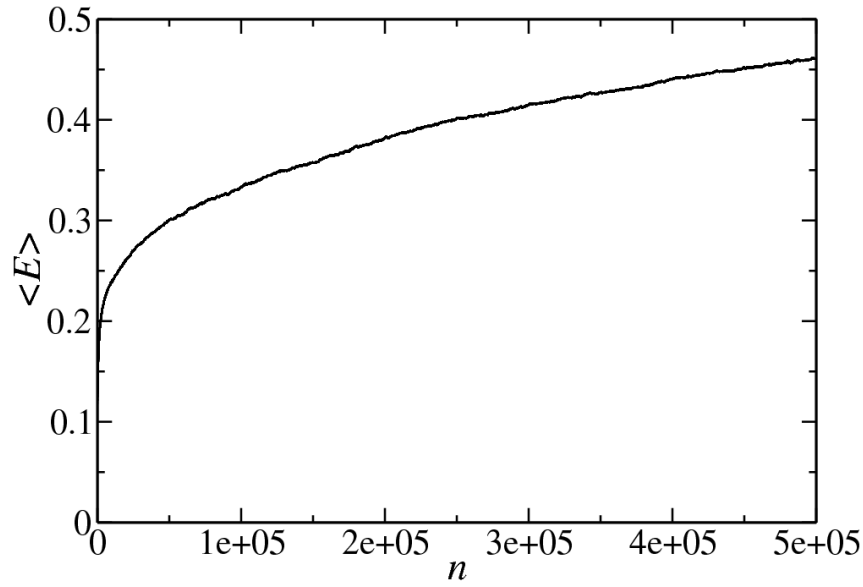

Figure 4.6: Due to continual spread in phase space as shown in Fig. 4.5, the mean energy $\langle E \rangle$ of all the particles keeps increasing. Parameters are same as in Figs. 4.4 and 4.5.

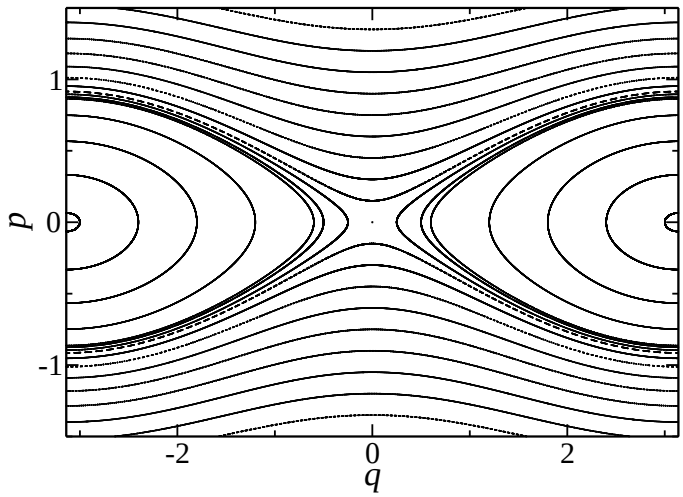

Figure 4.7: Stroboscopic section $S(0.0)$, for $b = 10^{-5}, \epsilon = 0.15, \phi = 0.0$ and $V_0 = 0.5$. It shows that the phase space is regular if $b \to 0$, as well as $\phi = 0$.

case of 1DLFW. Since $2R\pi + b = 2\pi$, as $b \to 0$, $R \to 1$. For spatially symmetric case, *i.e.*, if $\phi = 0$ and $R = 1$, Eq. (2.14) is satisfied for which the dynamics between the barriers is regular even in the region enclosed between $C_{\pm}(\mu_c)$. This is shown in Fig. 4.7. However, for spatially asymmetric case, *i.e.*, for $\phi \neq 0$, the condition given by Eq. (2.14) is not satisfied and phase space displays a region of mixed dynamics trapped between regular regions as shown in Fig. 4.8. Thus, for $b \to 0$, it becomes possible to have a diffusive phase space region sandwiched between two non-diffusive regions.

Now, if we start at time $n = 0$ with an initial distribution of points in the region defined by $|p| \leq p_c$ between the barriers, they will start spreading in phase space as the kicks begin to act. However, the spread in the momentum space gets arrested at the invariant curves that separate the regular and chaotic regions. As a result, the energy growth in the system gets arrested and system reaches a steady state as shown in Fig. 4.9.

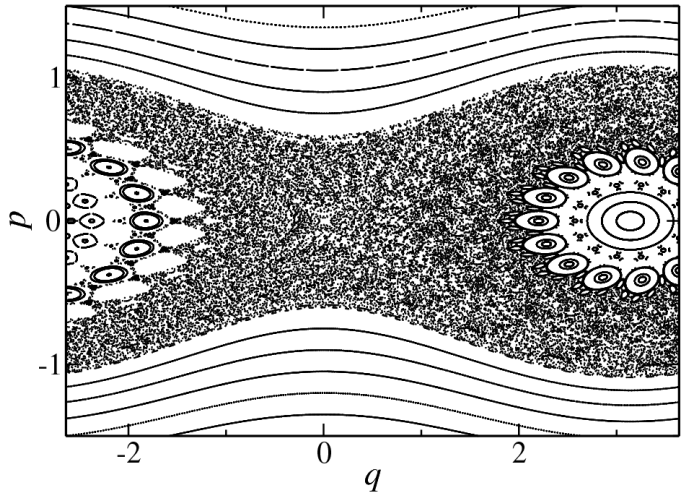

Figure 4.8: Stroboscopic section $S(0.0)$, for $b = 10^{-5}, \epsilon = 0.15, \phi = 0.5$ and $V_0 = 0.5$. It shows that the phase space comprises mixed dynamics region trapped between two regular regions for $b \to 0$.

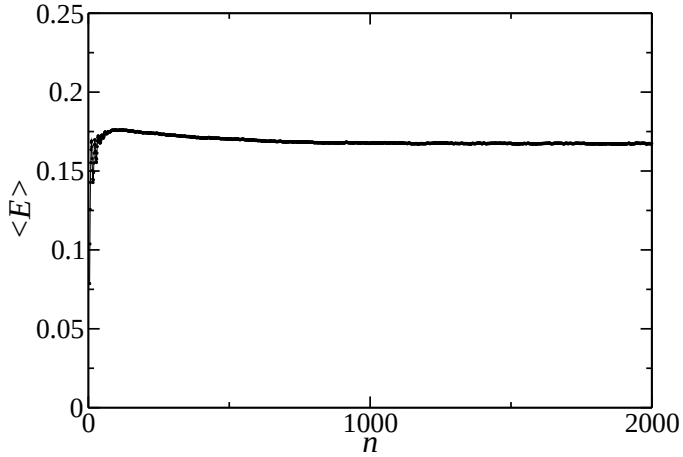

Figure 4.9: Due to trapping of mixed phase space region between the regular regions (see Fig. 4.7), the growth of energy gets arrested after some finite time of evolution. Parameters for this figure are same those for Fig. 4.7

4.5 The Classical Ratchet Effect

In this section, we study the directed transport in the absence of net bias, *i.e.*, the ratchet effect in the system of kicked particles in 1DLFW. One indicator of ratchet mechanism is that the ratchet current $\langle p \rangle \neq 0$ for an ensemble of initial conditions. We take a large set of initial conditions and calculate $\langle p \rangle$ as a function of time for different choices of parameters. Then we study the effect of spatio-temporal symmetries on the ratchet current. We start with $b \to 0$ and later show the effect of finite b.

For $b \to 0$, the system has "ideal" phase space feature for the typical parameter regime we deal with. In chapter 2, we discussed that for $b \to 0$, the mixed phase structures are identical to those of well map [Sa01]. That applies to case of periodic lattice also, as the additional periodic boundaries as such can not change the phase space features as long as $b \to 0$. In case of lattice of finite wells, like in the case of DBS, refraction takes place for $|p| > p_c$. This refraction is a significant distinction between well map and system defined in Eq. (4.1). However, refraction is equivalent to identity operation as $b \to 0$. Hence, the only reflections taking place at boundaries are responsible for breaking of KAM-tori. So these broken KAM-tori should generate same structures in phase space as in case of well map. Please note that in case of well map all the KAM-tori are broken (provided R is not an integer), but in case of our lattice of well or DBS with $b \to 0$ only a subset is affected. With $b \to 0$, we take $R < 1$, for which the broken KAM tori (due to effect of barriers) in the well region should lead to chaotic orbit except around the principal resonance region, *i.e.*, around stable fixed points at $(-\pi, 0)$ and $(\pi, 0)$, as shown by Sankaranarayanan *et. al.* [Sa01, Sa01a], for the kicked particle in infinite potential well. A hierarchical structure comprising chain islands is generated around $(x_l, 0)$ and $(x_r, 0)$, where x_l, x_r are the left and right boundaries of the potential well. Now, we choose V_0 such that these chains of islands never overlap with the transporting region $(|p| > p_c)$ and, hence, can not directly contribute to net transport. This translates to mean that the phase space accessible to initial states,

corresponding to energies below the threshold V_0, consists of a chaotic layer and possibly stable islands around $(x_l, 0)$ and $(x_r, 0)$ lying completely inside $[-p_c, p_c]$. The section shown in Fig. 4.7 corresponds to such a scenario only. Any initial state lying on any of those stable islands will remain confined to that and, hence, can not contribute to net directed motion. So the ratchet current will be determined by the $\langle p \rangle$ of the chaotic layer which will be independent of initial conditions. When the appropriate spatio-temporal symmetries are broken, we generically expect $\langle p \rangle \neq 0$. At the same time, the steady state ensures that the ratchet current does not get diluted due to continual broadening of energy distribution. Notice that steady state that arrests the diffusion associated with classical chaos is a result of the interplay between the non-KAM chaos within the well region and KAM-like region above the barriers.

4.5.1 The Lattice of Double Square Wells

When $b \to 0$, $\phi = 0$ and $R = 1$, the condition in Eq. (2.14) is satisfied and hence, for $\epsilon << 1$, the phase space is filled with invariant curves. This is what would be obtained for a kicked rotor with an identical value of kick strength. Hence, to obtain mixed phase space we set $\phi \neq 0$ in which case the system becomes spatially asymmetric. While this gives the required mixed phase space layer for $\phi \neq 0$, one disadvantage is that the spatial symmetry is already broken. Hence the effect of spatial asymmetry on ratchet current cannot be studied.

To overcome this problem, we modify the system given by the Hamiltonian in Eq. (4.1). In order to study the effect of spatial symmetry for $b \to 0$, we use the stationary potential schematically shown in Fig. 4.10. The periodic unit of this stationary potential V_{sq} contains two potential wells of unequal width with its overall length, in scaled coordinate system, being equal to 4π, *i.e.*, equal to two wavelengths of the kicking field. This ensures that the periodicity of V_{sq} is commensurate with that of kicking field so that the overall spatial periodicity is maintained. The overall spatial period of the system in scaled coordinates with this new stationary potential

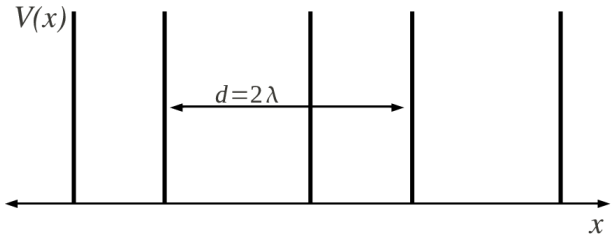

Figure 4.10: Schematic of lattice of double square wells. Barrier width b is taken to be negligible. Two consecutive finite square wells define one periodic unit. The length d of a periodic unit of this new stationary potential is twice the wavelength λ of kicking field.

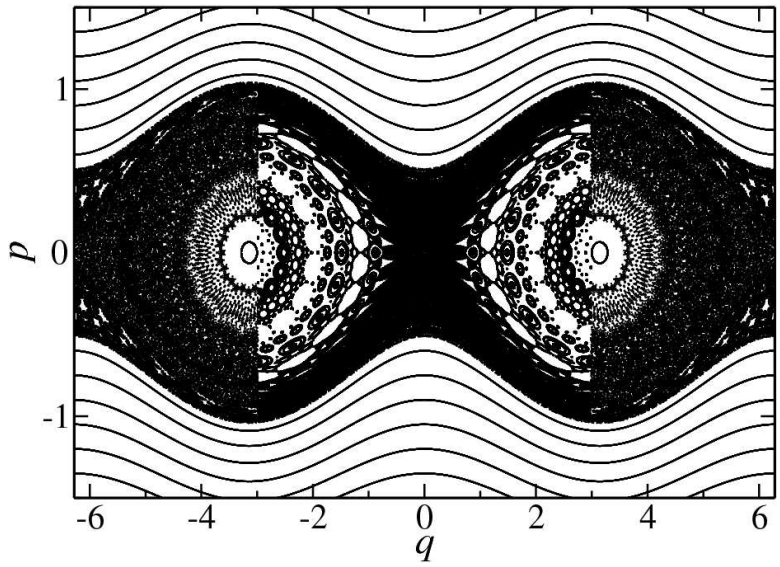

Figure 4.11: Stroboscopic section $S(0.0)$, for $b = 10^{-5}, \epsilon = 0.15, \phi = 0$ and $V_0 = 0.5$. The corresponding stationary potential is shown in Fig. 4.10.

will be 4π. The unequal width of two wells will ensure that for $\phi = 0$, Eq. (2.14) is not satisfied for the wells and the system can have mixed phase even for $\phi = 0$. The stroboscopic section $S(0.0)$ for this new stationary potential is shown in Fig. 4.11.

4.5.2 The Effect of Spatio Temporal Symmetries

The spatial symmetry of the system can be controlled through ϕ. The temporal symmetry of the system can be controlled through control over the sequence and magnitudes of kicks. For the series of delta kicks shown in Fig. 4.2, the system will

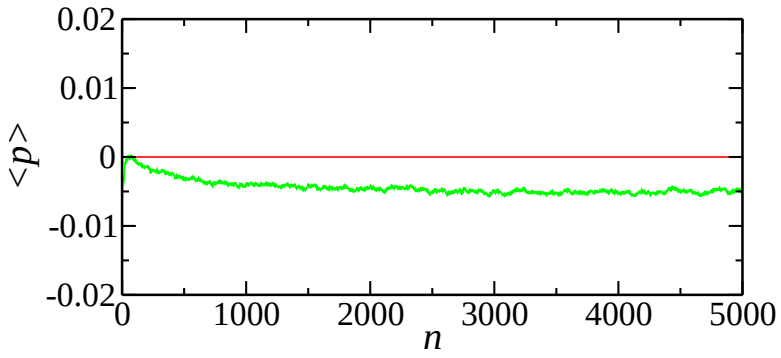

Figure 4.12: $\langle p \rangle$ vs n for ensemble of initial states all lying in chaotic layer for spatially symmetric (red) and spatially asymmetric (green) system. Temporal symmetry is maintained in both the cases. $\langle p \rangle$ is calculated on $S(0.5)$, ie. corresponding to $\tau = 0.5$. Parameters are $b = 10^{-5}, V_0 = 0.5, \epsilon = 0.2, \phi = 0.5$.

be $T-$symmetric about $\tau = 0$. This kicking sequence corresponds to kicking term (third term) in Hamiltonian H_0. However, for series of kicks defined in Eq. (4.9) and shown schematically in Fig. 4.3, there does not exist any center of symmetry and this kind of temporal variation in kicking field can be used to break the temporal symmetry of the system. Figure 4.12 shows $\langle p \rangle$ calculated on $S(0.5)$ as a function of discrete time n for the completely symmetric case as well as for the case in which spatial symmetry is broken by making $\phi \neq 0$ but temporal symmetry is maintained. It shows that the mean current of the system is zero when none of the symmetries is broken, whereas it settles to a constant non-zero value when spatial symmetry of the system is broken.

The saturation of mean current shown in Fig. 4.12 is due to existence of steady state demonstrated in section (4.4). Once the chaotic states sufficiently diffuse in the bounded chaotic layer, their net momentum attains a nearly constant value, except that there are fluctuations due to continuously changing phase space distribution around small islands embedded in the chaotic sea. In such a situations, the initial change in $\langle p \rangle$ can be treated as a transient and net transport in system is determined saturated value of the current. However, in presence of $T-$symmetry, phase space can be decomposed into pairs of stroboscopic sections in which the saturated current carried by diffusive layers in each of the sections are equal and opposite, as

shown in Fig. 4.13. It also shows that these pairs of section correspond to equal and opposite values of τ. The existence of such pairs imply that the net ratchet current averaged over τ (equivalent to average over all the stroboscopic sections) will always be zero. This result is consistent with the theoretical expectation revealed by S. Flach *i.e.* [Fl00], according to which, in the presence of temporal symmetry, the net current of a bound chaotic layer should be zero. Their work shows that if system has a center of symmetry in $t-$space, then corresponding to every trajectory (x, p, t), there exist another trajectory $(x, -p, 2t_0 - t)$, t_0 being the center of symmetry. In the case of time periodic system that we are dealing with, the center of symmetry, if it exists, lies at $\tau = 0$. Also we are dealing with trajectories in discrete time n at different sections corresponding to different values of τ. In this framework, the above theoretical result derived in [Fl00] implies that corresponding to every trajectory (q_n, p_n, τ) there must exist another trajectory $(q_n, -p_n, -\tau)$. Notice that the mean $\langle p \rangle$ for these two trajectories will be equal and opposite as they pass through equal and opposite momenta. This means that corresponding to every trajectory A on section $S(\tau)$, there exists a trajectory B on section $S(-\tau)$, such that currents carried by them are equal and opposite. This explains the distribution of current over τ values for time symmetric case as seen in Fig. 4.13.

When both spatial and temporal symmetries are broken, phase space can not be decomposed into such pairs as shown in Fig. 4.14. To break the temporal symmetry we use kicking cycle defined in Eq. (4.9). Now the net current averaged over τ will be non-zero. Figure 4.15 shows saturated values $\langle p \rangle$ for larger number of τ values for both T-symmetric and T-asymmetric case. To cancel the fluctuations in $\langle p \rangle$ values, seen in Figs. 4.13 and 4.14, we average over time after the steady state has reached.

Note that the saturated value of $\langle p \rangle$ is determined by steady state distribution of states in chaotic layer, which is independent of the details of initial set of states. Hence, the saturated current value will be independent of initial conditions. This is shown in Fig. 4.17a. One class models for chaotic (quantum) ratchet rely on chaotic

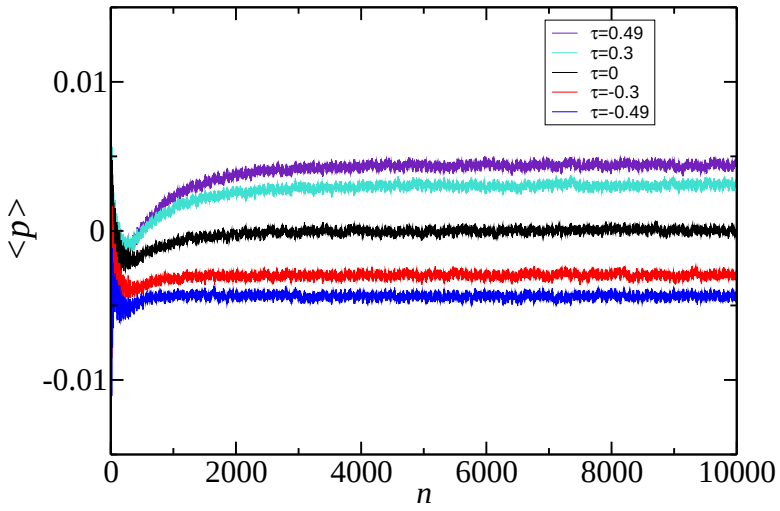

Figure 4.13: $\langle p \rangle$ vs n for ensemble of initial states all lying in chaotic layer for spatially asymmetric but T-symmetric case corresponding to different values of τ. Saturated values of $\langle p \rangle$ are equal and opposite for equal and opposite values of τ. Parameters are $b = 10^{-5}, V_0 = 0.5, \epsilon = 0.15, \phi = 0.5$.

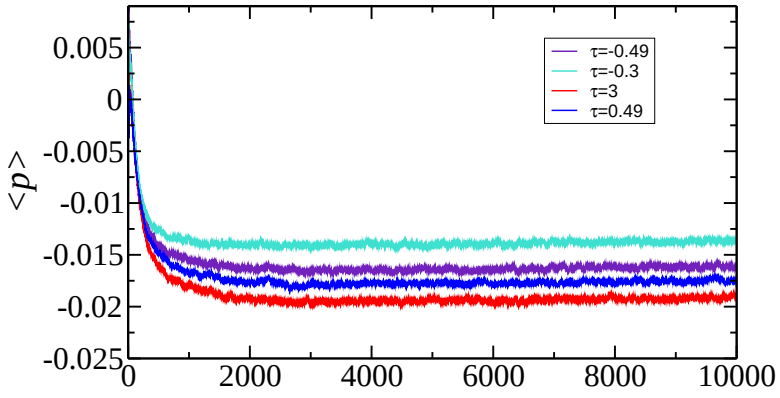

Figure 4.14: $\langle p \rangle$ vs n for ensemble of initial states all lying in chaotic layer for broken spatial and temporal symmetry corresponding to different values of τ. Saturated values of $\langle p \rangle$ are not equal and opposite for equal and opposite values of τ. Parameters are $b = 10^{-5}, V_0 = 0.5, \epsilon_1 = 0.08, \epsilon_2 = 0.16, \phi = 0.5$.

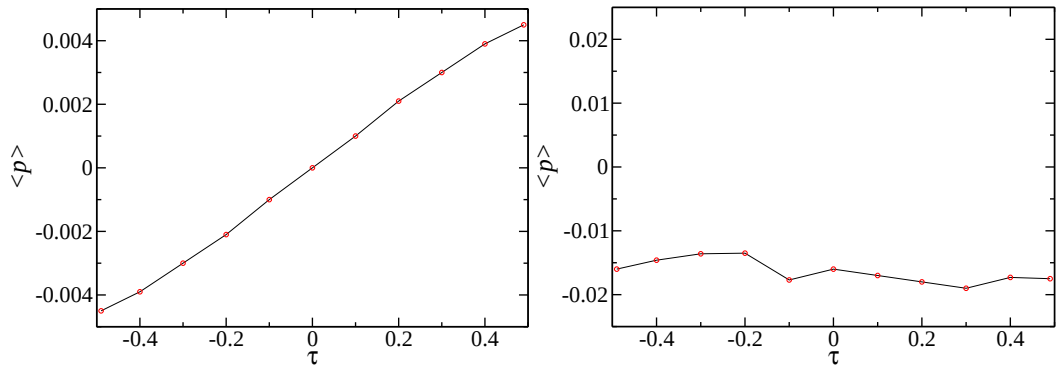

Figure 4.15: $\langle p \rangle$ vs τ for time-symmetric (left) and time-asymmetric (right) case. Spatial symmetry is broken in both the cases. Clearly, for time-symmetric case $\langle p \rangle$ values are symmetrically distributed about zero leading to net current zero. This symmetry in $\langle p \rangle$ distribution along τ does not hold when temporal symmetry is broken. Parameters for the two cases are same as those for Figs. 4.13 and 4.14, respectively.

regime in order to generate current independent of initial states [Mo00, Hu05] with limited experimental realization [Jo07a]. However, full chaos is also associated with unbounded spread in energy which is not in favor of an efficient ratchet effect. Hence the proposals in Refs. [Mo00], provide for a quantum ratchet but *not* a classical ratchet. In our model, there is a bounded mixed phase space, extent of which is very well controlled, such that the islands in it do not contribute to transport, leading to net current independent of initial state. Thus, we present a ratchet model in which one can obtain a ratchet current Independent of initial state at the same time energy spread is well controlled. Thus, in our system, meaningful classical ratchet currents can be obtained.

4.5.3 Effect of barrier width

In this section, we will discuss the behavior of $\langle p \rangle$ as a function of b for $b >> 0$. We have seen that for $b \to 0$, the $\langle p \rangle$ saturates to a constant value when steady state is reached. As discussed in section 4.4, the steady state exists because the mixed phase space is trapped between two regular regions. However, for $b >> 0$, mixed phase dynamics prevails throughout the phase space as shown in Fig. 4.4. In such a situation, any set of initial state lying in chaotic layer will keep spreading

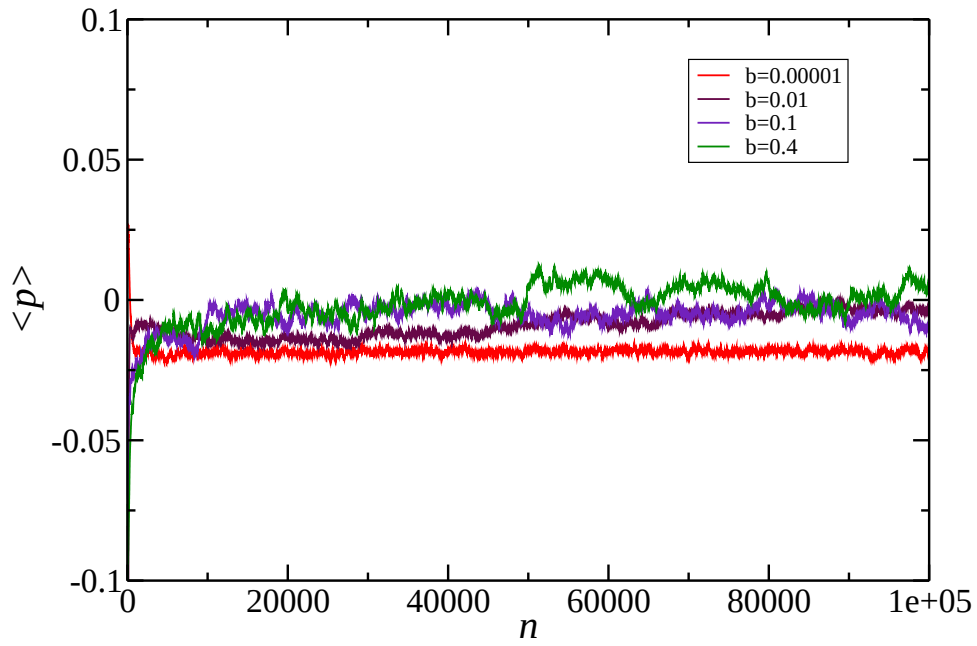

Figure 4.16: $\langle p \rangle$ vs n at $\tau = 0.5$ for different values of b. Other parameters are $V_0 = 0.5, \epsilon = 0.15, \phi = 0.5$.

in phase space. As the phase space distribution of of an ensemble of states evolve, the associated current, *i.e.*, $\langle p \rangle$ will keep changing and will never converge to any particular value. This is shown in Fig. 4.16. It shows that as b increases, the fluctuations in $\langle p \rangle$ increase. This also leads to large fluctuations in the net ratchet current averaged over τ.

Another consequence of taking $b >> 0$ is the dependence upon initial states. Clearly, in the presence of mixed phase space dynamics the evolution of a state is highly dependent on the region of phase space it is evolving in. As a result, $\langle p \rangle$ at given value of n will depend upon the initial state. Figure 4.17 shows $\langle p \rangle$ for two different sets of initial states. One set is of uniformly distributed points in a square of area 0.01 and its center coincides with the phase point (0,0). The other set of initial states is obtained by shifting the first set along q-axis by 0.1 units. As $b \to 0$, the saturated $\langle p \rangle$ is almost indistinguishable for two different set of initial states, both lying completely in chaotic layer. However, in case of $b >> 0$, $\langle p \rangle$ at any given τ is different for two different initial states. This implies that as b increases, the current becomes more and more dependent upon initial states.

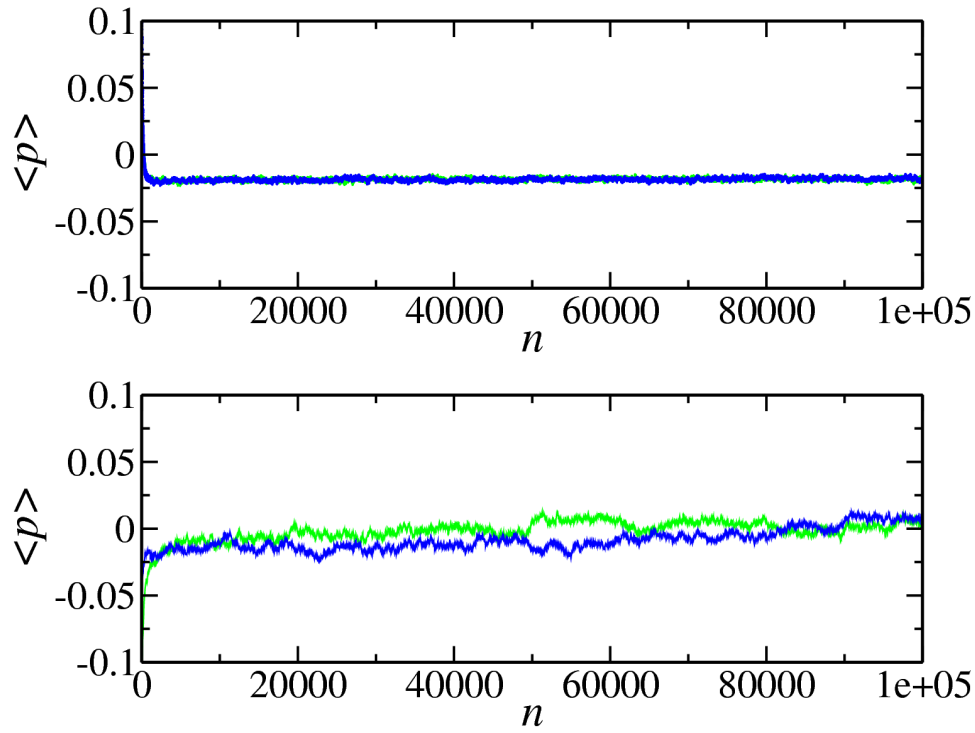

Figure 4.17: $\langle p \rangle$ vs n at $\tau = 0.5$ for two different sets initial states (discussed in text) in two different colors. The graph at the top corresponds to $b = 10^{-5}$ and the one at bottom corresponds to $b = 0.4$. Other parameters are $V_0 = 0.5, \epsilon = 0.15, \phi = 0.5$. The value of $\langle p \rangle$ at a given n is independent of the set of initial states used for $b = 10^{-5}$, but is different for different sets of initial states for $b = 0.4$.

CHAPTER 5

Kicked Particle in a Lattice of Finite Wells: The Quantum Ratchet

In this chapter we analyze the quantum dynamics of kicked particle in a lattice of finite wells. We first solve the Schroedinger equation for unperturbed system, *i.e.,* free particle in the presence of stationary potential without kicks. Then, we incorporate the effect of kicking. In order to see the signatures of classical phase space features, we generally remain confined to small value of Planck's constant so that there is sufficiently large number of energy levels in concerned energy region which roughly extend from ground state to energy twice as high as the well depth or, other words, twice as high as height of the barriers between which these well are constructed.

5.1 The Unperturbed System

In this section, we begin with the solution for the unperturbed system, *i.e.,* for $\epsilon = 0$. The Schroedinger equation for the system is described by the Hamiltonian in Eq.

(4.3) as

$$i\hbar_s \frac{\partial \psi}{\partial t}(x) = \left[\frac{-\hbar_s^2}{2} \frac{\partial^2}{\partial x^2} + V_{sq}(x) + \epsilon \cos(x+\phi) \sum_n \delta(t-n) \right] \psi(x). \tag{5.1}$$

In this, ϕ appears in the kicking field term. Also, the potential $V_{sq}(x)$ we use in this chapter is given by Eq. (4.4). In Eq. (4.4), ϕ is set to be zero. This is equivalent to shifting the origin of x-axis in such a way that the barriers are always symmetrically placed about the origin and the spatial asymmetry is introduced by shifting center of symmetry of kicking field with respect to origin. Quantum systems are convenient to analyze if V_{sq} does not shift on changing ϕ, so that the wave functions remain unaffected. The Schroedinger equation (5.1) is similar to the one given in Eq. (2.15) for a kicked particle in double barrier structure. The main difference between the two being that in the present case the stationary potential $V_{sq}(x)$ represents a series of identical finite square wells (See Fig. 4.1). Thus, $V_{sq}(x)$ is a periodic function of x. In this form, the potential is similar to the Kronig-Penney potential widely discussed in condensed matter physics [Ki03] and is a relevant basic model that explains conduction and insulation properties of solids. To study the classical evolution, it was convenient to split the Hamiltonian as sum of two parts; one, in which kicks changed the momentum and kinetic energy and the other being the effect of stationary potential $V_{sq}(x)$. However, to study the quantum dynamics, we rewrite the corresponding Hamiltonian (obtained after applying the above described shift of x-origin in Eq. (4.3)) as,

$$H = H_0 + \epsilon \cos(x+\phi) \sum_n \delta(t-n). \tag{5.2}$$

Here, $H_0 = \frac{p^2}{2} + V_{sq}(x)$ is the autonomous unperturbed system. The Schroedinger equation corresponding to H_0 is

$$i\hbar_s \frac{\partial \psi}{\partial t} = \left[\frac{-\hbar_s^2}{2} \frac{\partial^2}{\partial x^2} + V_{sq}(x) \right] \psi. \tag{5.3}$$

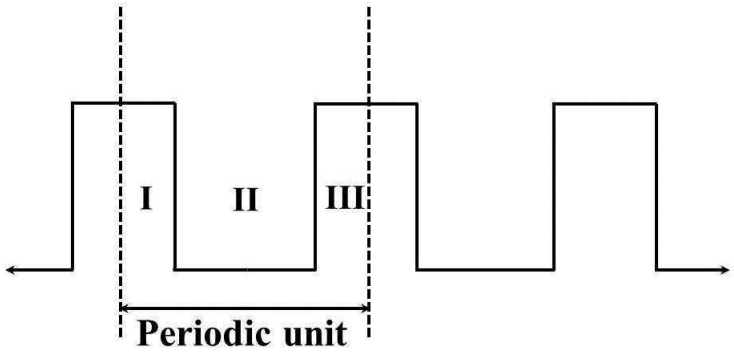

Figure 5.1: Figure shows the three regions (I, II and III) of periodic unit of $V_{sq}(x)$.

Since the potential is spatially periodic with period d, we have $V_{sq}(x) = V_{sq}(x+d)$. This periodicity implies that the Bloch theorem [As76] would apply. This theorem tells us that the wavefunction in periodic potentials can be chosen to be periodic with the same periodicity as that of the potential and modulated by a phase factor. For convenience, we have coincided the center of the potential well with the origin of coordinate axis. Now one periodic unit of stationary potential can be divided into three regions as shown in Fig. 5.1. The general solution of Schroedinger equation (5.3) in these three regions is

$$\psi(x) = R_1 e^{ik_1 x} + L_1 e^{-ik_1 x}, \qquad \frac{-d}{2} \leq x \leq \frac{-w}{2}, \tag{5.4a}$$

$$= R_2 e^{ik_2 x} + L_2 e^{-ik_2 x}, \qquad \frac{-w}{2} \leq x \leq \frac{w}{2}, \tag{5.4b}$$

$$= R_3 e^{ik_1 x} + L_3 e^{-ik_1 x}, \qquad \frac{w}{2} \leq x \leq \frac{d}{2}. \tag{5.4c}$$

To get the particular solutions, we will determine the sets of $R_1, L_1, R_2, L_2, R_3, L_3, k_1$ and k_2 for which $\psi(x)$ satisfies the applicable boundary conditions. Here, k_1 and k_2 are the wave numbers of eigenfunction in the barrier and well region, respectively. In the scaled coordinate system, since the mass of the particle becomes unity and the Planck's constant is

replaced with scaled Planck's constant $\hbar_s$, we have

$$k_1 = \frac{\sqrt{2(E-V_0)}}{\hbar_s} \qquad \frac{w}{2} < |x| \leq \frac{d}{2}; \;\; E > V_0, \tag{5.5a}$$

$$= \frac{\sqrt{2(V_0-E)}}{i\hbar_s} \qquad \frac{w}{2} < |x| \leq \frac{d}{2}; \;\; E \leq V_0, \tag{5.5b}$$

$$k_2 = \frac{\sqrt{2E}}{\hbar_s} \qquad |x| < \frac{w}{2} \tag{5.6}$$

Now, we proceed to determine the eigenenergies, and hence the wavenumbers k_1 and k_2, and the eigenfunction $\psi(x)$. We consider N units of finite well potential with periodic boundary condition applied, *i.e.*, arranged on a ring lattice. Using the Bloch theorem, we can write the wavefunction as

$$\psi(x) = \psi(x+d)e^{iKd}, \qquad K = \frac{2s\pi}{Nd} \quad (s = 0, \pm 1, \pm 2, \dots). \tag{5.7}$$

In this, the product Kd is the propagation constant. This form for the wave function implies that it can change by a phase factor e^{iKd} for spatial positions separated by distance d, *i.e.*, one period of the stationary potential. The allowed values of K are restricted by the relation $e^{iKd} = e^{i(K+2\pi)d}$. Thus the phase factor, and hence the wave function itself, repeats after N units of the stationary finite well potential.

For an arbitrary position x lying within the barrier region, we get,

$$R_1 e^{ik_1 x} + L_1 e^{-ik_1 x} = e^{iKd}\left(R_3 e^{ik_1 x} + L_3 e^{-ik_1 x}\right). \tag{5.8}$$

This leads to

$$R_3 = R_1 e^{id(K-k_1)}, \tag{5.9}$$

$$L_3 = L_1 e^{id(K-k_1)}. \tag{5.10}$$

Substituting this in the general solution in Eq. (5.4), we obtain

$$\begin{aligned}
\psi(x) &= R_1 e^{ik_1 x} + L_1 e^{-ik_1 x}, & \frac{-d}{2} \leq x \leq \frac{-w}{2}, \quad (5.11a)\\
&= R_2 e^{ik_2 x} + L_2 e^{-ik_2 x}, & \frac{-w}{2} \leq x \leq \frac{w}{2}, \quad (5.11b)\\
&= R_1 e^{id(K-k_1)} e^{ik_1 x} + L_1 e^{id(K-k_1)} e^{-ik_1 x}, & \frac{w}{2} \leq x \leq \frac{d}{2}. \quad (5.11c)
\end{aligned}$$

Now we apply the continuity conditions

$$\begin{aligned}
\psi\left(x_+\right) &= \psi\left(x_-\right), & (5.12a)\\
\psi'\left(x_+\right) &= \psi'\left(x_-\right). & (5.12b)
\end{aligned}$$

Here ψ' represents the position derivative of ψ, x_+ and x_- are two points arbitrarily close to x on its right and left hand side, respectively. Using Eq. (5.12) for $x = \frac{w}{2}$ and $x = \frac{-w}{2}$ leads to a set of linear equations in R_1, R_2, L_1 and L_2. Denoting the coefficient vector as

$$\mathcal{R} = \begin{bmatrix} R_2 \\ L_2 \\ R_1 \\ L_1 \end{bmatrix}, \tag{5.13}$$

the linear system to be solved becomes

$$\mathbf{M}\mathcal{R} = 0, \tag{5.14}$$

where the matrix $\mathbf{M}$ is given by,

$$\mathbf{M} = \begin{bmatrix}
e^{ik_2\frac{w}{2}} & e^{-ik_2\frac{w}{2}} & -e^{id(K-k_1)}e^{ik_1\frac{w}{2}} & -e^{id(K+k_1)}e^{-ik_1\frac{w}{2}} \\
k_2 e^{ik_2\frac{w}{2}} & -k_2 e^{-ik_2\frac{w}{2}} & -k_1 e^{id(K-k_1)}e^{ik_1\frac{w}{2}} & k_1 e^{id(K+k_1)}e^{-ik_1\frac{w}{2}} \\
e^{-ik_2\frac{w}{2}} & e^{ik_2\frac{w}{2}} & -e^{-ik_1\frac{w}{2}} & -e^{ik_1\frac{w}{2}} \\
k_2 e^{-ik_2\frac{w}{2}} & -k_2 e^{ik_2\frac{w}{2}} & -k_1 e^{-ik_1\frac{w}{2}} & k_1 e^{ik_1\frac{w}{2}}
\end{bmatrix}. \tag{5.15}$$

The homogeneous system of linear equations (5.14) will have non-trivial solution only if

$$\det(\mathbf{M}) = 0. \tag{5.16}$$

The condition in Eq. (5.16) leads to dispersion relations:
For $E > V_0$,

$$\cos\left(k_2\frac{w}{2}\right)\cos\left(k_1[d-w]\right) - \frac{{k_1}^2 + {k_2}^2}{2k_1k_2}\sin\left(k_2\frac{w}{2}\right)\sin\left(k_1\left[d-w\right]\right) = \cos\left(Kd\right). \tag{5.17}$$

For $E < V_0$,

$$\cos\left(k_2\frac{w}{2}\right)\cosh\left(\widetilde{k}_1[d-w]\right) - \frac{{k_2}^2 - \bar{k_1}^2}{2\widetilde{k}_1k_2}\sin\left(k_2\frac{w}{2}\right)\sinh\left(\widetilde{k}_1\left[d-w\right]\right) = \cos\left(Kd\right), \tag{5.18}$$

where $\widetilde{k}_1 = ik_1 = \dfrac{\sqrt{2(V_0 - E)}}{\hbar_s}$.

The dispersion relations obtained above are transcendental equations in the unknown variables k_1 and k_2. Hence, we obtain numerical solutions to find (k_1, k_2) pairs that satisfy either Eq. (5.17) or (5.18) for allowed values of propagation constant K. The triplets (K, k_1, k_2) which solve Eq. (5.17) or (5.18) are substituted back in (5.14). This linear system is then solved to obtain the vector $\mathcal{R}$, *i.e.,* the constants R_1, L_1, R_2 and L_2. This is substituted in (5.11) along with the triplet (K, k_1, k_2) to obtain the eigenstates of the unperturbed system represented by the Hamiltonian H_0 in Eq. (5.2). For any particular state, its energy can be calculated as

$$E = \frac{{k_2}^2\hbar^2}{2}. \tag{5.19}$$

Notice that the Eqs. (5.11) and (5.14) are periodic in Kd. Hence, it is sufficient to consider only one period of Kd, say, from $-\pi$ to π which corresponds to $\frac{-N}{2} \leq s \leq \frac{N}{2}$ in Eq. (5.7). This range is referred to as the first Brillouin zone [As76]. Figure 5.2 shows energy levels calculated for two typical situations. Graph on the right corresponds to a situation in which energy levels are distributed among broad, well separated, bands. These are the conduction bands. Within each

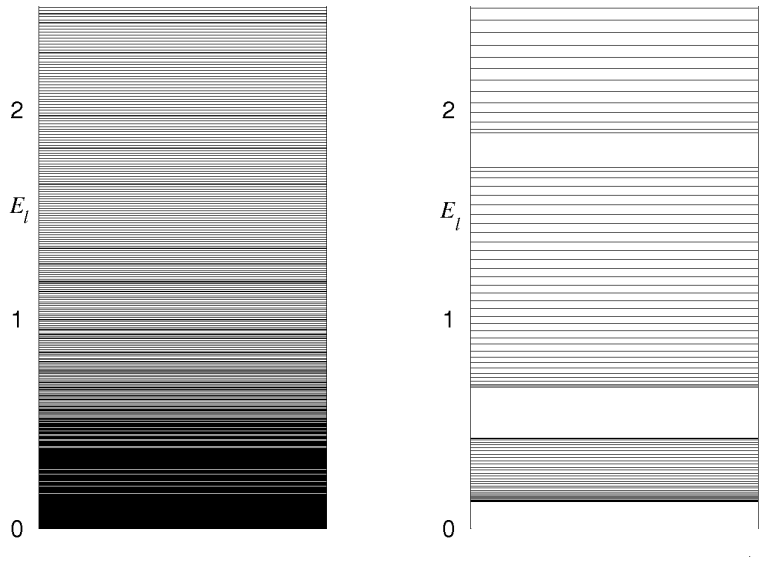

Figure 5.2: (Left) Energy levels of eigen states of unperturbed system, calculated for $b = 0.1\pi$, $V_0 = 0.5$, $\hbar_s = 0.0067$ and $N = 1$. It shows that energy levels are densely distributed for $\hbar_s << 1$. (Right) Energy levels of eigen states of unperturbed system, calculated for $b = 0.6\pi$, $V_0 = 0.5$, $\hbar_s = 1.1$ and $N = 64$. For large values of $\hbar_s$, the energies of basis states are distributed in broad well separated bands.

band there are densely distributed N discrete levels. This scenario exists for large values $\hbar_s$ and N. As $\hbar_s \to 0$, the behavior of the system goes closer to that of the corresponding classical system. In this situation, the energy bands come close to each other and shrink in energy space. The levels within a given band become practically indistinguishable. The left graph shows energy levels for a very small value of $\hbar_s$. Since the energy levels within a band become practically indistinguishable in such a situation, we consider only $N = 1$ to save computation time. For $\hbar_s << 1$, for which we get dense energy levels as shown in left graph in Fig. 5.2, the system is in the semiclassical regime. For most part, we remain confined to this regime in this thesis

5.2 The Kicked System

In this section, we solve the full system in Eq. (5.2) after incorporating the effect of kicks in the unperturbed system H_0. As done in case of DBS, we use the

time-periodic nature of the kicking and write down one period Floquet operator. We use the eigenstates of unperturbed system as basis states to get the matrix form of Floquet operator and calculate its eigen vectors, known as Floquet states, in the chosen basis. These eigenvectors in Husimi representation collectively contain the information on the dynamics at discrete time steps in a way analogous to the stroboscopic section in classical phase space (q, p, τ). The results in chapter 4 show that the ratchet current depends upon the phase τ of the kicking period and we have to consider the complete three dimensional picture (q, p, τ). To get a complete quantum mechanical picture, we calculate F for different values of τ. Any periodic cycle of kicks can be divided into alternating regimes of free evolutions and kicks as discussed in section (4.3). In this chapter we use two types of kicking cycles comprising (i) one kick followed by evolution under the action of $\widehat{H}_0$ (see Fig. 4.2) (ii) two kicks of unequal strength and two unequal periods of evolution under the action of $\widehat{H}_0$ (see Fig. 4.3). The time evolution operator corresponding these types of kicking cycle can be written in following form;

(i) One-kick cycle

$$\widehat{F}(\tau) = \widehat{f}_1^a(\tau)\widehat{k}_1(\tau)\widehat{f}_1^b(\tau), \tag{5.20}$$

(ii) Two-kick cycle

$$\widehat{F}(\tau) = \widehat{f}_2^a(\tau)\widehat{k}_2(\tau)\widehat{f}_1^a(\tau)\widehat{k}_1(\tau)\widehat{f}(\tau). \tag{5.21}$$

Here, $f_i^a(\tau), f_i^b(\tau)$ represent the evolution under the effect of $\widehat{H}_0$ before and after the i-th kick respectively. The operator $\widehat{k}_i(\tau)$ incorporates the effect of i-th kick. The arrangement of free evolution and kicks within a cycle changes with τ, hence $f_i^b(\tau)$, $f_i^a(\tau)$, $k_i(\tau)$ are different for different values of τ, as discussed section (4.3) also (see Fig. 4.3). We are using index representing kick number even for one-kick case just to make the generalization to higher number of kicks per cycle easy.

Writing $F(\tau)$ explicitly as time ordered product of the operators for free evolu-

tion and kicking part for one-kick cycle, we get

$$\widehat{F}(\tau) = \exp\left(-\frac{i}{\hbar_s}\widehat{H}_1 \nabla_1^a(\tau)\right) \exp\left(-\frac{i\epsilon_1(\tau)}{\hbar_s}\cos(\widehat{x})\right) \exp\left(-\frac{i}{\hbar_s}\widehat{H}_1 \nabla_1^b(\tau)\right). \tag{5.22}$$

Here, $\epsilon_1(\tau)$ represents the strength of kick. In case of two kick cycle, we will have kick strengths $\epsilon_1(\tau)$ and $\epsilon_2(\tau)$. We use this kind of kicking cycle for breaking the temporal symmetry. Note that in the earlier works on quantum ratchets only kicking cycles composed of kicks of equal strength is considered. Isherwood [Is04] has shown that with identical kick strengths, minimum number of kicks required in a cycle, in order to get ratchet current, is three. The generalization to non-identical kick strengths in a cycle used for breaking temporal symmetry of the system and obtaining ratchet current with just two kicks is particularly useful in saving computational time. The time duration of evolution before and after the kick are being represented by $\nabla_i^b(\tau)$ and $\nabla_i^a(\tau)$, respectively. We obtain matrix form of $\widehat{F}(\tau)$ in the basis of the corresponding unperturbed system. In the chosen basis, the matrix elements can be written as

$$F_{mn}(\tau) = \langle m|\widehat{F}(\tau)|n\rangle, \tag{5.23}$$

where, $|m\rangle$ stands for m-th eigenstate of $\widehat{H}_0$. Substituting in Eq. (5.22), we get

$$\begin{aligned} &F_{mn}(\tau) = \\ &\langle m| \exp\left(-\tfrac{i}{\hbar_s}\widehat{H}_1 \nabla_1^a(\tau)\right) \exp\left(-\tfrac{i\epsilon_1(\tau)}{\hbar_s}\cos(\widehat{x})\right) \exp\left(-\tfrac{i}{\hbar_s}\widehat{H}_1 \nabla_1^b(\tau)\right) |n\rangle. \end{aligned} \tag{5.24}$$

Since $|m\rangle$ and $|n\rangle$ are eigenstates of $\widehat{H}_0$, we have

$$\langle m| \exp\left(-\frac{i}{\hbar_s}\widehat{H}_1 \nabla_1^a(\tau)\right) = \exp\left(-\frac{i}{\hbar_s}E_m \nabla_1^a(\tau)\right) \langle m|, \tag{5.25a}$$

$$|n\rangle \exp\left(-\frac{i}{\hbar_s}\widehat{H}_1 \nabla_1^a(\tau)\right) = \exp\left(-\frac{i}{\hbar_s}E_n \nabla_1^a(\tau)\right) |n\rangle, \tag{5.25b}$$

where E_m and E_n are eigenenergies of $\widehat{H}_0$ corresponding to states $|m\rangle$ and $|n\rangle$,

respectively. Substituting back in Eq. (5.24), we get

$$\begin{aligned} F_{mn}(\tau) &= \exp\left(-\frac{i}{\hbar_s}E_m\nabla_1^a(\tau)\right)\exp\left(-\frac{i}{\hbar_s}E_n\nabla_1^b(\tau)\right) \\ &\quad \langle m \mid \exp\left(-\frac{i\epsilon_1(\tau)}{\hbar_s}\cos(\widehat{x})\right) \mid n\rangle \end{aligned} \tag{5.26}$$

The last term on the R.H.S. of Eq. (5.26) can be evaluated in the position representation as

$$\langle m|\exp\left(-\frac{i\epsilon_1(\tau)}{\hbar_s}\cos(\widehat{x})\right)|n\rangle = \int_{\frac{-Nd}{2}}^{\frac{Nd}{2}}\psi_m^*(x)\psi_n(x)\exp\left(-\frac{i\epsilon_1(\tau)}{\hbar_s}\cos(x)\right)\,dx. \tag{5.27}$$

Using this, we finally get the matrix elements of Floquet operator for one-kick cycle as

$$\begin{aligned} F_{mn}(\tau) &= \exp\left(-\tfrac{i}{\hbar_s}E_m\nabla_1^a(\tau)\right)\exp\left(-\tfrac{i}{\hbar_s}E_n\nabla_1^b(\tau)\right) \\ &\times \int_{\frac{-Nd}{2}}^{\frac{Nd}{2}}\psi_m^*(x)\psi_n(x)\exp\left(-\frac{i\epsilon_1(\tau)}{\hbar_s}\cos(x)\right)\,dx. \end{aligned} \tag{5.28}$$

Now for the case of two-kick cycle, the evolution during every cycle can be split into two parts; (i) before the second kick $F_1(\tau)$, (ii) after the second kick. The Floquet operator in Eq. (5.21) can now be written as

$$\widehat{F}(\tau) = \widehat{F}_2(\tau)\widehat{F}_1(\tau), \tag{5.29}$$

where,

$$\widehat{F}_1(\tau) = \widehat{f}_1^a(\tau)\widehat{k}_1(\tau)\widehat{f}_1^b(\tau) \tag{5.30a}$$

$$\widehat{F}_2(\tau) = \widehat{f}_2^a(\tau)\widehat{k}_2(\tau) \tag{5.30b}$$

Now, $\widehat{F}_1(\tau)$ and $\widehat{F}_2(\tau)$ can separately be treated at par with $\widehat{F}(\tau)$ for one-kick cycle.

Using the expression derived for matrix element in Eq. (5.28), we can write

$$\begin{aligned} F_{1mn}(\tau) &= \exp\left(-\frac{i}{\hbar_s}E_m\nabla_1^a(\tau)\right)\exp\left(-\frac{i}{\hbar_s}E_n\nabla_1^b(\tau)\right) \\ &\times \int_{\frac{-Nd}{2}}^{\frac{Nd}{2}}\psi_m^*(x)\psi_n(x)\exp\left(-\frac{i\epsilon_1(\tau)}{\hbar_s}\cos(x)\right)dx, \end{aligned} \tag{5.31a}$$

$$\begin{aligned} F_{2mn}(\tau) &= \exp\left(-\frac{i}{\hbar_s}E_m\nabla_1^a(\tau)\right) \\ &\times \int_{\frac{-Nd}{2}}^{\frac{Nd}{2}}\psi_m^*(x)\psi_n(x)\exp\left(-\frac{i\epsilon_1(\tau)}{\hbar_s}\cos(x)\right)dx. \end{aligned} \tag{5.31b}$$

Notice that Eq. (1.31b) contains only one term for evolution under the action of $\widehat{H}_0$, because the evolution before the second kick has already been accounted in F_1. The matrix representing $\widehat{F}(\tau)$ for two-kick cycle will be a product of matrices for $\widehat{F}_1$ and $\widehat{F}_2$, and hence its matrix element will be

$$F_{mn}(\tau) = \sum_l F_{2ml}(\tau)F_{1lm}(\tau). \tag{5.32}$$

The eigenvalues and eigenvectors of the Floquet matrices are numerically computed using LAPACK and BLAS routines [Lib] Using the computed eigenvectors of Floquet operators, the Floquet states in chosen basis can be determined as

$$|\Psi_j\rangle = \sum_l V_j^l(\tau)\,|l\rangle. \tag{5.33}$$

Here, $|\Psi_j\rangle$ is the j-th Floquet state, $V_j^l = \langle l|\Psi_j\rangle$ is the l-th element of the corresponding eigenvector of matrix $F(\tau)$ and represents the overlap of a Floquet state with the l-th unperturbed state.

In the classical system, we mostly dealt with the initial distribution of points lying in the well region with their energy being $E \leq V_0$. Equivalently, in the quantum system, we consider initial state will never have non-zero overlap with unperturbed states defined by $E > V_0$. For such a case, we need to consider only

those Floquet states which have non-zero overlap with unperturbed states with $E < V_0$. We write an initial state as a superposition of Floquet states

$$|\alpha\rangle = \sum_j c_j |\Psi_j\rangle. \tag{5.34}$$

In this $c_j = \langle\alpha|\Psi_j\rangle = \sum_l \langle\alpha|l\rangle\langle l|\Psi_j\rangle$, and defines the overlap of initial state with Floquet state $|\Psi_j\rangle$. Now, if $|\alpha\rangle$ is evolved using Floquet operator for n time steps, we get

$$\widehat{F}^n(\tau)\ |\alpha\rangle = \sum_j e^{in\Phi_j} c_j |\Psi_j\rangle, \tag{5.35}$$

where Φ_j are eigenphases or quasienergies of the Floquet states. The overlap of this evolved of this state with a Floquet state $|\Psi_i\rangle$ will be $\langle\alpha|\Psi_j\rangle = c_j e^{in\Phi_j}$. Note that the initial state and evolved state has same magnitude of overlap with a given Floquet state.

In the unperturbed basis, overlap of the initial state with a Floquet state will be

$$\langle\alpha|\Psi_j\rangle = \sum_l \langle\alpha|l\rangle\langle l|\Psi_j\rangle \tag{5.36}$$

Let there be l_c unperturbed states for which $E \leq V_0$. Since initial state is assumed to lie completely below, *i.e.,* $\langle\alpha|l\rangle = 0$ for $l > l_c$ (we allot indices to basis states in increasing order of their energy, so larger l implies larger energy). Using this, the overlap with Floquet state becomes $\langle\alpha|\Psi_j\rangle = \sum_{l=1}^{l_c} \langle\alpha|l\rangle\langle l|\Psi_j\rangle$. If the Floquet state Ψ_j has no overlap with basis state whose energy is $E \leq V_0$, *i.e.,* $\langle l|\Psi_j\rangle$ for $l \leq l_c$, then $\langle\alpha|\Psi_j\rangle = \sum_{l=1}^{l_c} \langle\alpha|l\rangle\langle l|\Psi_j\rangle = 0$. This implies that if initial state lies completely in energy region ($E \leq V_0$), the evolved state will be superposition of only those Floquet states which have non-zero overlap with basis states for which $E \leq V_0$. This provides a criteria to truncate the basis states for the Floquet states of our interest. We consider only those Floquet states which have at least one percent probability in region ($E \leq V_0$). All the basis states with energies in the range $0 \leq E \leq E_t$ were found to be sufficient to achieve desired convergence in the

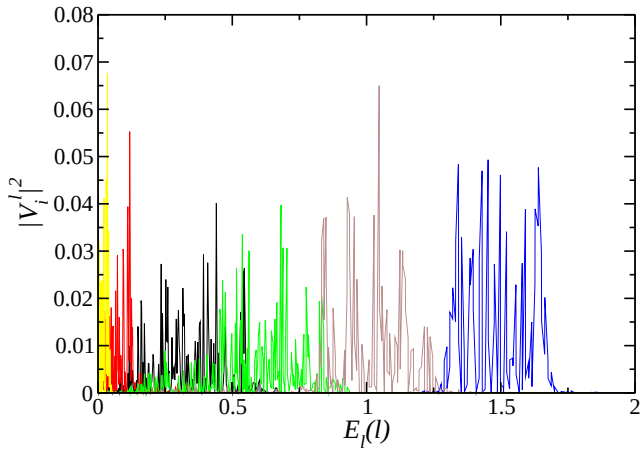

Figure 5.3: The probability density $|V_j^l|^2$ for some Floquet states vs energy of the basis states. The parameters are $\hbar_s = 0.0067, \phi = 0.5, V_0 = 0.5, \epsilon = 0.15, R = 1.9$.

Floquet states of our interest. Hence, we truncate the basis at energy $E = E_t$.

Figure 5.3 shows the overlap probability density $|V_j^l|^2$ of few Floquet states plotted against energies of the unperturbed states. For the same set of parameters classical phase space shows mixed dynamics, $i.e.$, phase space is spanned by a fully connected chaotic layer in which stable islands are embedded. However, almost all the Floquet states shown in Fig. 5.3 are localized in energy space. In Fig. 5.4, we show the spread (over the basis states) for all the Floquet states which have at least one percent probability in region $(E \leq V_0)$. The spread is shown in terms of minimum and maximum energies, denoted by E_{min} and E_{max}, at which Floquet state has finite (non-negligible) probability density. The probability density of a Floquet state $|\Psi_i\rangle$ at eigen energy E_l qualifies to be considered as finite if $|V_j^l|^2 > 0.0005$. Even though this is a arbitrary choice, nearly all such Floquet states are localized within the truncated basis, the limit of which is shown through a horizontal line. Thus, for the given choice of parameters, all the Floquet states which have significant overlap with energy region $E \leq V_0$ have converged within the truncated basis set.

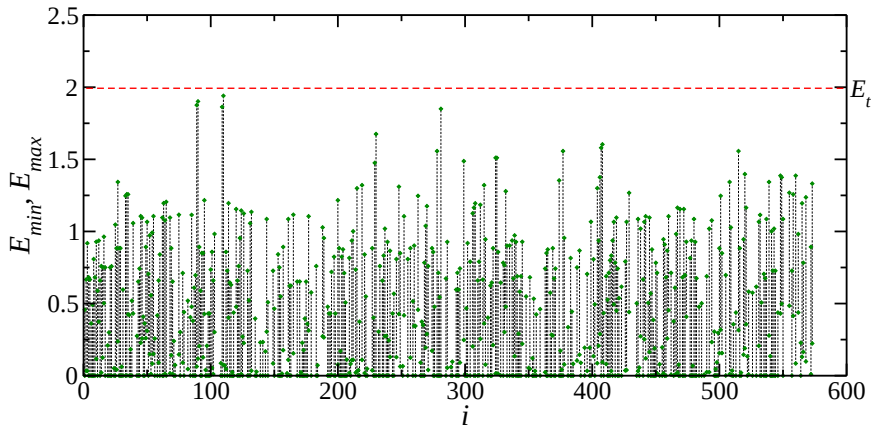

Figure 5.4: The horizontal axis shows the index (state number) assigned to Floquet states. The bottom and top points connected with a given vertical line represent the minimum energy E_{min} and maximum energy E_{max} at which the corresponding Floquet state $|\Psi_i\rangle$ has probability above the cut-off value 0.0005. Only those states which have minimum one percent probability with $E < V_0$ are shown. E_t represents the energy at which the basis is truncated.

5.3 The Quantum 'Phase Space'

In this section, we study the features of the Floquet states. In order to make correspondence with the classical phase space structures, we visualize the Floquet states $|\Psi_j\rangle$ in the Husimi representation and observe the signatures of non-KAM classical dynamics in them. Floquet states corresponding to any one particular value of τ are sufficient to grossly visualize the phase space structures, as in a single stroboscopic section from classical phase space. Throughout this section we use $\tau = 0$. The position wave function $\langle x|\Psi_j\rangle$ of a Floquet state $|\Psi_j\rangle$ can be substituted in Eq. (2.21) to get the corresponding Husimi function. Figure 5.5 shows Husimi distribution corresponding to some Floquet states to highlight some typical features of 'quantum phase space'.

The Husimi distributions shown in Figs. 5.5(a,b), for $R = 1, \epsilon = 0.15, b = 0.1\pi, V_0 = 0.5$ with $\hbar_s = 0.0067$ reveal the signature of classical chaotic dynamics around the hyperbolic fixed point $(x = \phi, p = 0)$ where $\phi = 0.5$. Figure 5.5(c-h) shows the Floquet states, in Husimi representation, which do not overlap with the strongly chaotic region around this hyperbolic fixed point. In Fig. 5.5(c) the

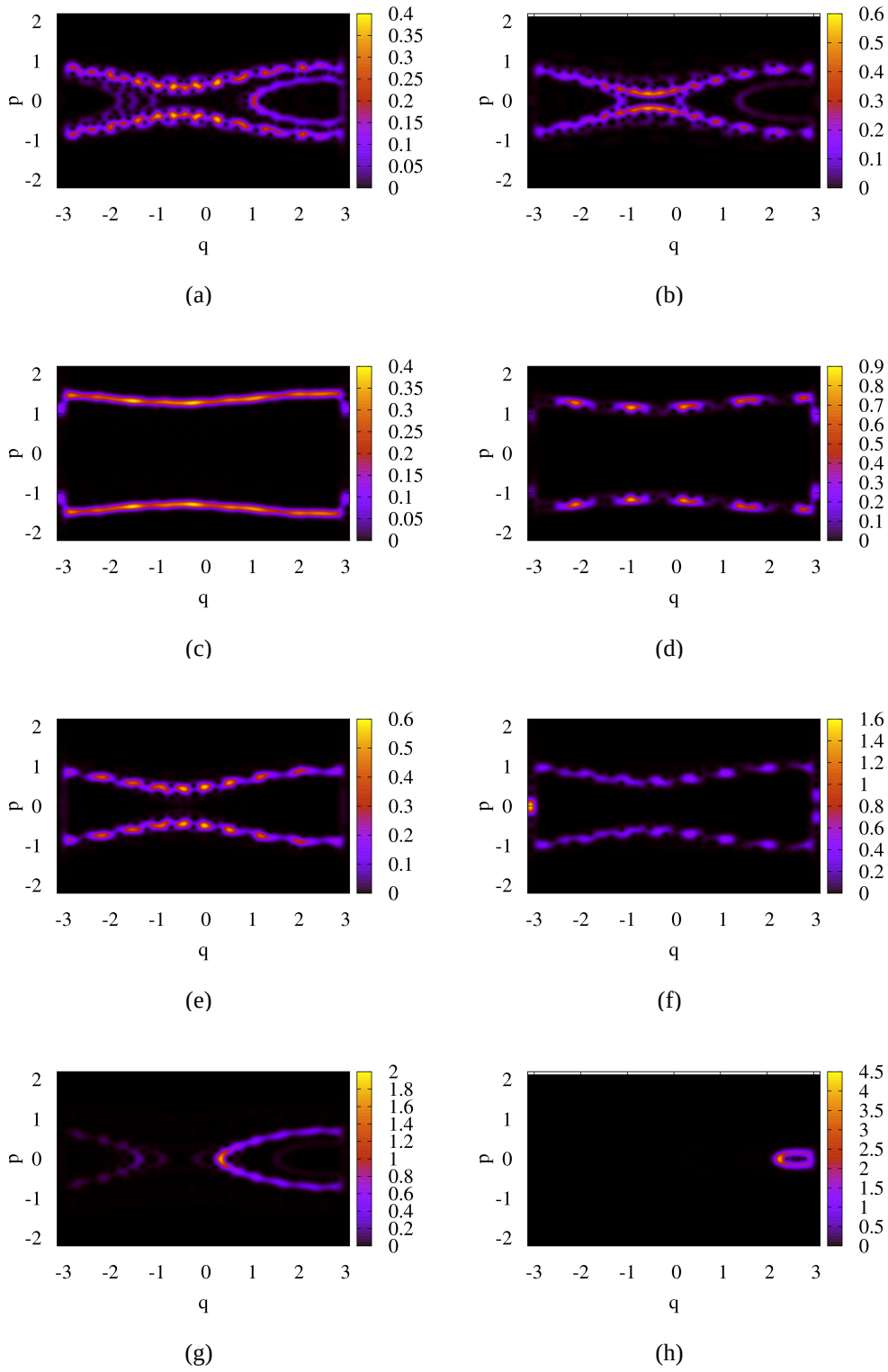

Figure 5.5: Husimi distribution for some of the Floquet states. Parameters: $\epsilon = 0.15$, $b = 0.1\pi$, $V_0 = 0.5$, $\hbar = 0.0067$ and $\phi = 0.5$

Husimi density is high for $p > 1$, which corresponds to phase space region beyond the barrier height. Hence, the structure closely resembles the invariant curves corresponding to quasi periodic orbits of the kicked rotor except that discontinuity in the barrier region is visible. This is a consequence of discontinuous classical trajectory at the discontinuities in the potential. We remind the reader that for these states barrier width $b >> 0$. For this value of b, classical phase space displays mixed dynamics. The states shown in Fig. 5.5(d-f) appear to be in proximity with the higher order resonances of the kicked rotor. The state shown in Fig. 5.5g displays enhanced density near the right barrier but much diminished density near the left barrier. The state shown in Fig. 5.5h shows almost closed orbit around elliptic fixed point at $(\pi - \phi, 0)$. In general, bulk of the Floquet states appear to have localized structures when seen in Husimi representation.

In Fig. 5.6, another panel of Floquet states is shown as Husimi plots. In this figure, the parameters are so chosen such that they differ only slightly from the parameter set used in Fig. 5.5. Increasing the values of b or ϕ, even by a small amount, will lead to more chaos in the system since we will be moving farther away from the situation in which Eq. (2.14) is satisfied. This effect of larger chaotic layer in phase space is seen in more complex Floquet states in Fig. 5.6. For the purpose of comparison, in Fig. 5.6(e,f), we show Floquet states for $\phi = 0$ and other parameters are same as in Fig. (5.5). This shows strongly localized density in the region which would be spanned by chaotic layer in classical phase space. This could be attributed to the influence of the individual orbits.

Husimi distributions in Fig. 5.7 show a selection of Floquet states for small barrier widths compared to the width of the potential, *i.e.*, $b << w$. In Fig. 5.7, we have chosen $b = 0.0001\pi$ for which $R = 0.99995$. The spatial symmetry of the system is broken by taking $\phi = 0.5$. The classical phase space for nearly the same set of parameters, $R = 1.0, \phi = 0.5$, is shown in Fig. 4.8 and it displays mixed dynamics. However, in contrast, the Husimi distributions shown in Fig. (5.7) resemble quasi periodic orbits of the kicked rotor. This is due to the fact that for very

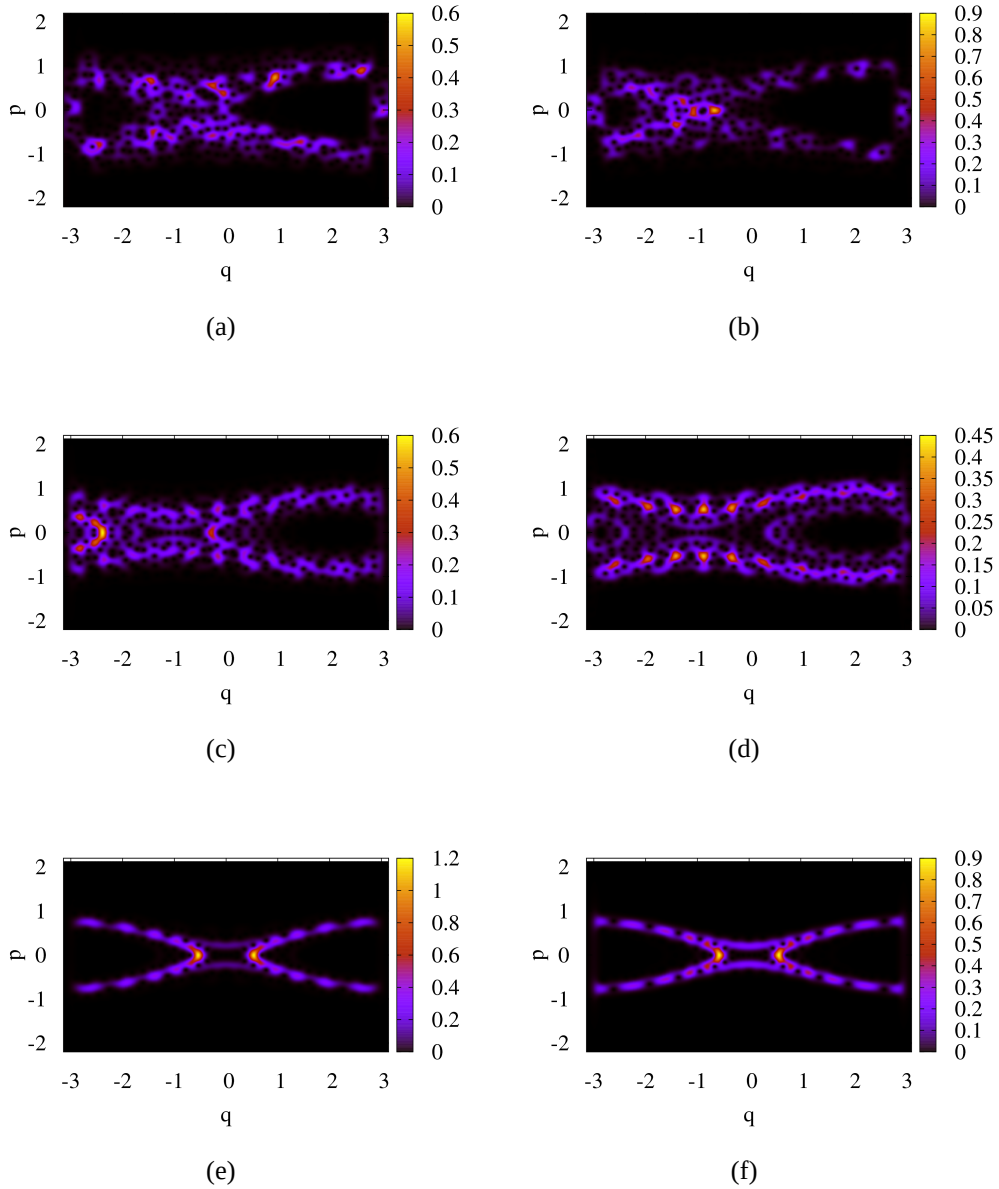

Figure 5.6: Husimi distribution for some of the Floquet states. The parameters are $\epsilon = 0.15$, $V_0 = 0.5$, $\hbar = 0.0067$, (a,b) $b = 0.3\pi, \phi = 0.5$, (c,d) $b = 0.1\pi, \phi = 1.0$, (d,e) $b = 0.1\pi, \phi = 0$

small value of barrier width b the transmission coefficient is high and the reflection from the barrier becomes small. Note that classically it is the multiple reflection at the barriers that is responsible for breaking the quasi periodic orbits and this leads to chaotic dynamics. Thus, for this choice of parameters, while classical dynamics is mixed, quantum behavior is different primarily due to tunnelling effect. In the quantum kicked rotor, localization appears as a purely quantum effect in contrast with the classical diffusive dynamics [Re04]. In this system, instead of localization due to interference effects, we see tunnelling as a quantum effect.

It has been verified that for above value of R being so close to unity, the dynamics in the well region is KAM-like until $\phi \neq 0$ (for $R \in$ integer, only $\phi \neq 0$ can violate the condition for KAM-like behavior ; see Eq. (2.14)). So non-KAM chaos for such a value of R can be fully attributed to non-zero ϕ. Figure 5.8 shows the quantum phase space for $\equiv 0.001\pi, R = 0.995$. The rest of the parameters are same as those for Fig. 5.7). The classical dynamics is KAM-like for $\phi = 0$ even for $R = 0.995$. This means that for the purpose of classical dynamics the difference in R can neglected, both can be treated as unity. However, the difference in two values of b leads to significant change in tunneling coefficients (within the WKB approximation, tunneling coefficient is 0.62 for $b = 0.0001\pi$ and 0.44 for $b = 0.001\pi$ and we have used an approximate value of energy E estimated from Fig. 5.7b and 5.7e). The Husimi distribution in Fig. 5.8 show trajectories which approximately overlap with 5.7b and 5.7e but are more dispersed in phase space. This increased spread in phase space is a manifestation of non-KAM classical dynamics which shows its signature more prominently if tunneling is better suppressed. The difference in b for above two cases does not affect the classical dynamics in a significant way but the associated change in tunneling affects the quantum dynamics significantly. Thus, this example shows how quantum effects such as tunnelling manifests itself in a system whose classical analog is essentially chaotic.

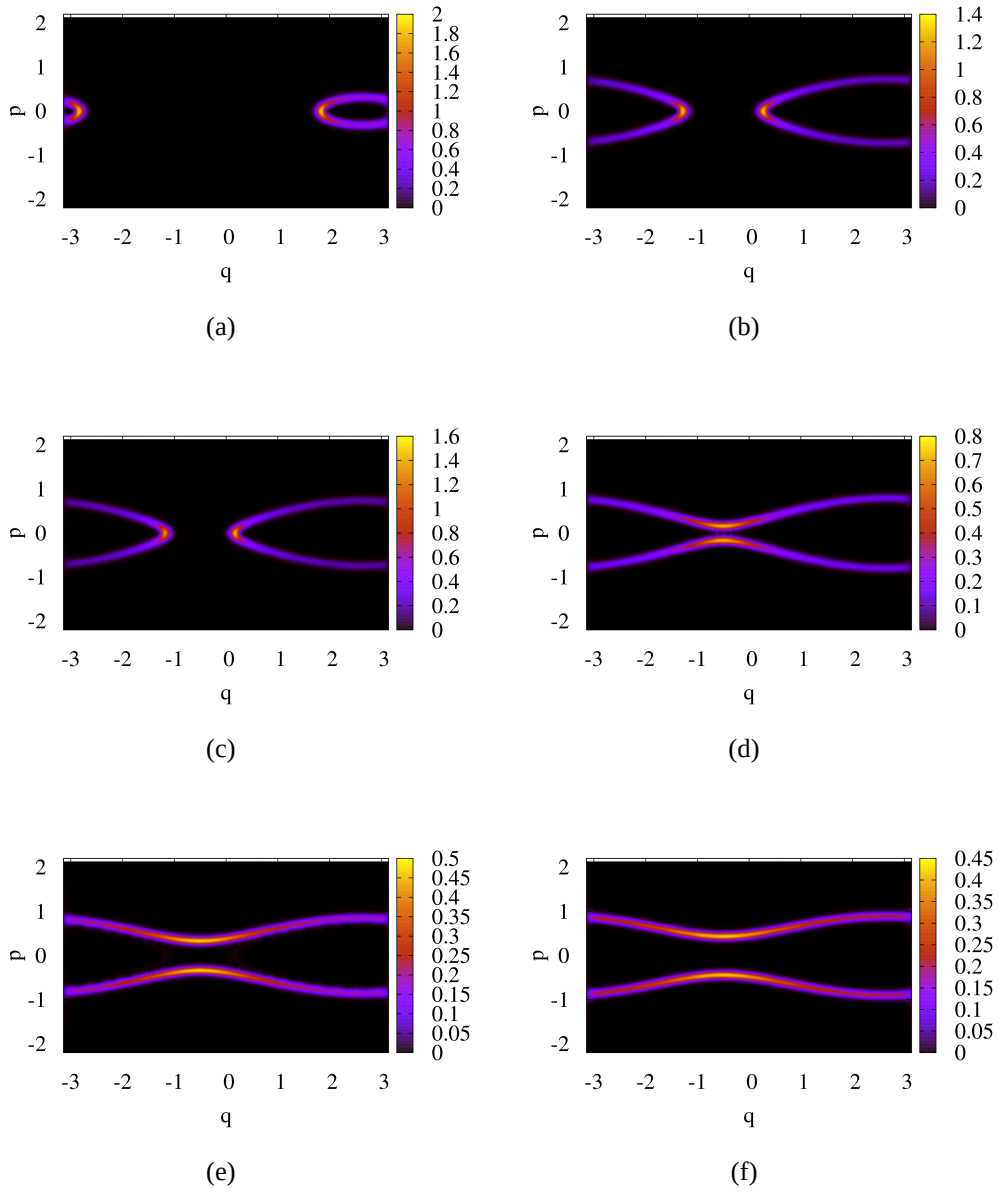

Figure 5.7: Husimi distribution for some of the Floquet states. Parameters: $\epsilon = 0.15$, $b = 0.00001\pi$, $V_0 = 0.5$, $\hbar = 0.0067$

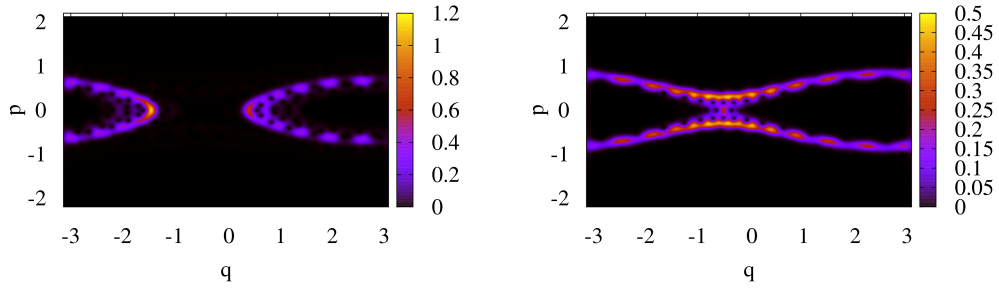

(a) (b)

Figure 5.8: Husimi distribution for some of the Floquet states. Parameters: $\epsilon = 0.15$, $b = 0.0001\pi$, $V_0 = 0.5$, $\hbar = 0.0067$

5.4 Quantum Ratchet Current

In this section, we analyze the probability current densities associated with the Floquet states. We take $\hbar = 0.0067$ and for this choice quantum dynamics follows classical dynamics closely. We study the effect of breaking symmetries for the ratchet effect in the system. In case of classical system, if $b \to 0$, chaotic layer trapped between the KAM-curves is the only transporting layer for initial states starting from the well region. The current carried by this layer, when both spatial and temporal symmetries are broken, has a saturated value independent of initial states. However, we show that for $b >> 0$, current does not settle to constant value due to continual spread of initial states in phase space. However, we saw in previous sections that nearly all the Floquet states of interest are confined within small energy range even for $b >> 0$. Even the spread of chaotic states, as seen in Figs. 5.5(a,b) and 5.6(a-d), lie approximately within $[-p_c, p_c]$, with corresponding energy range being from ground energy threshold energy, even for $b >> 0$ and the current values should saturate after long evolution. Since the Floquet states represent asymptotic behavior in time, we directly deal with currents associated with Floquet states.

The probability current associated with i-th Floquet state $|\Psi_i\rangle$ can be calculated

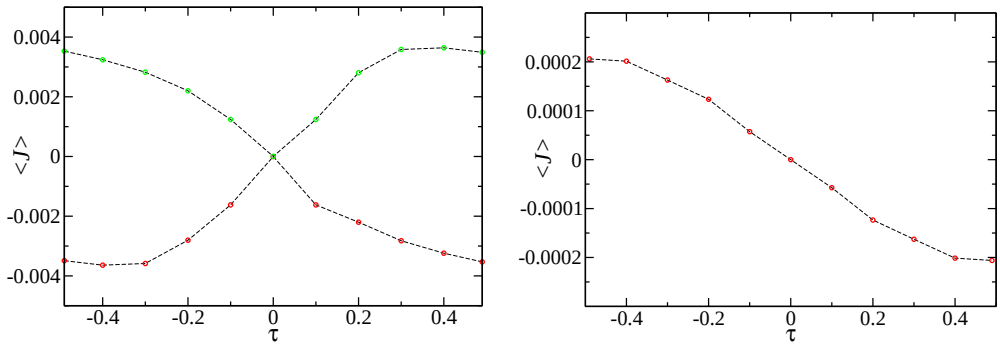

Figure 5.9: $\langle j \rangle$ separately for Floquet states carrying positive current and states carrying negative current for time symmetric system. (Right) Mean current of all chosen (see text) Floquet states at different times. Parameters: $\epsilon = 0.15, b = 0.1\pi$, $V_0 = 0.5$, $\hbar = 0.0067$

in position representation as

$$J_i = \hbar_s \Psi_i^*(x) \frac{\partial \Psi_i(x)}{\partial x}. \tag{5.37}$$

In quantum system, although states are localized in energy basis even for $b >> 0$, the saturated current is not uniquely determined by one bound chaotic layer as in the case of classical system with $b \to 0$. However, different Floquet states can, in principle, have different currents associated with them. So we take the average over the current values for different Floquet states. However, we need not to consider all the Floquet states. We consider only those Floquet states, which have at least five percent probability in region $(E \leq V_0/2)$. This energy range approximately represents the minimum width, if width is measured at different positions, of chaotic layer around hyperbolic fixed point $(-\phi, 0)$. This is done to exclude all the Floquet state which do not have significant overlap with chaotic region near hyperbolic point $(-\phi, 0)$.

Figure 5.9 shows collective behavior of all positive and negative current carrying Floquet states for different values of τ for time-symmetric case, *i.e.*, when $H(x, -t) = H(x, t)$. This symmetry holds for the case of one kick cycle. The mean current $\langle j \rangle$ for all the Floquet states carrying positive current at any $\tau = \tau_1$ is equal in magnitude to mean current for all the negative current carrying Floquet

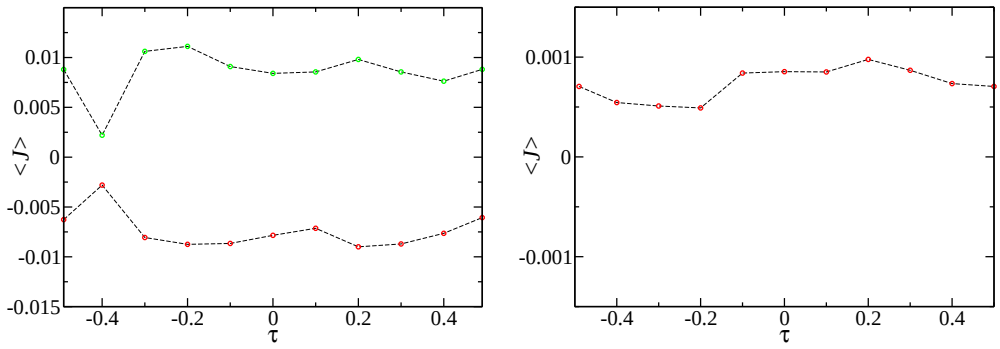

Figure 5.10: (Left) $\langle j \rangle$ separately for Floquet states carrying positive current and states carrying negative current for time asymmetric system. (Right) Mean current of all chosen (see text) Floquet states at different times. Parameters: $\epsilon_1 = 0.8, \epsilon_2 = 0.16, b = 0.1\pi$, $V_0 = 0.5$, $\hbar = 0.0067$

states at $\tau = -\tau_1$. As a result the mean positive current of all the Floquet states at $\tau = \tau_1$ is equal and opposite to mean current at $\tau = -\tau_1$. It was also observed that for $\phi = 0$, for which the system is spatially symmetric, *i.e.*, $H(-x,t) = H(x,t)$ holds, the $\langle J \rangle = 0$ at any given value of τ.

When temporal as well as spatial symmetry is broken, *i.e.*, when $H(-x,t) \neq H(x,t)$ and $H(x,-t) \neq H(x,t)$, the balance between positive and negative values of $\langle J \rangle$ breaks leading to net non-zero ratchet current, as shown in Fig. 5.10. This is achieved when $\phi \neq 0$ as well the one kick cycle is replaced by type (ii) periodic kicking cycle discussed in section (5.2). Thus, the behavior of $\langle J \rangle$ of all the Floquet states having significant overlap with chaotic region follows the current observed in the classical system with bounded chaotic layer for $b \to 0$.

Let us now define a generalized eigenstate $|\Psi_i;\tau\rangle$ of $H(x,\tau)$ such that $\langle x|\Psi_i;\tau\rangle = \Psi_i(x,\tau)$ be the solution of Schroedinger equation (5.1). Also $|\Psi_i;\tau\rangle$ will represent the i-th Floquet state of $F(\tau)$ for arbitrary τ. The probability current density associated with such an eigenstate, after integrating over τ, will be

$$I_i = \int_{\tau=-0.5}^{\tau=0.5} J_i(\tau) d\tau. \tag{5.38}$$

Figure 5.11 shows the distribution of τ integrated currents associated with different eigenstates which have minimum five percent probability in the energy range

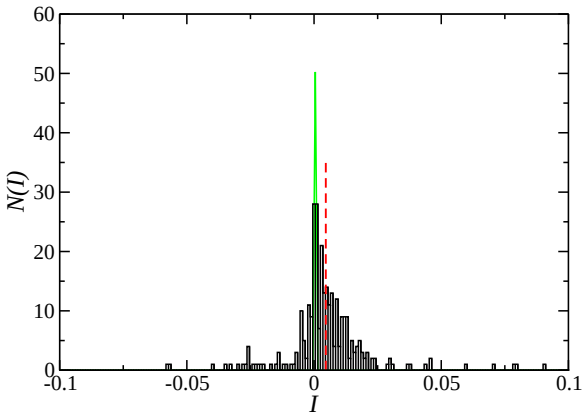

Figure 5.11: τ integrated current of eigen states for which at least five percent density lies below V_0. Parameters: $\epsilon = 0.1$, $b = 0.1\pi$, $V_0 = 0.5$, $\hbar = 0.0067$. The vertical red line mark the mean I of the distribution. The green curve shows the distribution of I values for time symmetric case. The distibution in green is not normalised. It is scaled down by factor of 20.

$E < 0.5V_0$. We see that for time symmetric case the τ integrated current, *i.e.*, I_i, has a sharp peak at $I = 0$. When temporal symmetry is broken, we get asymmetric distribution of currents with finite width. The non-zero mean current for time asymmetric system is also shown in Fig. 5.11. However, note that the spread about mean is moderate. Moreover, for any arbitrary initial state lying completely in region $(E < V_0/2)$, evolved state will be a superposition of all these Floquet states. Due to a chaotic layer in phase space near $p = 0$, in the semiclassical limit, the time evolution will mix the Floquet states sufficiently. Thus, the current in system can be expected to be robust against changes in initial states, though not fully independent of them.

We note that the net force averaged over all space and time is zero, *i.e.*, $\int_t \int_x -\frac{\partial V(x)}{\partial x} dx dt = 0$. Thus, we have shown that the system can be used to obtain net directed current in absence of net bias. In semiclassical regime, the quantum current behavior, with respect to symmetries of the system, mimics the scenario for classical system. We have also done some preliminary analysis on the system in its quantum regime, *i.e.*, for large values of $\hbar_s$. For this choice of Planck's constant, the unperturbed levels display band structure. The preliminary results we have obtained suggest that if inter-band transitions are not allowed, the net directed

transport is not possible. This is also suppoted by some theoretical prediction by Peter Hanggi [Go98]. Analysis of ratchet effect in band structure will form the future extension of this thesis.

CHAPTER 6

Summary and Future Directions

6.1 Summary

In this thesis, we have studied the dynamics and transport properties of non-KAM systems, namely, (i) the kicked particle in a potential with double barrier structure and (ii) kicked particle in a periodic lattice of finite potential wells. These time dependent systems are significant for several reasons. From the point of view of deterministic Hamiltonian chaos, they belong to a class of, sparsely explored, non-KAM systems. As an instance of kicked system in a periodic potential, it provides a connection with extensively studied condensed matter systems. Thirdly, this system exploits the KAM and non-KAM type dynamics for directed motion. The double barrier structures and quantum wells are widely used in electronic devices and the models studied in this thesis has potential experimental realization and applications.

We summarize the main results here. The classical kicked rotor system leads to well studied Chirikov map which is popularly known as standard map. We have derived maps to describe the phase space dynamics of a kicked particle in the presence of discontinuous and, hence, non-analytic potentials such as (i) and (ii) listed

above. These maps, in a sense, are generalizations of the standard map after incorporating effects of non-analytic potentials. The kicked rotor is a KAM system, where as, the system we have studied in this thesis is non-KAM due to the presence of non-analytic potentials. We have studied how the non-KAM nature of the system modifies the phase space characteristics and leads to novel dynamical features. In general, this system can show both non-KAM and KAM-like behavior in different regions of phase space.

We have reported interesting dynamical properties, namely, (a) classically induced suppression of energy growth, (b) momentum squeezing, (c) momentum pumping and (d) non-equilibrium steady state in the case of double-barrier structure. We have explained these dynamical properties on the basis of phase space features of the system. We have pointed out the role of non-KAM dynamics behind them. Classically, all these dynamical features arise due to a subtle interplay between the KAM and non-KAM type of dynamical features in the system. Typically, these features exist only for small values of kick strengths for which the usual kicked rotor has mostly regular phase space. At high values of kick strengths, since all the invariant curves are broken irrespective of whether any discontinuous potential is present or not, the non-KAM nature of the system studied in thesis does not lead to a qualitatively different dynamics. We have also studied the quantum dynamics of this system in semiclassical regime by evolving an arbitrary initial wave packet. We show that in the semiclassical regime, the classical dynamical features carry over to quantum dynamics quite well.

The dynamical features in our model such as the non-equilibrium steady state and classically induced energy growth suppression are of current interest in the general context of transport and localization especially for interacting systems such as the Bose-Einstein condensates. Recently there have been several experimental results that point to classical features suppressing energy growth of condensates [He06, Cl05]. Typically, in such experiments, condensates are released from a confining potential and their expansion in a disordered potential is studied. When

chemical potential $\mu < V_0$, where V_0 is the strength of disorder, condensates are classically reflected from the fluctuations of the disordered potential effectively localizing the condensates. In our model, particles are neither interacting nor there is any disordered potential. However, the non-KAM chaotic dynamics and KAM like invariant curves provide the essential ingredient for the suppression of diffusion. Even as the particles are transported in the position space their energy absorption is restricted by KAM like structures. Such studies form an important background to understand and clearly distinguish similar quantum phenomena like the Anderson localization from the classically induced ones and also to explore the connections between interactions, localization and disorder.

In the case of periodic lattice of finite potential wells, we analyzed the effect of periodic boundary conditions and the width of the barriers separating finite well on the dynamical features of the system. We show that for infinitesimally thin barriers, classical phase space displays a mixed layer trapped between invariant curves which act as dynamical barriers to transport. In this situation, the system approaches a steady state in which mean momentum and mean energy saturate to a constant value soon after the kicking begins to act, provided all the initial states lie in trapped region. We have shown that directed transport is possible even in absence of any net bias if both the spatial and temporal symmetries are broken. Thus, the system acts like a ratchet. We have also shown and explained that the current carried by bound mixed phase space, given by mean momentum of all the states evolving in it, is independent of initial states despite the fact that this region is not fully chaotic. We have pointed out that for $b >> 0$ all the invariant curves break down leading to mixed dynamics throughout the phase space. In this situation, the system experiences unbounded, though not normal, diffusion in momentum space even for initial states lying much below the threshold momentum. We show that this results in fluctuations in current values and dependence on initial state which increase gradually as the barrier width increases.

We have also studied the quantum dynamics of kicked particle in a periodic

lattice of finite wells. To study the quantum version of the system, we have done the Floquet analysis. We have derived the matrix form of Floquet operator in the unperturbed basis and computed its Floquet states. The Floquet states are mostly localized in energy space even for barrier width $b >> 0$, for which classical system shows mixed dynamics throughout the phase space. We have visualized the phase space features of Floquet states through Husimi distributions and showed that in semiclassical regime, signatures of classical phase space dynamics can be seen for quantum system too. We have shown that the quantum system also acts like a ratchet and displays directed transport when both the spatial and temporal symmetries are broken.

6.2 Future Directions

Several aspects of the result presented in this thesis can be studied further. A pertinent question on the phenomenology of non-KAM chaos is to verify if discontinuous potentials truly lead to abrupt transition from regularity to chaos. The numerical results seem to suggest that if the parameter R is infinitesimally away from integer value, transition is not abrupt. This will add to understanding of KAM vis-a-vis non-KAM systems. The dynamical features presented in this thesis have been argued on the basis of phase space structures. It is desirable to obtain analytical estimates for them to understand the phenomenon better. The quantum dynamics of double barrier potential has only been partially explored. For instance, we have not studied how quantum tunelling might affect the non-equilibrium steady state or the classically induced localization effects. What can be said about the competition between above the barrier escape of the particle and tunnelling rates ? In the lattice of finite potential wells, what would be the dynamics of currents in the presence of band structure ? One of the more general questions would be to explore the quantum manifestations of non-KAM system. This has not been systematically explored yet and there could be many new results in this context.

In order to be of wider interest, this model should also be experimentally realizable. Even a detailed theoretical proposal for a suitable experiments and predictions to be verified is worth attempting. This can potentially open up more areas for research. One of the likely experimental test bed would be cold atoms in optical lattices in some combination with either quantum wells or heterostructures. This might lead to considering interactions among the particles. An interesting extension of this work would be to incorporate the interparticle interaction. In light of recent experiments on kicked BEC [He06, Cl05, Fo05, Sc05a, Sa08], theoretical analysis of interacting kicked particles can be useful in explaining the features observed in these experiments. Use of delta kicks is convenient for theoretical analysis. Also, delta kicks can be realized using pulsed optical lattices in cold atom experiments. However, in most systems of practical interest like electronic circuits, waveguides etc., one deals with potential field which are continuous functions of time. So, the use of continuous driving in place of delta kicks might be useful in the context of experiments. Finally, the new frontier of quantum chaos is the study of open systems. We believe that the model studied in this thesis can be useful in the context of quantum open systems.

APPENDIX A

Effect of Barrier-width on Refraction

Consider a particle that evolves on an invariant curve of the standard map $C_5(\mu_5)$, approaches right barrier at $x_w = R\pi$ with $p > p_c$ during its motion after $n^{th}-$kick, crosses it and exits on to another invariant curve of standard map $C_6(\mu_6)$. In this appendix, we show that as the width of the barrier $b \to 0$, $C_5(\mu_5) \to C_6(\mu_6)$.

After the particle crosses the interface at x_w and if Δt denotes the time it will take to cross the barrier region of width b, then $\Delta t \to 0$ if $b \to 0$. Hence, the probability that a particle will experience the next kick while crossing the barrier will also tend to zero. Hence we can assume that the particle does not experience a kick while crossing the barrier. In such a situation, the particle will face only two discontinuities between nth and $(n+1)$th kick. Thus, $k = 2$, $B_1 = x_w$ and $B_2 = x_w + b$. From our assumptions, $\begin{pmatrix} x_n^0 \\ p_n^0 \end{pmatrix}$ lie on $C_5\,(\mu_5)$, and $\begin{pmatrix} x_n^2 \\ p_n^2 \end{pmatrix}$ will lie on $C_6\,(\mu_6)$.

$$\begin{pmatrix} x_n^1 \\ p_n^1 \end{pmatrix} = \widehat{\mathcal{R}}_1 \begin{pmatrix} x_n^0 \\ p_n^0 \end{pmatrix} \Rightarrow \begin{pmatrix} x_w + \dfrac{(x_n^0 - x_w)\, p_n^1}{p_n^0} \\ \sqrt{(p_n^0)^2 - 2V_0} \end{pmatrix} \tag{B1}$$

Similarly,

$$\begin{pmatrix} x_n^2 \\ p_n^2 \end{pmatrix} = \widehat{\mathcal{R}}_2 \begin{pmatrix} x_n^1 \\ p_n^1 \end{pmatrix} \Rightarrow \begin{pmatrix} x_w + b + \dfrac{(x_n^1 - x_w - b)\, p_n^2}{p_n^1} \\ \sqrt{{p_n^1}^2 - 2V_0} \end{pmatrix}. \qquad \text{(B2)}$$

Substituting for x_1 and p_1 from Eq. B1 in Eq. B2, we get,

$$\begin{pmatrix} x_n^2 \\ p_n^2 \end{pmatrix} = \begin{pmatrix} b - \dfrac{bp_n^0}{p_n^1} + x_n^0 \\ p_n^0 \end{pmatrix} \qquad \text{(B3)}$$

Using $b \to 0$, we get, $\begin{pmatrix} x_n^2 \\ p_n^2 \end{pmatrix} \to \begin{pmatrix} x_n^0 \\ p_n^0 \end{pmatrix}$. This implies $C_5(\mu_5) \to C_6(\mu_6)$ or $\mu_6 - \mu_5 \to 0$. Hence, refraction (see text) becomes identity operation as $b \to 0$.

APPENDIX B

KAM-like Behavior: Effect of (R, ϕ)

We show that for certain special choices of (R, ϕ), reflection from the walls of potential V_{sq} takes a state from invariant curve C_+ to its symmetric counterpart C_-, where C_+ and C_- are related through reflection symmetry about $(0, 0)$. Let

$$\left\{ \begin{array}{c} R\pi + \phi = l\pi \\ -R\pi + \phi = m\pi \end{array} \right\}, \quad l, m \in \text{integer} \tag{A1}$$

Then, $x_r = l\pi$ and $-x_l = m\pi$. Let $\begin{pmatrix} x_n^{i-1} \\ p_n^{i-1} \end{pmatrix}$ lie on C_+. Reflection from the right boundary at x_r will take it to

$$\begin{pmatrix} x_n^i \\ p_n^i \end{pmatrix} = \widehat{\mathcal{R}}_i \begin{pmatrix} x_n^{i-1} \\ p_n^{i-1} \end{pmatrix} = \begin{pmatrix} 2l\pi - x_n^{i-1} \\ -p_n^{i-1} \end{pmatrix} \tag{A2}$$

on the invariant curve C. The spatial periodicity of 2π in the standard map implies that

$$\begin{pmatrix} (2l\pi - x_n^{i-1}) \bmod (2\pi) \\ -p_n^{i-1} \end{pmatrix} = \begin{pmatrix} -x_n^{i-1} \\ -p_n^{i-1} \end{pmatrix} \tag{A3}$$

is on C. Since $\begin{pmatrix} -x_n^{i-1} \\ -p_n^{i-1} \end{pmatrix}$ is on C_- and C_- is unique, we have $C = C_-$. Thus, the effect of reflection from the right boundary at x_r is to take a state from C_+ to C_- if Eq. A1 is satisfied. Similarly, the effect of reflection from left boundary at $-x_l$ is to take a state from C_- to C_+. Hence, a state undergoing repeated reflections will remain confined to a pair of invariant curves, thus, exhibiting regular motion even in presence of non-KAM potential. We call this KAM-like behavior.

Bibliography

[An58] P. W. Anderson, Phys. Rev. **109**, 1492 (1958).

[Ar68] V. I. Arnold and A. Avez, *Ergodic Problems of Classical Mechanics*, (Benjamin, New York, 1968).

[As76] N. W. Ashcroft and D. Mermin, *Solid State Physics*, (Harcourt College Publishers, 1976).

[As94] R. Dean Astumian and M. Bier, Phys. Rev. Lett. **72**, 1766 (1994).

[Ba08] A. G. Balanov, D. Fowler, A. Patane, L. Eaves, and T. M. Fromhold, Phys. Rev. E **77**, 026209 (2008).

[Ba00] M. Barbi and M. Salerno, Phys. Rev. E **62**, 1988 (2000).

[Ba94] R. Bartussek, P. Hanggi, and J. G. Kissner, Europhys. Lett. **28**, 459 (1994).

[Be91] G. P. Berman, V. Yu. Rubaev and G. M. Zaslavsky, Nonlinearity **4**, 543 (1991).

[Bl98] Ya. M. Blanter and M. Buttiker, Phys. Rev. Lett. **81**, 4040 (1998).

[Br98] P. W. Brouwer, Phys. Rev. B **58**, R10135 (1998).

[Br06] W. R. Browne and B. L. Feringa, Nature Nanotechnology **1**, 25 (2006).

[Bu92] R. H. Bube, *Electrons in Solids: An Introductory Survey*, (Academic Press, San Diego, 1992).

[Ca05] G. G. Carlo, G. Benenti, G. Casati, and D. L. Shepelyansky, Phys. Rev. Lett. 94, 164101 (2005).

[Ca79] G. Casati, B. V. Chirikov, F. M. Izraelev, and J. Ford, Lecture Notes in Physics **93**, 334 (1979).

[Ca84] G. Casati, B. V. Chirikov, and D. L. Shepelyansky, Phys. Rev. Lett. **53**, 2525 (1984).

[Ce96] G. A. Cecchi and M. O. Magnasco, Phys. Rev. Lett. **76**, 1968 (1996).

[Ch79] B. V. Chirikov, Phys. Rep. **52**, 263 (1979).

[Ch87] A. A. Chernikov, R. Z. Sagdeev, D. A. Usikov, M. Yu. Zakharov, and G. M. Zaslavsky, Nature **326**, 559 (1987);

[Ch88] A. A. Chernikov, R. Z. Sagdeev, and G. M. Zaslavsky, Physica D **33**, 65 (1988).

[Ch89] B. V. Chirikov in *Chaos and Quantum Physics*, M. J.Giannoni, A. Voros, and J. Zinn-Justin (eds.), Les Houches, North-Holland, 1989.

[Cl05] D. Clement *et. al.*, Phys. Rev. Lett. **95**, 170409 (2005).

[Cu09] J. A. Currivan, A. Ullah, M. D. Hoogerland, Europhys. Lett. **85**, 30005 (2009).

[Da99] A. P. Davis, Nature **401**, 120 (1999).

[Da08] I. Dana, V. Ramareddy, I. Talukdar, and G. S. Summy, Phys. Rev. Lett. **100**, 024103 (2008).

[Da11] I. Dana and V. B. Roitberg, Phys. Rev. E **83**, 066213 (2011).

[De07] S. Denisov, L. Morales-Molina, S. Flach, and P. Hanggi, Phys. Rev. A **75**, 063424 (2007).

[Di03] T. Dittrich, M. Gutierrezb, and German Sinuco, Physica A **327**, 145 (2003).

[Do94] C. R. Doering, W. Horsthemke, and J. Riordan, Phys. Rev. Lett. **72**, 2984 (1994).

[Du05] S. Dutta, *Quantum Transport : Atom to Transistor*, (Cambridge Univeristy Press, Cambridge, 2005).

[Er09] L. Ermann, G. G. Carlo, and M. Saraceno, Phys. Rev. E **79**, 056201 (2009).

[Fe63] R. P. Feynman, R. B. Leighton, and M. Sands, *The Feynman Lectures on Physics*, Vol.1, (Addison-Wesley, 1963).

[Fe08] D. Ferry and S. M. Goodnick, *Transport in Nanostructures*, (Cambridge Univeristy Press, Cambridge, 2008).

[Fi82] S. Fishman, D. R. Grempel, and R. E. Prange, Phys. Rev. Lett. **49**, 509 (1982).

[Fl00] S. Flach, O. Yevtushenko, and Y. Zolotaryuk, Phys. Rev. Lett. **84**, 2358 (2000).

[Fo05] C. Fort *et. al.*, Phys. Rev. Lett. **95**, 170410 (2005).

[Fr01] T. M. Fromhold, A. A. Krokhin, C. R. Tench, S. Bujkiewicz, P. B. Wilkinson, F. W. Sheard, and L. Eaves, Phys. Rev. Lett. **87**, 046803 (2001).

[Fr05] M. Frigo and S. G. Johnson, *Fastest Fourier Transform in the West*, Proc. of the IEEE **93**, 216 (2005); `http://www.fftw.org`.

[Ga97] S. A. Gardiner, J. I. Cirac and P. Zoller, Phys. Rev. Lett. **79**, 4790 (1997).

[Go98] Igor Goychuk, Milena Grifoni, and Peter Hanggi, Phys. Rev. Lett. **81**, (1998).

[Gr84] D. R. Grempel, R. E. Prange, and S. Fishman, Phys. Rev. A **29**, 1639 (1984).

[Gr02] M. Grifoni, M. S. Ferreira, J. Peguiron, and J. B. Majer, Phys. Rev. Lett. **89**, 146801 (2002).

[Ha05] P. Harrison, *Quantum Wells, Wires and Dots*, (Wiley-Interscience, Chichester, 2005).

[Ha09] P. Hanggi and F. Marchesoni, Rev. Mod. Phys. **81**, 387 (2009).

[He06] K. Henderson *et. al.*, Europhys. Lett. **75**, 392 (2006).

[Hu94] B. Hu, B. Li, J. Liu, and Y. Gu, Phys. Rev. Lett. **82**, 4224 (1994).

[Hu40] K. Husimi, Proc. Phys. Math. Soc. Jpn. **22**, 264 (1940).

[Hu04] N. A. C. Hutchings, M. R. Isherwood, T. Jonckheere, and T. S. Monteiro, Phys. Rev. E **70**, 036205 (2004).

[Hu05] G. Hur, C. E. Creffield, P. H. Jones, and T. S. Monteiro, Phys. Rev. A **72**, 013403 (2005).

[Is04] Matthew Isherwood, Ph. D. thesis, `http://www.ucl.ac.uk/~ucap2tm/CHAOS/ratchet.html`, UCL, 2004.

[Iz90] F. M. Izrailev, Phys. Rep. **196**, 299 (1990).

[Jo07a] P. H. Jones *et. al.*, Phys. Rev. Lett. **98**, 073002 (2007).

[Ju96] P. Jung, J. G. Kissner, and P. Hanggi, Phys. Rev. Lett. **76**, 3436 (1996).

[Ka98] H. Kamegawa, T. Hondou, and F. Takagi, Phys. Rev. Lett. **80**, 5251 (1998).

[Ke08] A. Kenfack, J. Gong, and A. Pattanayak, Phys. Rev. Lett. **100**, 044104 (2008).

[Ki03] C. Kittel, *Introduction to Solid State Physics*, (John Wiley & Sons, 2003)

[Ko03] A. Komnik and A. O. Gogolin, Phys. Rev. B **68**, 235323 (2003).

[Ku98] J. Kula, T. Czernik, and J. Luczka, Phys. Rev. Lett. **80**, 1377 (1998).

[Le03] A. F. J. Levi, *Applied Quantum Mechanics*, (Cambridge University Press, 2003),

[Li80] R. L. Liboff, *Introductory Quantum Mechanics*, (Assison-Wesley, 1980).

[Lib] `http://www.netlib.org/`

[Lo00] R. Loudon, *The Quantum Theory of Light*, (Oxford University Press, 2000).

[Ma93] M. O. Magnasco, Phys. Rev. Lett. **71**, 1477 (1993).

[Ma94] M. O. Magnasco, Phys. Rev. Lett. **72**, 2656 (1994).

[Ma00] J. L. Mateos, Phys. Rev. Lett. **84**, 258 (2000).

[Mo94] F. L. Moore, J. C. Robinson, C. Bharucha, P. E. Williams, and M. G. Raizen, Phys. Rev. Lett. **73**, 2974 (1994).

[Mo95] F. L. Moore, J. C. Robinson, C. F. Bharucha, B. Sundaram, and M. G. Raizen, Phys. Rev. Lett. **75**, 4598 (1995).

[Mo00] T. S. Monteiro, P. A. Dando, N. Hutchings, and N. Isherwood, Phys. Rev. Lett. **84**, 2358 (2000).

[Mo02] T. S. Monteiro, P. A. Dando, N. A. C. Hutchings, and M. R. Isherwood, Phys. Rev. Lett. **89**, 194102 (2002).

[Ot93] E. Ott, *Chaos in Dynamical Systems* (Cambridge University Press, 1993).

[Po07] D. Poletti, G. G. Carlo, and B. Li, Phys. Rev. E **75**, 011102 (2007).

[Re80] A. B. Rechester and R. B. White, Phys. Rev. Lett. **44**, 1586 (1980).

[Re97] P. Reimann, M. Grifoni, and P. Hanggi, Phys. Rev. Lett. **79**, 10 (1997).

[Re02] P. Reimann, Phys. Rep. **361**, 57 (2002).

[Re04] L. E. Reichl, *The transition to chaos: Conservative classical systems and quantum manifestations*, (Springer, New York, 2004).

[Sa99] A. Sarmiento and H. Larralde, Phys. Rev. E **59**, 4878 (1999).

[Sa01] R. Sankaranarayanan, A. Lakshminarayan, and V. B. Sheorey, Phys. Rev. E **64**, 046210 (2001).

[Sa01a] R. Sankaranarayanan, A. Lakshminarayan and V.B. Sheorey, Phys. Lett. A 279, 313 (2001)

[Sa08] L. Sanchez-Palencia *et. al.*, New J. Phys. **10**, 045019 (2008).

[Sa09] T. Salger, S. Kling, T. Hecking, C. Geckeler, L. Morales-Molina, and M. Weitz1, Science **326**, 1241 (2009).

[Sc97] L. Schimansky-Geier, M. Kschischo, and T. Fricke, Phys. Rev. Lett. **79**, 3335 (1997).

[Sc01] H. Schanz, Marc-Felix Otto, R. Ketzmerick, and T. Dittrich, Phys. Rev. Lett. **87**, 070601 (2001).

[Sc05] H. Schanz, T. Dittrich, and R. Ketzmerick, Phys. Rev. E **71**, 026228 (2005).

[Sc05a] T. Schulte *et. al.*, Phys. Rev. Lett. **95**, 170411 (2005).

[Sc07] T. Schwartz, G. Bartal, and S. Fishman, Nature **446**, 52 (2007).

[St93] H. J. Stockmann, *Quantum Chaos: An Introduction* (Cambridge University Press, 1993)

[Ta89] M. Tabor, *Chaos and Integerability in Nonlinear Dynamics-An Introduction* (Wiley-Interscience, 1989).

[Ta89a] K. Takahashi, Prog. Theor. Phys. (Suppl.) **98**, 109 (1989).

[Ta07] D. J. Tannor, *Introduction to quantum mechanics: A time dependent perspective*, (University Science Books, 2007).

[Tr00] E. Trias, J. J. Mazo, F. Falo, and T. P. Orlando, Phys. Rev. E **61**, 2257 (2000).

[Wa08] J. Wang and J. Gong, Phys. Rev. E **78**, 036219 (2008).

[Wa08a] J. Wang and J. Gong, Phys. Rev. E **77**, 031405 (2008).

[Za05] G. M. Zaslavsky, *Hamiltonian Chaos and Fractional Dynamics*, (Oxford University Press, Oxford, 2005).

[Za07] G. M. Zaslavsky, *Physics of Chaos in Hamiltonian Systems*, 2nd edn, (Imperial College Press, 2007).

[Zn10] M. Znidaric, J. Stat. Mech.: Theory Exp. 2010 L05002.

List of Publications

1. *Dynamics of δ-kicked particle in a finite potential well*
   Harinder Pal and M. S. Santhanam
   Nonlinear Dynamics, edited by M. Daniel and S. Rajasekar (Narosa Publishing House, New Delhi, India, 2009).

2. *Dynamics of kicked particles in a double-barrier structure*
   Harinder Pal and M. S. Santhanam
   Phys. Rev. E 82, 056212 (2010).

3. *Classically induced suppression of energy growth in a chaotic quantum system*
   Harinder Pal and M. S. Santhanam
   Accepted for publication in Pramana - Journal of Physics.